Novel Low-Cost Scalable Nanofabrication Technologies by Soft Lithography, Plasmonic Lithography, and Electrochemical Processes

by

Kaito Yamada

A dissertation submitted in partial fulfillment
of the requirements for the degree of
Doctor of Philosophy
(Applied Physics)
in The University of Michigan
2021

Doctoral Committee:

Professor L. Jay Guo, Chair
Professor Cagliyan Kurdak
Professor Stephen Maldonado
Professor Zetian Mi

Kaito Yamada

kaitoy@umich.edu

ORCID iD: 0000-0003-4413-6340

ACKNOWLEDGEMENTS

First of all, I would like to express my deepest gratitude to Professor L. Jay Guo for guiding me in my Ph.D. study. He has always brought fruitful discussions, new ideas, and has been supportive of students' ideas. Without his strong support and sound advice, I would not have been able to accomplish my degree. I would also like to express my appreciation to my dissertation committee members, Professor Cagliyan Kurdak, Professor Stephen Maldonado, and Professor Zetian Mi for serving on my committee and giving me insightful guidance. I would also like to thank Professor Kurdak for helping me as the director of Applied Physics Program. I am grateful that I could study in such a wonderful environment and experience the diverse curriculum of the Applied Physics Program. I would also like to thank the LNF engineers and staff for providing and supporting a wonderful environment for experimental research at the cleanroom. Dr. Pilar has always helped me with my experiments and offered immense encouragement.

I also greatly appreciate Guo group members' help and kindness throughout my study. I would like to thank Zhong Zhang, my first mentor, for teaching me nanoimprint lithography and basic skills on experiments. I would also like to express my appreciation to Dr. Xi Chen for giving me advice on the plasmonic lithography project even after she graduated. I would like to thank Dr. Sungho Lee for helping me with many works, from nanoimprint lithography to photo roller lithography. Without his ideas and help, my work could not have been successful. I would like to thank Dr. Chengang Ji and Dr. Saurabh Acharya for guiding me

in research as both collaborators and friends. I have been always motivated by their enthusiasm for research. I would also like to thank Jennie Paik for her help for in enhancing group interaction and being a good friend to me. I want to like to thank all of my former and current group members for their assistance and friendship. I am grateful that I also had many opportunities to collaborate with researchers outside of University of Michigan. I would like to thank all of my collaborators, the Oklahoma State University group, the University of Illinois Urbana Champaign group, NanosurfaceBio, and VisionEase. I would also like to acknowledge and show gratitude for the financial support from KDDI Foundation, National Science Foundation, and Rackham Graduate School of University of Michigan.

From the bottom of my heart, I want to thank the friends I have met here Michigan. My cohorts in Applied Physics are wonderful people, and I am very pleased that I could learn so much from them. Finally, I would like to thank my parents for a lifetime of support and encouragement. Without their love and support, I could never have pursued my degree or my dreams.

TABLE OF CONTENTS

LIST OF TABLES

LIST OF FIGURES

ABSTRACT

As wide variety of devices such as optical devices, wearable devices, and color filters have become more common, the demand for technologies which can fabricate these devices at a low cost is at an all-time high. Photolithography is currently the most widely used patterning technology in industries, but its resolution is physically limited by the diffraction of light. Although there have been many technologies developed to improve the resolution limit of photolithography, the increasing cost remains one of the biggest concerns. As another key technology, material depositions are also an important factor in determining the fabrication cost for nanotechnology devices. The most common technologies are vacuum depositions, such as physical vapor deposition and chemical vapor deposition, due to their high controllability and plainness. However, the high vacuum required for this process increases the cost significantly, since it limits the size of substrates, takes a long time to pump, and requires many expensive tools.

There have been many studies on alternative technologies for the main processes used in nanotechnology fabrications, e.g., nanoimprint lithography, plasmonic lithography, and electrochemical depositions. Despite the fact that they have some advantages in cost, practical applications are still very limited because of their complexities. In this dissertation, nanoimprint lithography technologies aimed at practical applications will be discussed first. Moreover, a newly developed technique based on metal transfer assisted nanolithography

will be introduced to expand its ability to fabricate various devices on a wider choice of materials.

As the second topic, plasmonic lithography, a super resolution optical lithography utilizing surface plasmon polaritons excited by evanescent waves will be discussed. While there have been many studies on plasmonic lithography to achieve sub-diffraction limit patterns, attempts to scale up this technology for larger sizes and higher productivity have not been well investigated, which has created a barrier in putting this technology to practical use in mass production. In this thesis, large area plasmonic photo roller lithography by epsilon-near-zero hyperbolic metamaterials will be introduced as a potential solution for higher productivity. Although the experiment requires a somewhat complex fabrication process and setup, plasmonic lithography by the 5^{th} order diffraction has been successfully performed.

Lastly, electroplating and electroless plating will be discussed as low-cost material deposition technologies. Even though these technologies have a long history and have been used in industries for various purposes, the potential application to nanotechnology fields has been very limited. This dissertation focuses on the optics and photonics applications of electrochemistry, in particular, broadband light absorbers and structural colors. Electroless plating of Pt was performed on a porous substrate to fabricate a device showing excellent light absorptance in a wide range of wavelengths and electroplating of metals and metal oxides was employed to fabricate Fabry-Pérot cavities to create color filters. Both experimental and computational work are reported to characterize their performances.

CHAPTER 1

Introduction to Various Nanofabrication Technologies

1.1 Photolithography and the diffraction limit of light

Lithography technologies have been a focus of interest in the semiconductor industry since the earliest stages. According to Moore's Law, the minimum patternable size has determined the number of transistors fabricated in single chip and contributed to the improvements in the performance, energy efficiency, and fabrication cost. Photolithography has been the most widely used technology for patterning in industry because of its high throughput and resolution. When the line width of the transistors in microprocessors were μm scale, the resolution limit of photolithography had room to improve since the bottle neck of this technology was not caused by the theoretical limit of physics. In other words, the light source used in those days, Hg lamps, had three spectral lines 436 nm (g-line), 405 nm (h-line), and 365 nm (i-line), and the diffraction limit of those wavelengths are much smaller than the process nodes. However, as the miniaturization of the transistors fabricated in a single chip has advanced, the line width of the transistor has become closer to the diffraction limit of the light source. Thereafter, new light sources with shorter wavelengths, KrF (248 nm) and ArF (193 nm), have been introduced to achieve further resolution, but the process nodes of the transistors had soon caught up to the resolution limit.

The diffraction limit of light in photolithography can be derived by the following method. Considering an infinitesimal dipole with frequency ω in front of a lens, 2D Fourier

expansion gives the electric field

$$\boldsymbol{E}(\boldsymbol{r},t)=\sum_{\sigma,k_x,k_y}\boldsymbol{E}_{\sigma}(k_x,k_y)\times\exp\left(ik_z z+ik_x x+ik_y y-i\omega t\right) \tag{1.1.1}$$

where z axis is the axis of the lens and from Maxwell's equations, the dispersion relation of k_x, k_y, and k_z can be obtained.

$$k_x^2+k_y^2+k_z^2=k^2=\frac{\omega^2}{c^2} \tag{1.1.2}$$

Thus, for small values of k_x and k_y,

$$k_z=+\sqrt{\frac{\omega^2}{c^2}-k_x^2-k_y^2},\qquad \frac{\omega^2}{c^2}>k_x^2+k_y^2 \tag{1.1.3}$$

However, for large values of k_x and k_y,

$$k_z=+i\sqrt{k_x^2+k_y^2-\frac{\omega^2}{c^2}},\qquad \frac{\omega^2}{c^2}<k_x^2+k_y^2 \tag{1.1.4}$$

These waves are evanescent waves decaying exponentially along the z direction. Therefore, in the regular photolithography systems, these waves cannot be used for patterning and the resolution can never be higher than

$$\Delta=\frac{2\pi}{k_{\max}}\sim\frac{2\pi c}{\omega}=\lambda \tag{1.1.5}$$

where λ is the wavelength of the light source.

When it comes to the device fabrication, the more important parameter is the half pitch of the periodic pattern, which means the half feature size of the linewidth and spacewidth. In that case, the resolution becomes the ability to distinguish the two objects that are close together. In photolithography, the resolution limit is usually expressed as

$$\Delta \sim k_1 \frac{\lambda}{NA} \tag{1.1.6}$$

which is well-known as the Rayleigh criteria. Here, k_1 is a coefficient that depends on many factors related to the process and *NA* is the numerical aperture of the projection system. *NA* is also interpreted as $n\sin\theta$ where n is the refractive index of the medium between the lens and substrate, and θ is the maximal half-angle of the cone of light that can enter or exit the lens.

There have been many technologies introduced in the industry to overcome challenges, such as the double patterning [1,2] and immersion lithography [3,4], and then extreme ultraviolet lithography, which employs a 13.5 nm wavelength light source, has been put in practice recently [5,6]. However, the increasing fabrication cost due to the complexity of the process, equipment cost, and low yield, is a significant issue as shown in Figure 1-1 [7]. Moreover, since the applications of nanofabrication technology have broadened as various devices such as the virtual/augmented reality [8,9], wearable electronics [10,11], and flexible devices [12,13] become more common, technology that can fabricate these devices at a low cost has become more important and in high-demand.

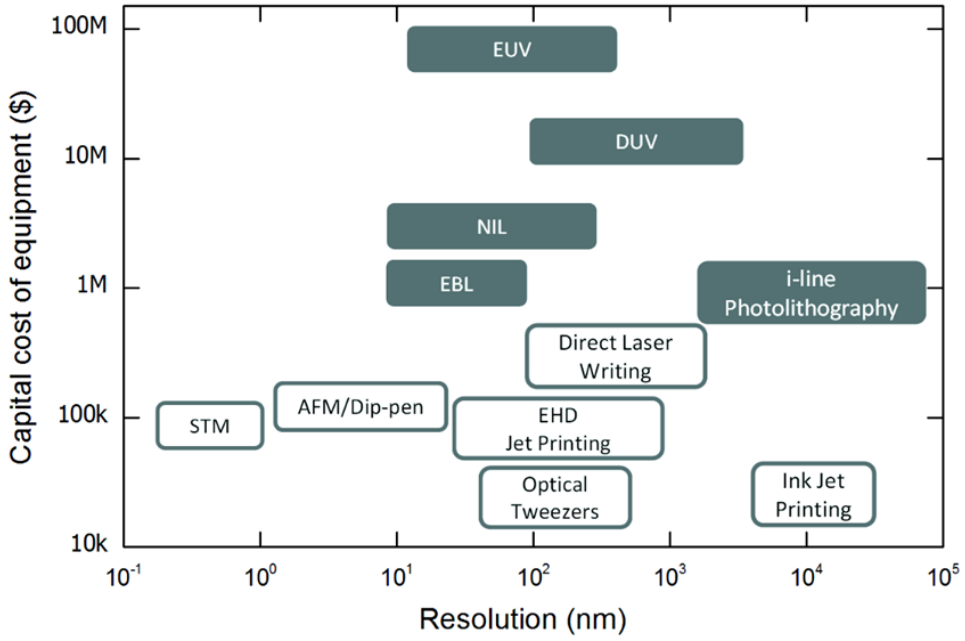

Figure 1-1 The resolutions and capital costs of equipment for various patterning technologies, adapted from literature [7]. Copyright (2014) Springer.

1.2 Next generation lithography technologies

To replace photolithography, there have been many studies on alternative patterning technologies. For example, electron beam lithography has been used for long time, as it can fabricate sub-10 nm patterns due to the extremely short wavelength of the accelerated electrons [14]. A focused beam of electrons can draw custom patterns on an electron beam resist, but the throughput is extremely low because it essentially draws the patterns one by one. Thus, electron beam lithography cannot replace photolithography for the purposes of fabrication, and low-volume production.

Nanoimprint lithography is a more promising technology in terms of both the resolution and throughput [15–18]. When nanoimprint lithography was first performed in

1995, it brought a huge impact to the field with its very high resolution, showing 25 nm holes and 30 nm lines patterning [15]. Since then, the nanoimprint lithography has been intensively studied as one of the next generation lithography technologies. A master mold, a nano patterned substrate used in nanoimprint lithography, plays an important role since it is the main factor defining the minimum feature size. The master mold is pushed onto polymers with heat and/or UV light to emboss the patterns. As a result, the reverse patterns of the master mold are transferred onto the substrate as Figure 1-2(b) shows, and there is theoretically no resolution limit. Sub-10 nm resolution, which is much higher than the immersion photolithography (using the state-of-the-art photolithography technology with ArF excimer laser) was reported even in the early stage of the nanoimprint lithography [19,20]. While some other next-generation lithography technologies such as electron beam lithography can have similar or even higher resolution than the nanoimprint lithography, the biggest advantage of the nanoimprint lithography is its cost efficiency, as master molds can be repeatedly used several times. Therefore, even if the mold fabrication process is expensive, the overall fabrication cost for large lots will be inexpensive enough for the mass production. Furthermore, since its ability to create patterns directly on polymer films is more suitable for flexible optical device applications (e.g. wire grid polarizers) than photolithography, nanoimprint lithography has already been used for a wide variety of applications in the industry.

The first experiment using this nanoimprint lithography was thermal nanoimprint lithography done on the PMMA layer [15–17]. Polymer materials usually have the glass

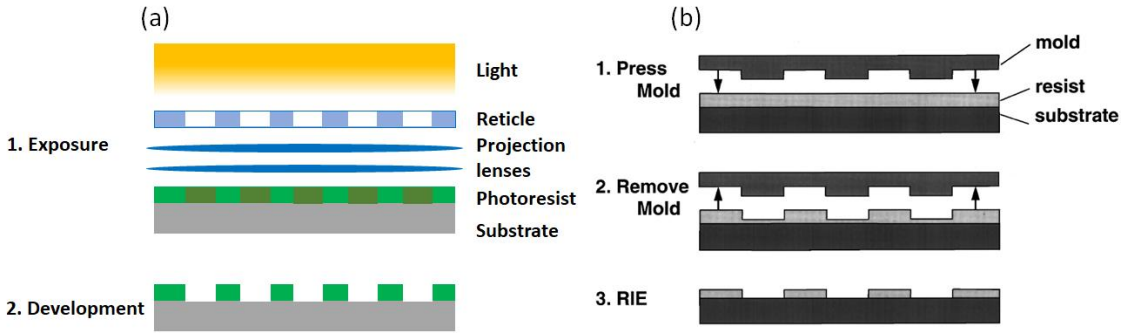

Figure 1-2 Schematics of (a) photolithography and (b) nanoimprint lithography, adapted from literature [17]. Copyright (1996) AIP Publishing.

transition temperatures where they become soft enough to be imprinted by a patterned mold, and once they are cooled, the patterned polymers become hard enough again to keep the patterns. While thermal nanoimprint lithography has the advantage of being compatible with most polymers, there are several disadvantages, including a long processing time, thermal shrinkage, and the heat tolerance of the master mold which must be considered.

Soon after the first thermal nanoimprint was reported, UV nanoimprint lithography was also performed by J. Haisma *et al* [21]. While UV nanoimprint lithography limits the usable materials to UV curable polymers, it has advantages in the pattern fidelity, productivity, and the choice of master molds. Although there is still shrinkage as a result of the UV curing of polymers, it is typically smaller than the thermal shrinkage, and the UV curing time to fully crosslink the resin is also shorter than the heating/cooling process in thermal nanoimprint lithography. Furthermore, the master mold can be less heat tolerant since the process does not require a high temperature. Therefore, depending on the

applications and requirements, the more appropriate technology should be chosen from either thermal nanoimprint lithography or UV nanoimprint lithography.

In parallel with achieving very high resolutions, many studies have also been focused on improving the productivity and patterning area size. In the early stage, a step-and-repeat process was employed for nanoimprint lithography as it was used for photolithography too [22]. Then later, the first experiment on roll-to-roll nanoimprint lithography, which is capable of continuous patterning using a flexible nanoimprint mold wrapped on a roller system, was reported [23–25]. It brought a significant impact to the field of nanoimprint lithography because it enabled patterning in a large area with higher productivity [26,27]. This technology has opened up a whole new world of applications, e.g., moth-eye films [28], wire grid polarizers [24], and so on, owed to its excellent cost efficiency in producing such structures directly on polymer films. These technologies play a key role in the display industry, virtual reality industry, and augmented reality industry which has been growing rapidly recent years. In this thesis we report on both conventional nanoimprint lithography for specific applications, as well as a new soft lithography technique based on nanoimprint lithography which extends the potential applications of soft lithography.

Soft lithography technologies, which sometimes include nanoimprint lithography, are not limited to embossing patterns on a substrate but also can transfer patterns and replicate structures [29–32]. For example, when polydimethylsiloxane (PDMS) is poured into a nanoimprint mold and cured, a PDMS stamp with the reverse patterns of the master mold can be easily obtained. The master mold can be used repeatedly in this technique, further

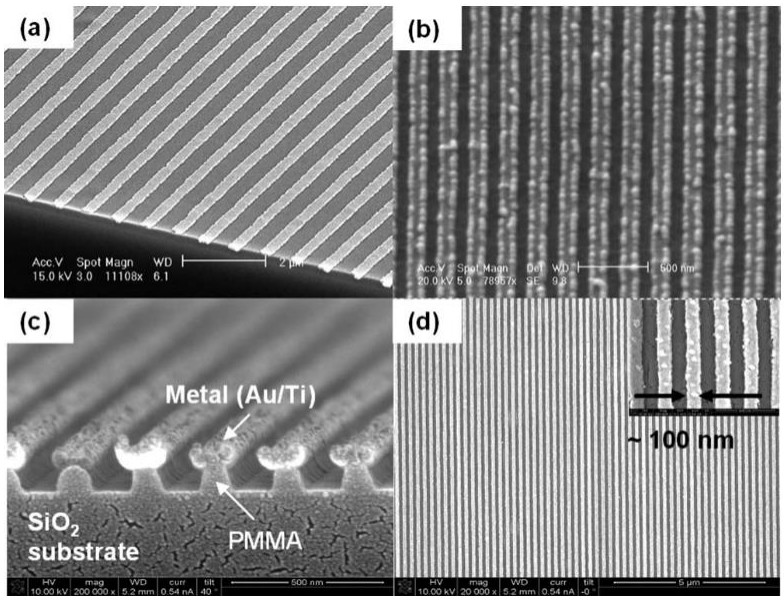

Figure 1-3 SEM images of the transferred metal gratings, etched PMMA layer, and deposited another metal through the pattern. (a) A tilted view and (b) top view of the transferred gratings. (c) A cross-sectional image of the etched PMMA layer. (d) The deposited metal gratings through the PMMA pattern. Adapted from literature [31]. Copyright (2008) AIP Publishing.

contributing to the cost efficiency. As a pattern transfer technology, Figure 1-3 shows metal transfer assisted nanolithography reported in 2008 [31]. Thin metal films were deposited on a PDMS stamp fabricated by the process above, and it was used for selective pattern transfer only where the structures were in contact with the Polymethyl Methacrylate (PMMA) coated substrate. This technique enables not only pattern transferring but also the shadow pattern fabrication using metal transfer films as the etching mask in the subsequent process. Therefore, soft lithography technologies have a wide variety of applications for both solid and flexible devices. However, the compatible materials in metal transfer assisted nanolithography is very limited because of the process conditions: a high temperature (115 ˚C) and insufficient surface energy of PMMA.

Though based on optical lithography technology, overcoming the diffraction limit of light by utilizing near-field light has also been well studied recent years [33–36]. In a regular system, the near-field light decays very fast and cannot transfer the information [37]. However, under certain conditions, e.g. periodic metal structures or metamaterials, it can be coupled with surface plasmon polaritons [38] and can propagate in the photomask to expose photoresist. This technology is called plasmonic lithography because it utilizes plasmon. The biggest advantage of this technology is that a similar optical system used in photolithography can be employed, while the resolution can go beyond the diffraction limit of light. However, as described above, since the near-field light cannot propagate deeply in a regular medium, the experimental results reported in the early stage showed only shallow photoresist patterns, i.e., low aspect ratios as seen in Figure 1-4 [33]. In recent studies, the ability to pattern high aspect ratio structures have been reported by using a thin Al layer as a spatial frequency filter and creating a Fabry-Pérot cavity in the photoresist layer [39,40]. This is done by sandwiching it with another substrate coated with Al/Al_2O_3. Although the wavelength of the light source is 405 nm, the resolved patterns in the photoresist layer have a period of 122.5 nm, and they are high enough for subsequent processes such as dry etching or material deposition.

Thereafter, advanced work on plasmonic lithography using epsilon-near-zero hyperbolic metamaterials (ENZ HMMs) to achieve the further reduced periodicity from the photomask level to the photoresist level has been reported [40–42]. The ENZ HMM used here works in a similar way as the previous one, but only passes the 3rd order of diffractions, which gives the 1/6 period from the photomask grating period. Therefore, even though the

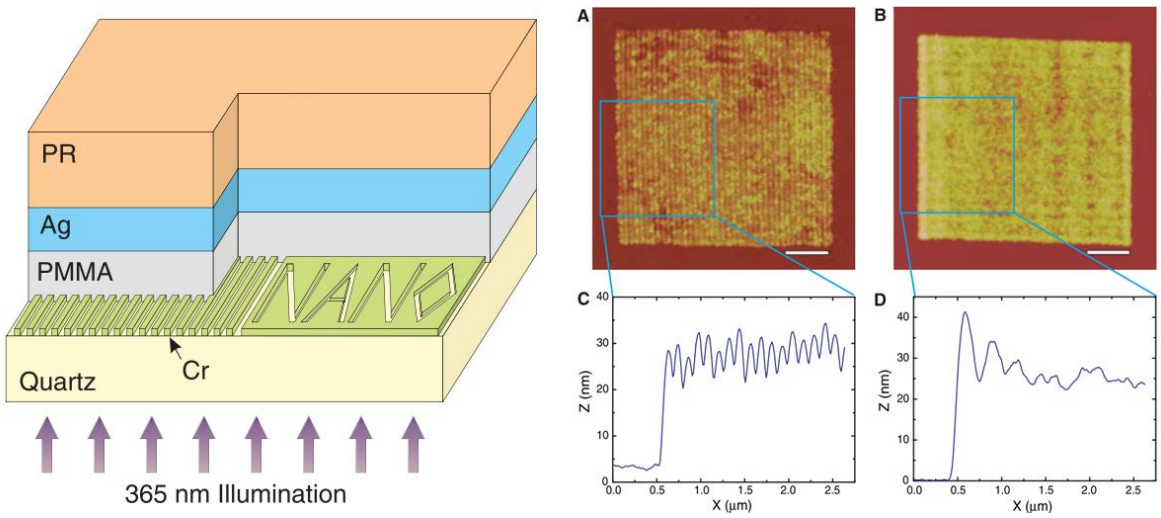

Figure 1-4 A schematic of plasmonic lithography and AFM measurements on the resolved grating patterns. It is shallow but the sub-diffraction limit patterns were resolved, adapted from literature [33]. Copyright (2005) Science.

Al gratings on the photomask have the period of 700 nm, the resulting photoresist patterns have 117 nm in period. This is also promising as a low-cost mass production technology,especially for optical applications such as wire grid polarizers since it is suitable for periodic pattern fabrications. However, the scaling up of this technology to a large area is challenging because of the complexity of the photomask. This is the main reason that most experimental work of plasmonic lithography has performed well only in a small area.

Another attempt to increase the throughput of plasmonic lithography as well as thepatternable size has been performed in our previous work by combining the plasmonic lithography technology with a photo roller system [43], which enables continuous patterning when a flexible photomask is employed. Although this work has shown potential for this technology to be used for large areas and continuous lithography, the photomask size is still

not large enough since electron beam lithography was used for the grating fabrication of the photomask. Moreover, the requirements of flexibility and transparency for the substrate makes photomask fabrication very challenging, and only simple plasmonic lithography utilizing the 1st order diffraction has been performed. The expected next step is for plasmonic photo roller lithography to utilize an ENZ HMM photomask to realize a large area of continuous patterning while maintaining the resolution sub-diffraction limit.

Many alternative patterning technologies are still developing but appear promising for low-cost fabrications. Since the required patterns and characteristics for current nanotechnology devices vary depending on the application, it is expected that a suitable process is chosen for each device fabrication. Further development of these technologies remains in high demand.

1.3 Material deposition technologies

Material deposition technologies are also significant for the device fabrications in nanotechnology to give function to devices, and it is one of the key factors in determining the fabrication cost. The most common process in the industry is vacuum deposition because of its wide material compatibility, high accuracy in thickness control, and quality of the deposited films. However, the vacuum process requires high vacuum in a chamber, which restricts the substrate size and takes time to pump down. This usually increases the fabrication cost. Therefore, low-cost material deposition technologies have attracted a great deal of attention in recent years, especially for applications such as broadband light absorbers [44–46] and structural colors [47,48], in which fabrication cost plays an especially large role.

One of the common processes for material deposition is physical vapor deposition (PVD), which produces a vapor phase of materials to deposit on the target substrate. Electron beam or thermal evaporations are widely used in both industry and research because of its broad material compatibility covering many metal oxides and alloys as well as metals. A source material is put in a crucible made from Al_2O_3, Molybdenum, or Tungsten, and Joule heat or an electron beam is applied to evaporate the source. The evaporated material is condensed on the workpiece to form a thin film as Figure 1-5(a) shows. Because of this principle, the deposition occurs vertically, which means the structure shapes on the substrate will remain after the process. Moreover, a wide variety of substrates can be used as a workpiece including polymers, since the process temperature in the chamber is not too high.

As another common PVD process, sputtering is often used but has different characteristics. In sputtering, several hundreds of volts are applied between the two electrodes: a workpiece and target (i.e. the material to be evaporated) in an inertial atmosphere (e.g. Argon). As a result, the created glow plasma discharge bombards the target material and generates a vapor phase. Since the bombarded atoms or molecules fly to the workpiece at random angles, the material deposition occurs conformally on the surface as shown in Figure 1-5(b). Therefore, sputtering is more suitable for uniform depositions in a large area compared to electron beam or thermal evaporations. However, owing to its mechanism, the conductivity of the target is important, and it is difficult to deposit non-conductive materials such as metal oxides or highly pure semiconductors at a high deposition rate.

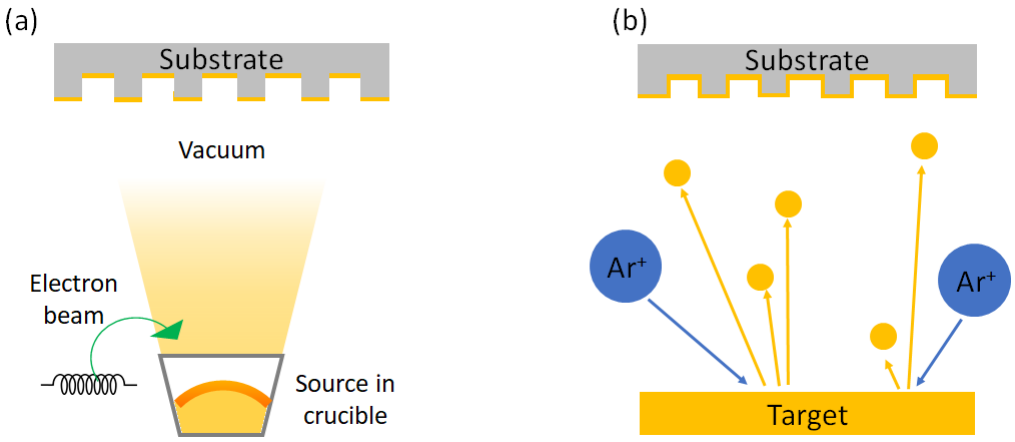

Figure 1-5 Schematics of (a) electron beam deposition and (b) sputtering.

Chemical vapor deposition (CVD) is also a major process used in the semiconductor industry to deposit various thin films. In this process, a substrate is exposed to volatileprecursors that react or decompose on the substrate surface, and as a result, a thin film of the desired material is created. CVD typically does not require as high of a vacuum as PVD, yet it has comparably high deposition rates. Moreover, by choosing a suitable substrate and chemicals, selective deposition on the substrate is also possible. However, since CVD generally requires a high temperature (e.g. 600-1100 ˚C), the substrate choice is limited. Atomic layer deposition (ALD), which is similar technology with CVD, can deposit materials with one atomic layer at a single cycle. This high level of controllability contributes to more uniform coatings and higher accuracy, but the low deposition rate and high process temperature results in greater fabrication costs and a limited material choice.

Aside from vacuum processes, wet chemical processes also have a long-standing history, and have been used for many applications. Two major electrochemical depositions,

electroplating and electroless plating, are typically employed depending on the application and substrate properties. In electroplating, the applied voltage between two electrodes drive the reduction of metal ions to pure metals. Because of this mechanism, electroplating requires conductive substrates, and the current flow in the solution dominates the characteristic of the material deposition, resulting in directional deposition much like thermal evaporation. However, by bubbling gasses in the solution (e.g., O_2) metal oxides can also be deposited [49–51]. Although metal oxides are generally non-conductive materials, and only a very thin film is electroplatable due to the thick film insulating the current flow, some metal oxides such as ZnO or SnO_2 show high conductivity and can be deposited much thicker. Therefore, by choosing suitable materials, electroplating can be employed for many optical applications like structural colors and photonic crystals while contributing to cost reduction.

On the other hand, in electroless plating, catalytic materials such as Palladium (Pd) coated on the substrate reduces metal ions to pure metals. Since electroless plating occurs where the catalytic materials are, it can produce a conformal deposition like sputtering when the substrate is uniformly coated with the catalyst as shown in Figure 1-6(b), and the conductivity of the substrate is not necessary. The most important process for electroless plating is coating substrates with catalytic materials. If a vacuum deposition is employed for it, the biggest advantage of electroless plating, i.e. a low-cost wet chemical process, cannot be well utilized. A recent study by S. Horiuchi and Y. Nakao has reported a universal process for Pd colloid deposition on a wide variety of materials using a cationic surfactant and negatively charged colloidal particles [52]. Since the Pd colloid can catalyze various metals such as Cu, Au, and Pt, this technology enables low-cost fabrication for many applications.

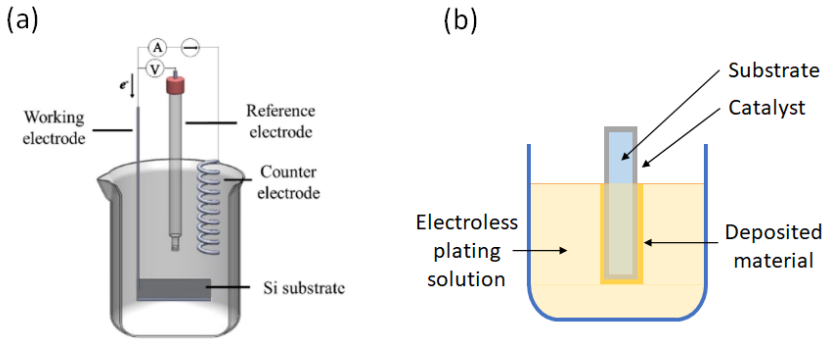

Figure 1-6 A schematic of (a) electroplating, adapted from literature [47]. Copyright (2019) ACS. (b) A schematic of electroless plating.

Because of the various characteristics of each technology, appropriate processes need to be chosen depending on the application to ensure the cost reduction of the fabrication process. Therefore, studies on not only the processes themselves, but also on the appropriate applications are highly valuable and sought-after.

1.4 Dissertation overview

This dissertation will mainly discuss the three technologies introduced above: soft lithography, plasmonic lithography, and electrochemical deposition. In addition to introducing new materials in both thermal and UV nanoimprint lithography, a newly developed technique based on metal transfer assisted nanolithography will be reported in Chapter 2. Based on our previous work with plasmonic lithography, the advanced process using a flexible photomask with ENZ HMMs for large are patterning will be shown in Chapter 3. Chapter 4 introduces electroplating and electroless plating with optics/photonics applications and discusses the device performance both computationally and experimentally. Chapter 5 summarizes achievements.

CHAPTER 2

Soft Lithography: Thermal/UV Nanoimprint Lithography and Metal Transfer Assisted Nanolithography

2.1 Thermal and UV nanoimprint lithography

2.1.1 Overview of the mold fabrications by thermal nanoimprint on fluorocarbon polymer films for the fast roll-to-roll nanoimprint lithography

Roll-to-roll nanoimprint lithography has a great advantage in that the nanopatterning can be performed continuously, which contributes to the high throughput and patterning in a large area. However, some requirements for the roll-to-roll nanoimprint molds make the mold fabrications difficult and challenging, such as flexibility, transparency, and low surface energy of the mold material. Since the nanoimprint mold is wrapped on a roller in the roll-to-roll nanoimprint, it needs to be made by flexible materials, which are typically polymer films or soft and thin metal films (e.g., Ni.) [53–55] When the UV nanoimprint is employed in the roll-to-roll system, either the master mold or the substrate should be transparent so that the UV light can cure the UV curable resin sandwiched by the master mold and substrate. The surface energy of the master mold material also plays an important role because low surface energy can lead to easy demolding after imprinting, and results in a longer master mold lifetime, fewer defects, and faster roll-to-roll imprinting [56]. In terms of the fabrication cost and difficulty of the fabrication processes, polymer films are often used as the master mold materials. However, since UV curable materials are also polymers, they typically have strong adhesions with each other and increase the demolding force. In order to solve this

issue, Fluorocarbon-based polymers are great candidates among polymers, and they have high mechanical strength as well as low surface energy [57]. However, it also makes the mold fabrication somewhat difficult. In this study, two different fluorocarbon-based polymer films, Ethylene-tetrafluoroethylene (ETFE : ETFE-E2, Saint Gobain) and Fluorinated ethylene propylene resin (FEP-FG, Saint Gobain) were employed for the mold fabrications [58,59].

2.1.2 Experimental procedure

As the thermal imprinting molds, two different molds were used: a SiO_2 master mold having gratings with the period of about 550 nm and the depth of about 180 nm with triangular shapes provided by our collaborator and a Si master mold fabricated by photolithography and dry etching. The fabrication process of the Si master is as follows. The starting substrate was 4″ p-type Si (001) wafer. Hexamethyldisilazane (HMDS) was coated on the Si wafer by vapor prime in an oven (YES-310TA (E) : Yield Engineering System). Then a photoresist (Megaposit SPR955 : MicroChem) was spun with the thickness of 0.97 μm followed by a soft bake for 90 seconds at 100 ℃ on a hotplate. Grating patterns with the period of 1.28 μm and the duty cycle of 0.5 were exposed by a stepper (GCA AutoStep) with a dose of 150 mJ/cm^2 in a 2″×2″ area and post baked for 90s at 110 °C. The exposed photoresist was developed by AZ 726 MIF twice for 25 seconds each. The exposed Si surface was dry etched by reactive ion etching (LAM 9400) with 100 sccm of HBr, 100 sccm of He, and 600 W at 30 mTorr for 90 seconds which resulted in 240 nm deep trenches with the smooth and vertical sidewalls. The residual photoresist was removed by O_2 plasma treatment by YES-CV200RFS(E) (Yield Engineering System) with 80 sccm of O_2 and 800

W at 150 °C for 360 seconds. Both master molds were coated with a release agent using Trichloro(octadecyl)silane (OTS) by the silane coupling.

Thermal nanoimprinting was performed by using a hydraulic press tool (Atlas Manual Hydraulic Press 15T GS15011 : Specac) as shown in Figure 2-1. The experimental process is shown in Fig. 2-2. A conformal contact of the master mold to the polymer film is important for thermal nanoimprint to transfer patterns uniformly. Therefore, a silicone rubber sheet and a piece of cleanroom paper were placed on the bottom and top platens respectively. A glass substrate was placed on the rubber sheet to make a flat bottom sandwiching a polymer film by the Si master mold. The top platen was in contact with the cleanroom paper at 180 °C and then the temperature and the pressure were increased to the designated ones. After keeping the temperature and pressure for the designated time, the temperature decreased and the pressure was released at 150 °C. Finally, the demolding of the Si master from the polymer film was done at room temperature. The imprinted polymer films were characterized by the atomic force microscopy (AFM, Dimension ICON AFM : Bruker).

Figure 2-1 A hydraulic manual press tool used for thermal nanoimprint lithography.

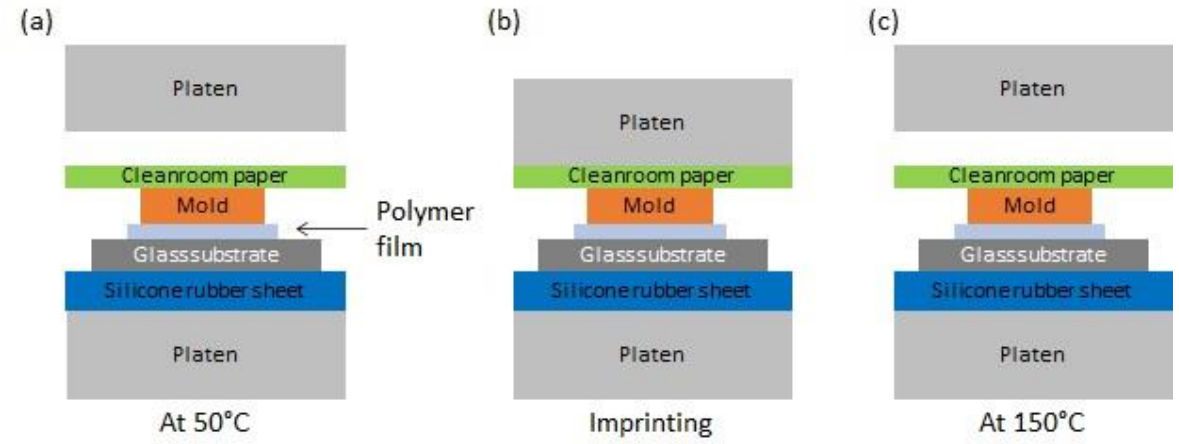

Figure 2-2 Schematics of the thermal nanoimprinting on fluorocarbon-based polymer films.

2.1.3 Results and discussions

The conditions of thermal nanoimprint are shown as Table 2-1 and corresponding AFM images are shown in Figure 2-3. According to the results, there are different optimal nanoimprint conditions for each of ETFE-E2 and FEP-FG films. Since the AFM image of Sample 1 shows no roughness, it is suitable for the following roll-to-roll process. However, as the AFM image of Sample 2 shows, the imprinted ETFE-E2 film under the same condition as Sample 1 has the small roughness on the entire top surface. This roughness was successfully improved by increasing the imprinting temperature and time to 240 °C and 30 minutes respectively. Here, it should be noted that the anti-sticking coating by OTS is very important to reduce the surface roughness, as can be seen by comparing Sample 3 with Sample 4. In addition, even if the imprinting time is 30 minutes, ETFE-E2 films are likely to have the surface roughness at the imprinting temperature of 220 °C. The roughness observed in Sample 8 was not due to inappropriate conditions, but instead due to the unclean surface

Table 2-1 The experimental conditions of the thermal nanoimprint lithography.

Sample No.	Master mold	Film	Temperature (°C)	Pressure (psi)	Time (min)	OTS	Surface smoothness
Sample 1	SiO_2	FEP-FG	220	660	5	○	○
Sample 2	SiO_2	ETFE-E2	220	660	5	○	×
Sample 3	SiO_2	ETFE-E2	240	660	30	×	×
Sample 4	SiO_2	ETFE-E2	240	660	30	○	○
Sample 5	Si	FEP-FG	220	660	30	○	○
Sample 6	Si	FEP-FG	240	660	30	○	○
Sample 7	Si	ETFE-E2	220	660	30	○	△
Sample 8	Si	ETFE-E2	240	660	30	○	○

of the Si master as a result of many nanoimprints.

In order to characterize the topology of an embossed polymer layer in thermal nanoimprint lithography, let us adopt a Kelvin-Voigt linear elastic model where a purely elastic spring and purely viscous damper are connected in parallel as Figure 2-4 shows. E and η are the modulus and the viscosity of the polymer respectively. Provided that the polymer is linearly viscoelastic, from a point-loaded linear-elastic half-space [60], the surface position of the polymer can be written as

$$s(x,y,t) = \frac{-(1-\nu^2)\left(1-e^{-\frac{-Et}{\eta}}\right)}{\pi E\sqrt{x^2+y^2}} \tag{2.1.1}$$

where ν is Poisson's ratio. Here, since E and η are both functions of the temperature T, let us simplify them by the same approximation with the reference [61] by E. Arruda *et al*., and Williams-Landel-Ferry equation respectively,

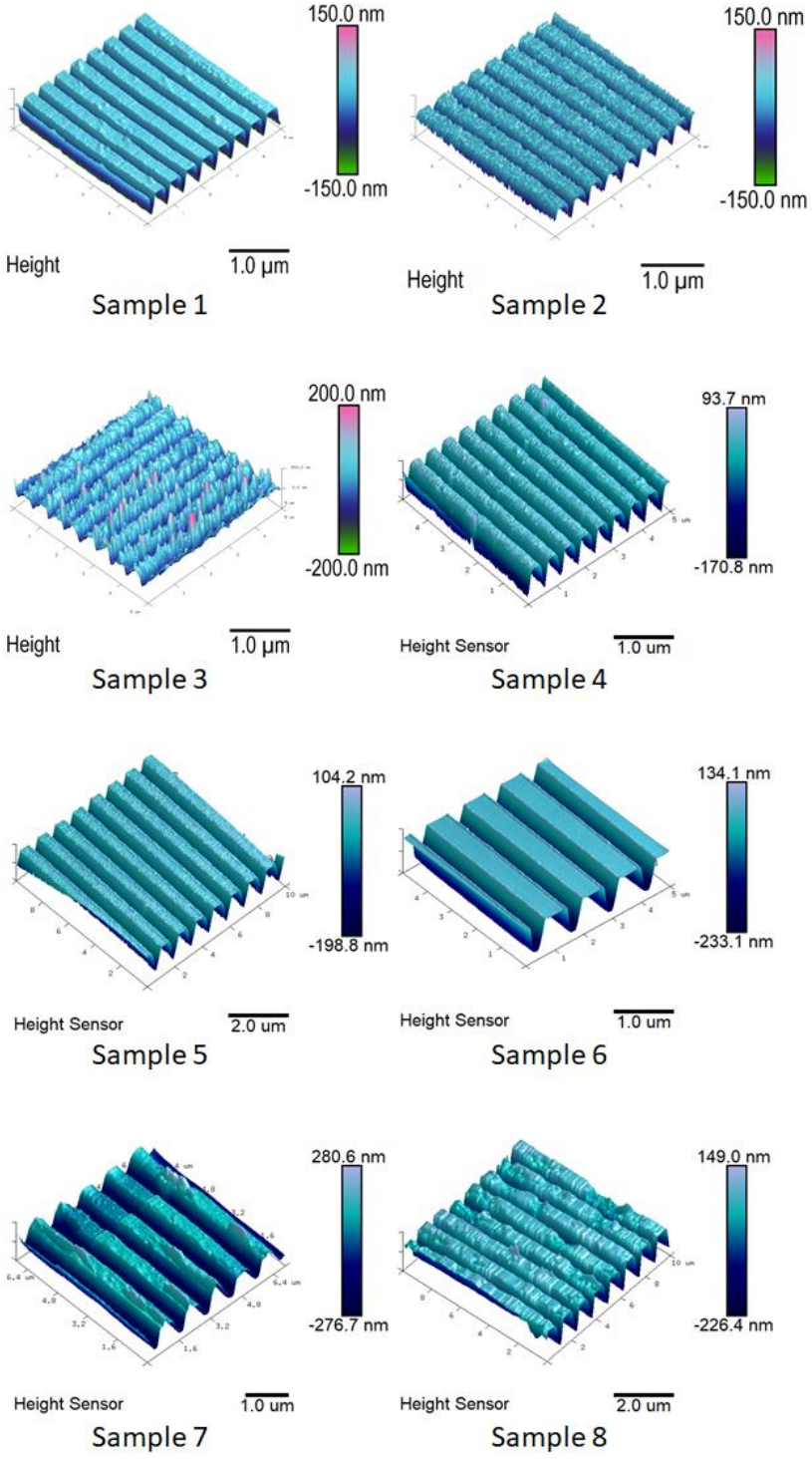

Figure 2-3 AFM images of the imprinted samples 1-8.

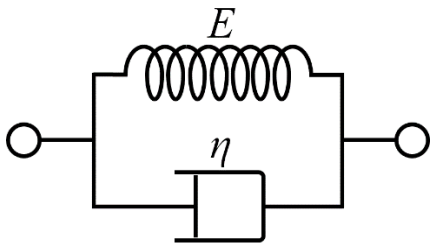

Figure 2-4 A schematic representation of Kelvin-Voigt model.

$$E(T) = 0.5\left(E_g + E_r\right) - 0.5\left(E_g - E_r\right)\tanh\left(\frac{T - T_g}{\Delta T}\right) \tag{2.1.2}$$

$$\eta(T) = \eta_0 \exp\left(\frac{-c_1\left(T - T_g\right)}{c_2 + T - T_g}\right) \tag{2.1.3}$$

wherein E_g and E_r are the elastic moduli at well below and well above the glass transition temperature, and ΔT, c_1, and c_2 are material constants. There is a study on the topography of an embossed polymer film in thermal nanoimprint lithography both experimentally and computationally based on these equations [62]. The study has shown a drastic difference in the filling of cavities with the imprinted polymer only by the imprinting time change from 2 minutes to 30 minutes as shown in Figure 2-5. These results are in agreement with our experimental results which showed that the longer imprint time improved the surface roughness of the imprinted polymer.

Table 2-2 shows a comparison of the material properties of two polymer films employed in this study. Although these two films have almost the same melting points around 250-270°C, their mechanical properties are quite different. Specifically, the tensile modulus

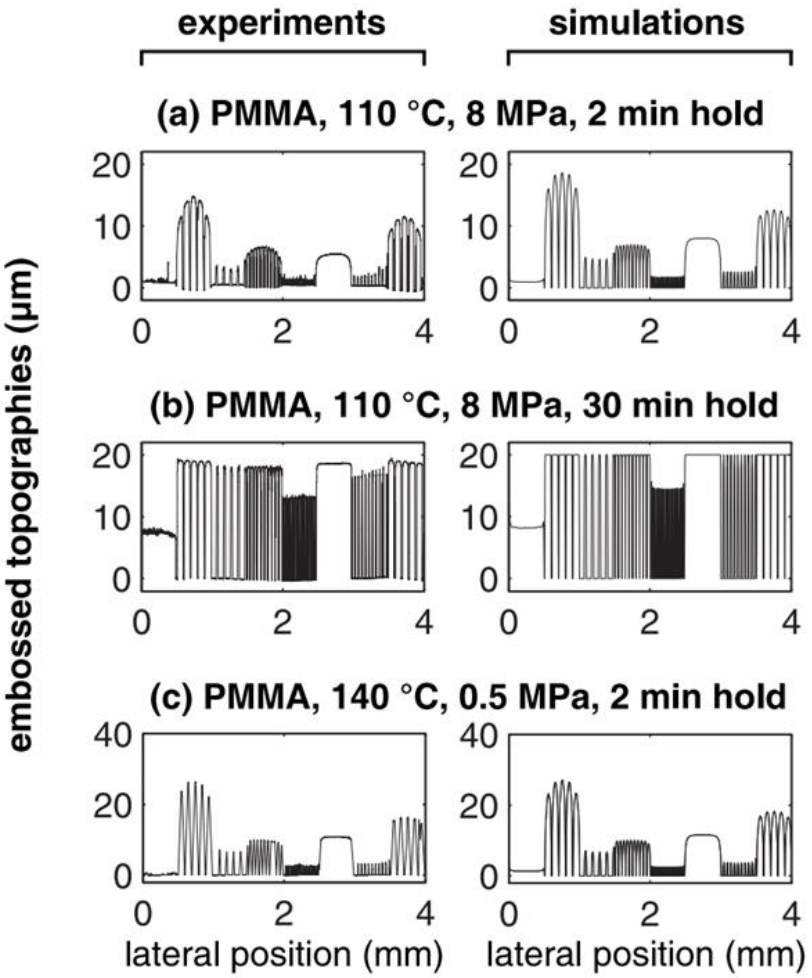

Figure 2-5 An example of experimental and computational results of embossed topographies in thermal nanoimprint lithography with various conditions, adapted from literature [62].

Table 2-2 Material properties of ETFE-E2 and FEP-PG films.

Material properties	Value		Units
	ETFE-E2	FEP-PG	
Tensile strength @Break (RT)	48	24	Mpa
Elongation @Break (RT)	400	300	%
Tensile modulus	1100	480	MPa
Melt Point	250-270	252-282	˚C

Material properties are obtained from the reference [58,59].

of ETFE-E2 is about 2.3 times higher than that of FEP-PG at the room temperature. As can be seen from equation (2.1.1), the higher the tensile modulus becomes, the slower the surface position of the polymer becomes. This is thought to be the reason that a 5-minute imprint time was enough to remove the surface roughness for FEP-PG films, while the longer imprint time was required for ETFE-E2 films.

2.1.4 Overview of the UV nanoimprint lithography for photo collector device replication

As an alternative to fossil fuels, there is a huge demand for utilizing renewable energies. Solar energy is a particularly promising resource among them, and there have been many studies to reduce the fabrication costs and increase their efficiency for photovoltaics [63,64]. However, the current photovoltaics technology requires more improvements to its battery energy storage system. On the other hand, the energy harvested from solar thermal energy has an advantage in that the energy storage technology is less expensive, and the energy is accessible from day to night and year around [65,66]. To maximize the efficiency, concentrated solar power technologies such as a planar focusing

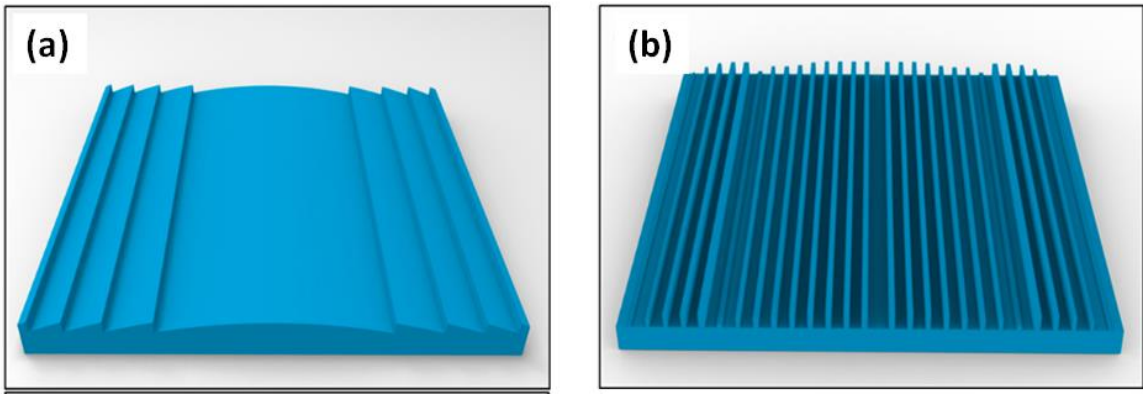

Figure 2-6 (a) A simple planar focusing collector and (b) a complicated one, adapted from literature [67]. Copyrights (2018) ACS.

collector have been employed [67], and there is a huge demand to fabricate such structures at a low cost for the sake of commercialization competing with fossil fuel energy. Nanoimprint lithography is one of the most promising methods to achieve this, due to the scalability and cost efficiency.

Simple structures such as the planar focusing collector shown as Figure 2-6 (a) are easily replicated by the nanoimprint lithography, and we employed high modulus PDMS for fabricating a replica mold and Silsesquioxane (SSQ) for another replication [68]. However, there are still several points to be improved. First, the high modulus PDMS itself is not mechanically strong enough to stand without a supporting substrate. Therefore, it is required to spincoat a thin layer on the master mold, resulting in a waste of the high modulus PDMS dropped on it, and a regular PDMS is typically employed to support the thin high modulus PDMS layer because of their affinity. This process makes the curing time very long (~1h). Second, the high modulus PDMS needs to be synthesized right before the spincoating since they start curing right after they are mixed. Lastly, replicating high aspect ratio structures with microns to sib-micron width patterns often results in some defects or fillings in the patterns because of the insufficient ability to replicate such structures. In one recent study, a new design with higher efficiency such as Figure 2-6 (b) has been suggested [67], and it consists of more complicated patterns with higher aspect ratios than the old one, which makes replication very difficult.

2.1.5 Replication of very fine structures by Polyurethane Acrylate

Replication of fine structures, particularly high aspect ratio structures, is one of the

most challenging processes in nanoimprint lithography because of its fragility and difficulty in demolding. The requirements for UV resins in those applications are high mechanical strength, low viscosity which enables high-fidelity replications, and moderately low surface energy that allows for easy demolding while maintaining the sufficient adhesion to the substrate. Here, a UV curable resin, Polyurethane Acrylate (PUA : PUM311, MCNET Co., Ltd) was employed to overcome the challenges of replicating high aspect ratio structures with a small feature size [69,70].

The chemical structure of PUA and reaction scheme is shown in Figure 2-7 [71]. The most unique characteristic of PUA is the ability of the self-replication, that is, PUA can be used as both the master mold and nanoimprint resist at the same time. When typical UV curable resins are used in this way, they crosslink with each other and cannot be separated after the UV curing. However, if PUA is used as the master mold material and overcured before another UV nanoimprint lithography, PUA can also be used as the UV nanoimprint resist and easily separated even after the UV curing. This is because overcuring can remove trapped polymer radicals and remaining unsaturated acrylate [71]. This characteristic is very helpful for various applications, since replications of either of the original pattern of the master mold or the reverse pattern are possible by the same material, which easily enables the 2nd replica fabrication. The concentrating solar power device to be replicated here is a metasurface planar focusing collector design as shown in Figure 2-6(b). Since it was fabricated by the two-photon lithography, it is not suitable for mass production and the motivation to apply the nanoimprint lithography. The experimental flow of the PUA replication is shown in Figure 2-8. This process is much simpler than the one previously used

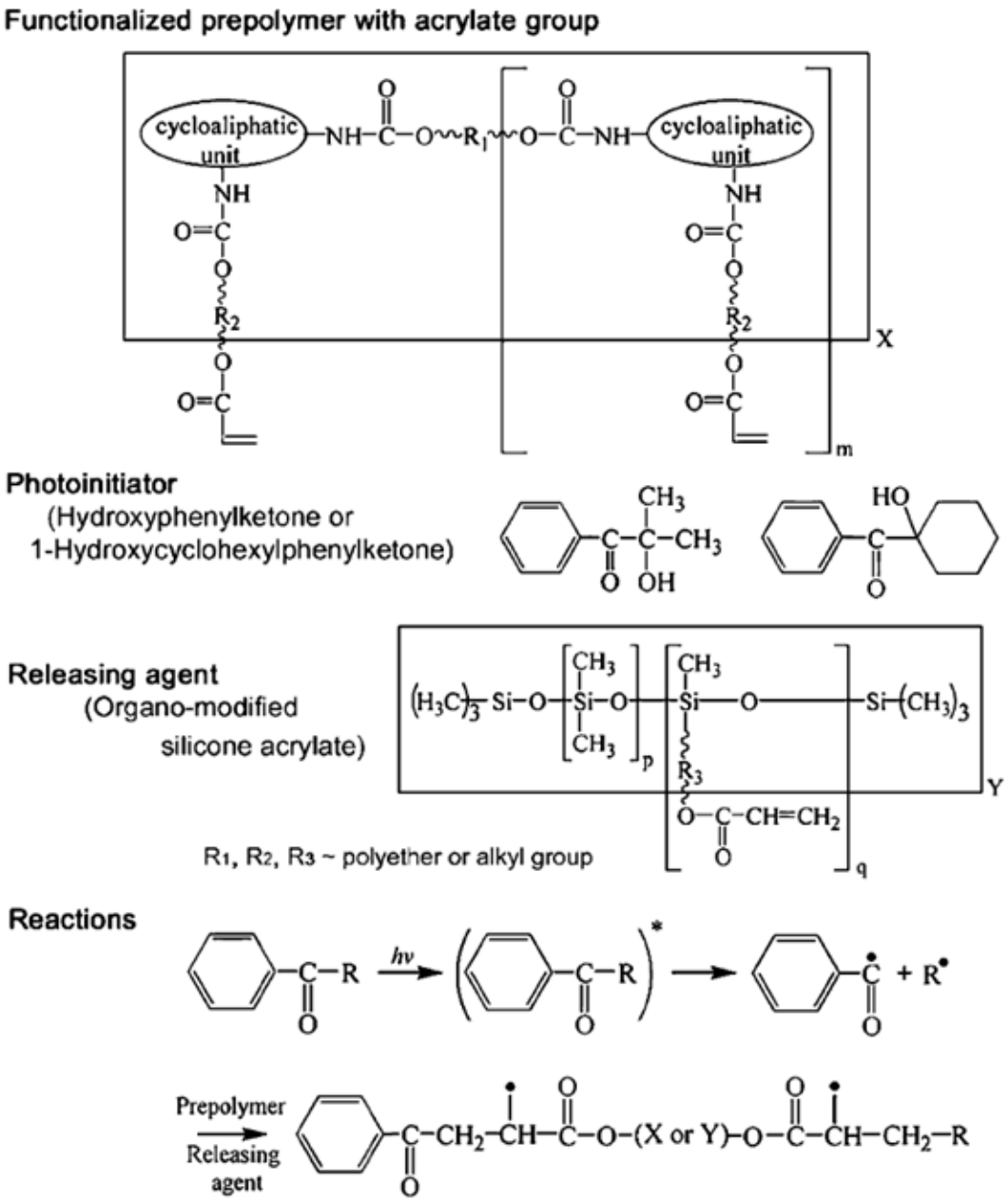

[a] X and Y denote the unchanged fragments during the photo-polymerization process.

Figure 2-7 The chemical structures of the PUA and photoinitiator, and the curing reactions by UV exposure, adapted from literature [71]. Copyright (2004) ACS.

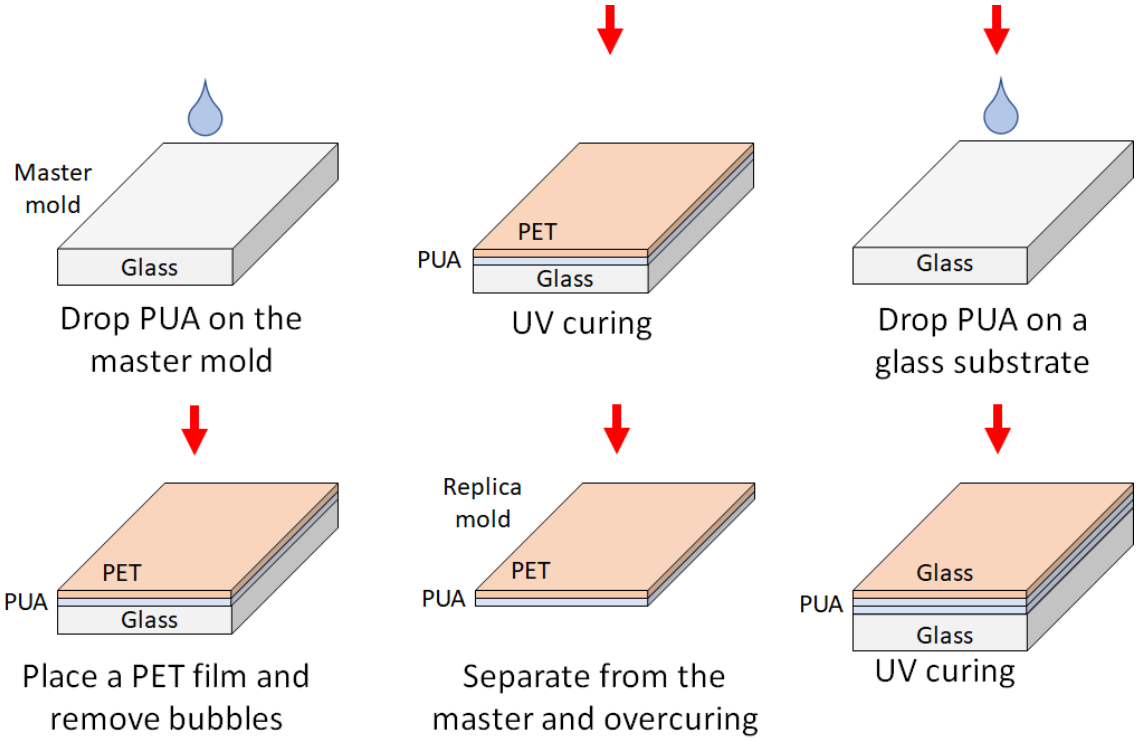

Figure 2-8 A replication process flow for the metasurface planar focusing collector by PUA.

by high modulus PMDS and the processing time could be a few minutes when a comparably strong UV light is used for curing. SEM images of the replicated patterns by both methods using high modulus PDMS and PUA are shown in Figure 2-9. The one fabricated by PUA shows no defects or fillings between the structures, and the replication fidelity is very high even for the high aspect ratio structures. This work has been published as part of the reference [67].

2.2 Metal transfer assisted nanolithography

2.2.1 Metal transfer assisted nanolithography by PMMA and Au/Ti films

Soft lithography technologies are not limited to imprint patterns but can also transfer

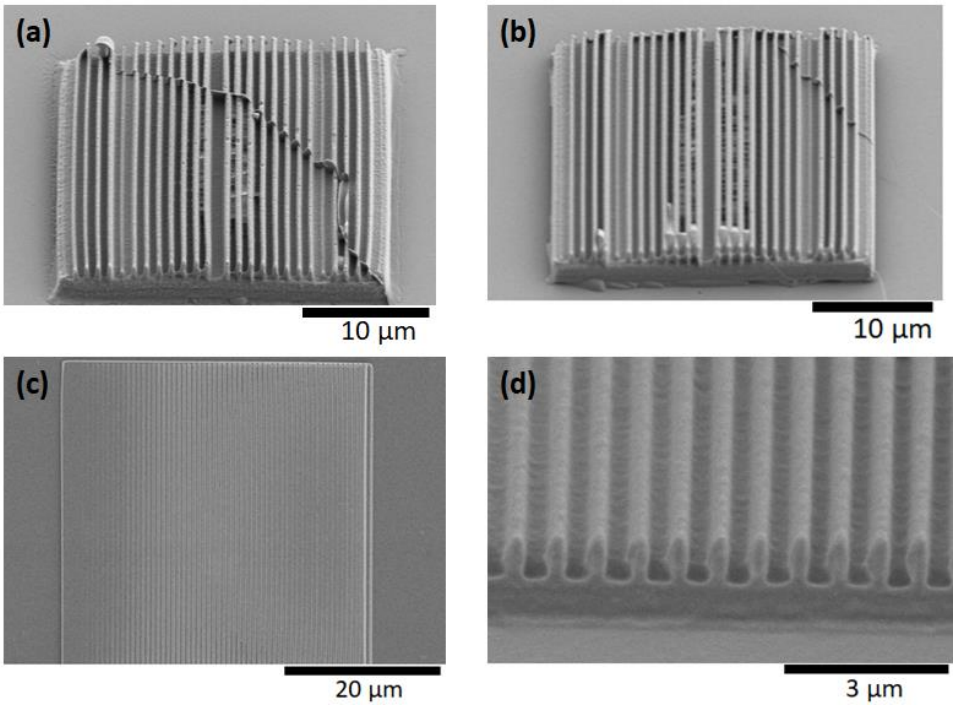

Figure 2-9 The replicated metasurface planar focusing collectors (a) and (b) by high modulus PDMS and (c) by PUA. (a) The structures were partially destroyed because of the fragility of high modulus PDMS. (b) Fillings between the structures were observed because of the low fidelity of the replication. (c) The PUA replica shows no destruction or fillings and (d) the cross-sectional image shows high-fidelity replication even for the high aspect ratio structures.

patterns from the master mold to the substrate. Metal transfer-assisted nanolithography has been reported for the first time in 2008 [31] and it shows that it is capable of making nanopatterns on various kinds of substrates, uniformly, in a large area without employing any complicated processes. The experimental procedure of metal transfer assisted nanolithography is shown in Fig. 2-10. The principle of metal transfer assisted nanolithography is simply based on the difference in the surface energies of the stamp and substrate, PDMS and PMMA respectively in the first report. The processing temperature that

is slightly higher than the glass transition temperature of PMMA also contributes to the pattern transfer by creating a conformal contact at the interface. However, since this technique uses PMMA as the intermediate polymer layer, the process temperature must be over 100 C˚, which is the glass transition temperature of PMMA. This limits the compatibility of the materials for the substrate, especially when polymer films are employed. Moreover, because of the small difference in the surface energy between PDMS and PMMA, the choices of the metal films are also limited to Au/Ti. In order to improve these aspects, the extended process of metal transfer assisted nanolithography using UV curable polymers is discussed.

2.2.2 Theoretical study on transfer printing technologies

As represented by template stripping, reported for the first time in 1993 [72], transfer printing technologies have attracted a lot of attention, and their importance has been increasing with emerging demands for flexible electronics [73–76]. Feng *et al*., has studied

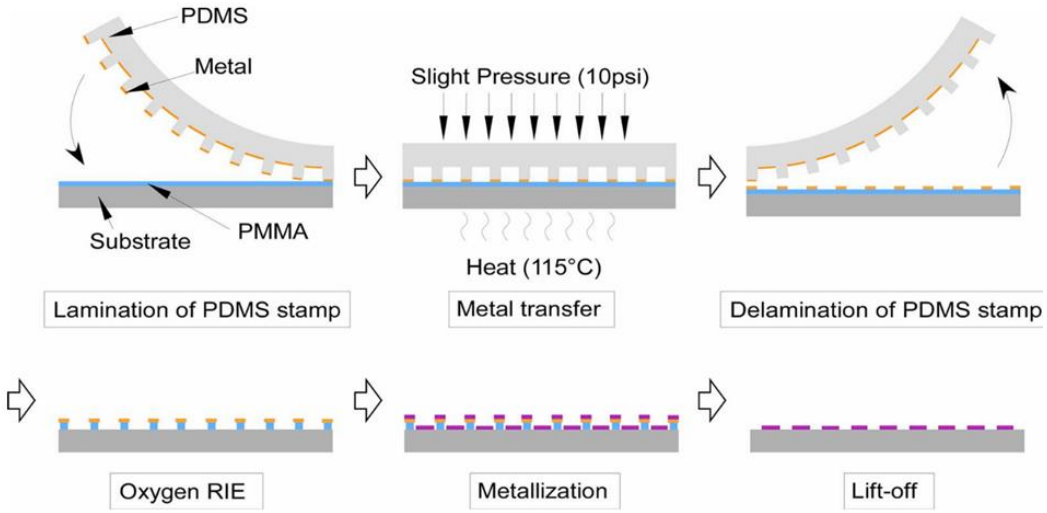

Figure 2-10 Schematics of metal transfer-assisted nanolithography using PMMA, adapted from literature [31]. Copyright (2008) AIP Publishing.

the mechanism of transfer printing and characterized the conditions for the pick-up and printing process [77]. Figure 2-11 (a) shows a schematic of the peel test. *F* represents a peel force, *v* is a steady-state speed when the stamp is peeled off from the substrate, and *G* is the energy release rate expressed by

$$G = \frac{F}{w} \tag{2.2.1}$$

where *w* is the width of the stamp. This parameter *G* accounts for both the energy of interfacial bond breaking and viscoelastic dissipation around the crack tip. The important parameter for transfer printing is the critical energy release rate where the crack propagates steadily. Considering the critical energy release rates at the two interfaces as Figure 2-11 (b) and (c), pick-up and printing processes can be modeled. Here, the critical energy release rates at the two interfaces of the stamp and film, and the film and substrate are represented by $G_{\text{crit}}^{\text{stamp/film}}$ and $G_{\text{crit}}^{\text{film/substrate}}$ respectively. When the energy release rate reaches $G_{\text{crit}}^{\text{film/substrate}}$ pick-up occurs, and printing does so when it reaches $G_{\text{crit}}^{\text{stamp/film}}(v)$. It should be clarified that the critical energy release rate at the interface of the stamp and film is a

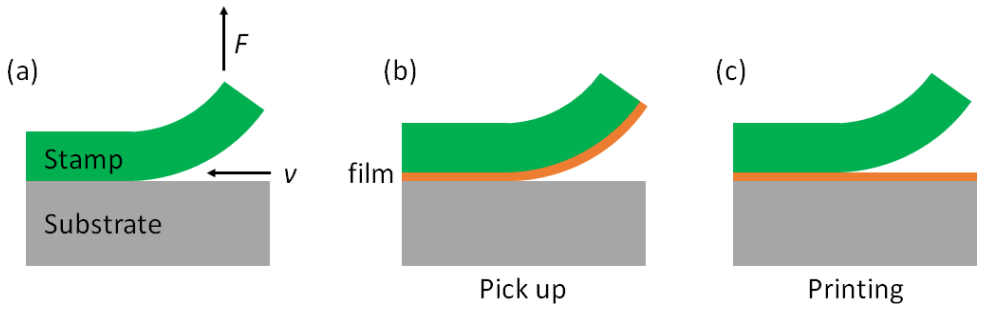

Figure 2-11 Schematics of (a) the peel test, (b) pick-up, and (c) printing in transfer printing.

function of the peeling speed since the energy dissipation in the viscoelastic stamp increases with the peeling speed. Therefore, the conditions for the two different phenomena, pick-up and printing, can be expressed by the following equations,

$$G_{\text{crit}}^{\text{film/substrate}} < G_{\text{crit}}^{\text{stamp/film}}(v) \text{ for pickup} \tag{2.2.2}$$

$$G_{\text{crit}}^{\text{film/substrate}} > G_{\text{crit}}^{\text{stamp/film}}(v) \text{ for printing} \tag{2.2.3}$$

and these are shown in Figure 2-12.

When this theory for transfer printing is applied to metal transfer assisted nanolithography, only the printing condition is our best interest since the film is directly deposited on the stamp by thermal evaporation. For the best result, the condition where $G_{\text{crit}}^{\text{film/substrate}}$ is much higher than $G_{\text{crit}}^{\text{stamp/film}}(v)$ is preferred. As described in equation (2.2.1), when the width becomes smaller, the critical energy release rate becomes larger. Therefore, however large the peeling speed is, printing will be dominant. Lowering the

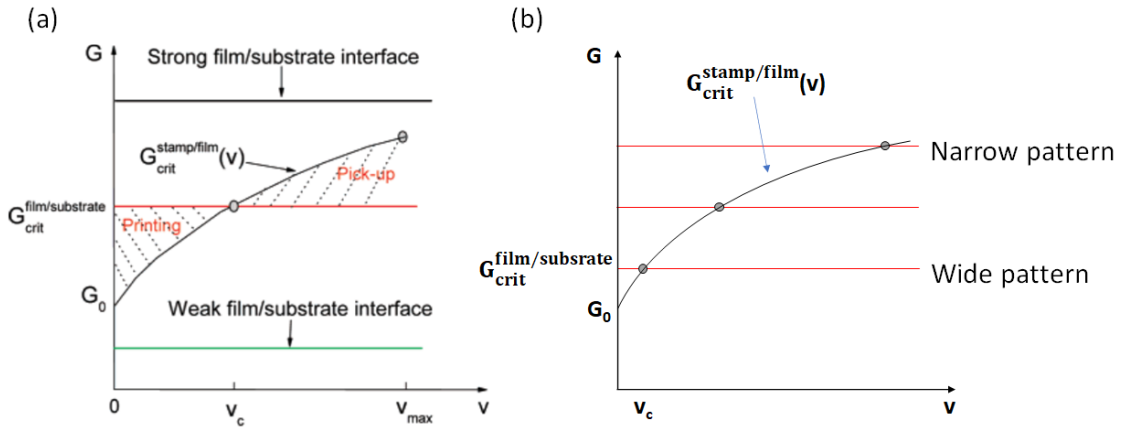

Figure 2-12 (a) Schematic diagram for pick-up and printing conditions in transfer printing, adapted from literature [77]. Copyright (2007) ACS. (b) Two difference cases where the transferred pattern width is narrow and wide.

peeling speed is easy to implement, so this process tends to be successful. According to the reference [31], metal gratings with a line width of 100 nm were successfully transferred on a PMMA layer. However, it was very difficult to transfer 650 nm wide metal gratings with the same conditions on a PMMA layer without any defects as shown in Figure 2-13. This result can be explained in terms of the difference in $G_{\mathrm{crit}}^{\mathrm{film/substrate}}$ for different width as Figure 2-12 (b) shows. From the next section, a modified process to improve this challenge will be introduced.

2.2.3 Metal transfer assisted nanolithography by SU-8

SU-8 is known as an i-line negative photoresist and usually used for device applications where the photoresist stays permanently as a part of the device, e.g., micro electromechanical systems. However, we found out that when SU-8 is employed at the

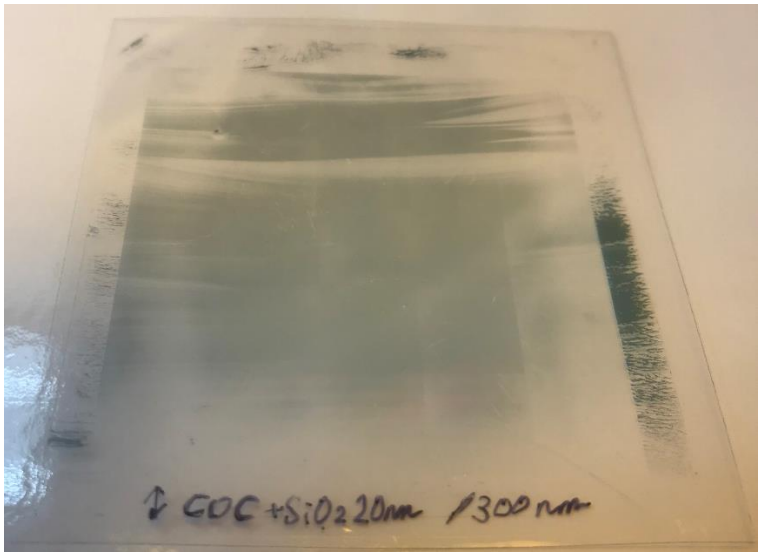

Figure 2-13 A picture of transferred metal gratings with 650 nm line width on a PMMA layer coated on a Cyclic Olefin Copolymer film.

intermediate layer in the metal transfer assisted nanolithography, it can improve the uniformity of the transferred patterns as well as expand the compatibility of the materials for the substrate and transferred films. Since SU-8 cannot be lifted off easily, this process is basically for applications where the SU-8 layer will be incorporated as a part of the device unlike the original metal transfer assisted nanolithography. However, due to the wider material compatibility, this technology can be used to fabricate flexible devices at a low cost.

2.2.3.1 Experimental procedure

A schematic of the experimental flow is shown in Figure 2-14. The Si master mold used for replicating PDMS stamps here was fabricated in the same way described in section 2.1. The period of the mold is 1.3 μm with the duty cycle of 0.5, and the grating height is about 600 nm. First, PDMS (Sylgard 184 : Dow) was prepared by mixing the two parts with a ratio of 10:1 and poured onto the Si master mold. Then it was put in a desiccator and pumped down for 30 minutes to remove bubbles trapped in the PDMS. Finally, the PDMS was cured on a hotplate at 80 C˚ for 2 h and delaminated from the Si master mold. Metal films which would be transferred by the metal transfer assisted nanolithography were deposited on the PDMS stamps by electron beam evaporation in the evaporator (Angstrom Engineering Inc.). Not only Au/Ti with 10 nm/5 nm films but also 30 nm of an Al film were chosen, which is impossible to transfer by the metal transfer assisted nanolithography by PMMA. SU-8 with various solid concentrations were prepared by diluting SU-8 2005 with Cyclopentanone aiming for spincoating various thicknesses of SU-8. Those SU-8 were spun on a PET film fixed on a Si wafer and metal transfer assisted nanolithography was performed

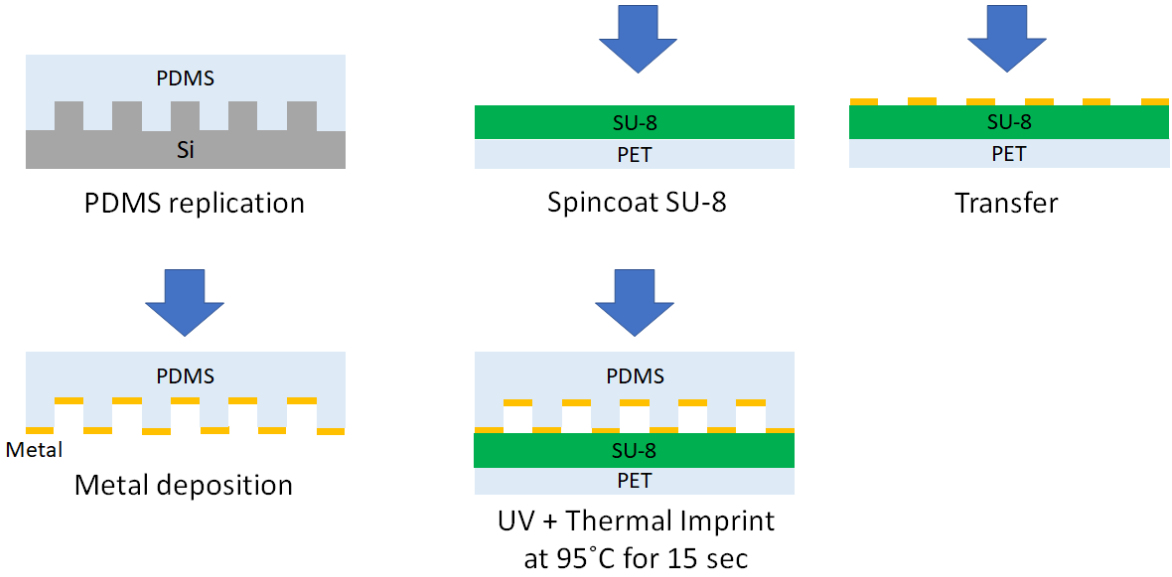

Figure 2-14 A schematic of the experimental flow for metal transfer assisted nanolithography by SU-8.

by the nanoimprinter (NX-2000 : Nanonex) with 15 psi for 15 seconds at 95°C. Then, the transferred patterns were characterized by SEM and AFM.

2.2.3.2 Results and discussions

Figure 2-15 shows the cross-sectional SEM images of the transferred Al gratings for three different thicknesses of the spincoated SU-8, 5 μm, 160 nm, and 40 nm. In the case that the SU-8 layer was thick enough, it was nanoimprinted by the PDMS stamp even with as low as 15 psi and for as short as 15 seconds. As a result, the SU-8 layer made conformal contact on the both top and bottom metal films deposited on the PDMS stamp, and they were transferred onto the SU-8 layer as Figure 2-15 (a) shows. This could be a useful technique to transfer the devices fabricated on a PDMS stamp to any substrates at a low cost since the PDMS stamp can be reused many times. However, unlike the original metal transfer assisted

nanolithography with PMMA, it cannot selectively transfer the films on the top of the patterns. Then, it is found that decreasing the spincoated SU-8 thickness resulted in different scenarios. When the SU-8 thickness was 160 nm, which is much smaller than the stamp height, the SU-8 layer was still imprinted, but not high enough to contact the bottom of the PDMS stamp. Thus, the metal films on the bottom of the PDMS stamp were not transferred to the substrate. In an extreme case where the SU-8 thickness was 40 nm, deformation of the SU-8 layer did not occur, but the metal films on the top of the PDMS stamp were successfully transferred to the substrate. This result is similar to when PMMA is employed. Figure 2-16 shows the transferred Al gratings on the 40 nm SU-8 layer with high fidelity.

These results could be interpreted by relating to the residual layer in nanoimprint lithography. It is known in nanoimprint lithography that the master mold does not extrude the nanoimprint resist until it reaches the substrate surface, even though the resist thickness is smaller than the master mold's height, i.e., there is a residual layer left on the substrate [78]. Lee and Jung have investigated the residual layer thickness in UV nanoimprint lithography with different imprint pressures [79]. According to their results, UV curable resist can be

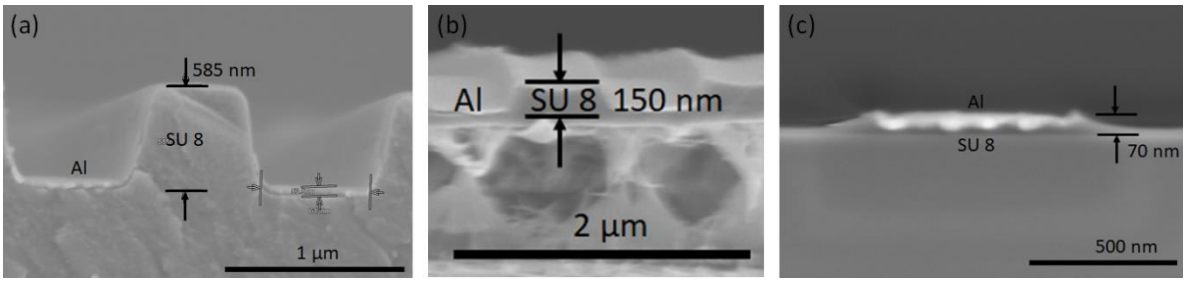

Figure 2-15 SEM images of the results of metal transfer assisted nanolithography with SU-8 with the SU-8 thickness of (a) 5µm, (b) 160 nm, and (c) 40 nm.

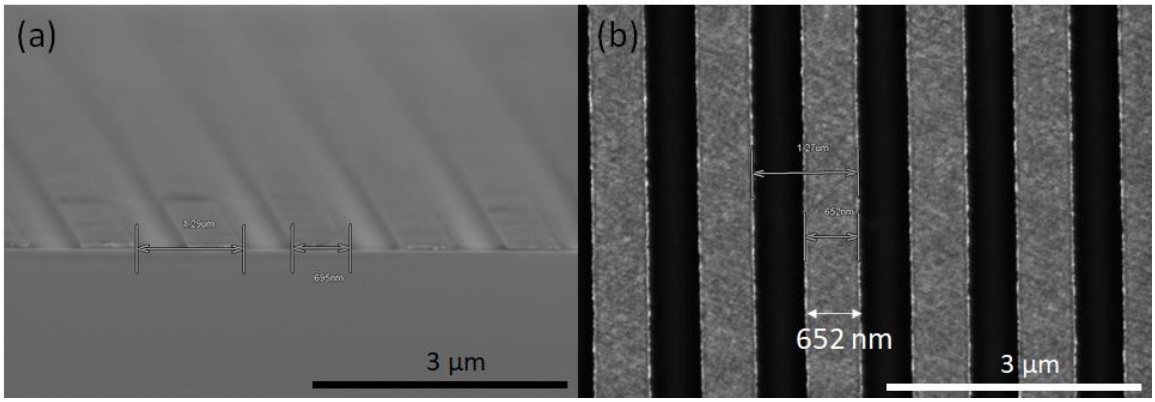

Figure 2-16 SEM images of the transferred Al gratings on the 40 nm thick SU-8 layer. (a) A cross-sectional image and (b) top view.

imprinted only by the vacuum suction, with no pressurization, and the higher the imprint pressure gets, the smaller the residual layer thickness becomes. This also supports the experimental results shown here, and 40 nm SU-8 is thought to be less than the residual layer thickness for the imprinting pressure of 15 psi.

Next, the surface morphology of the transferred metal films was also characterized by AFM and SEM. Figure 2-17 (a) shows the AFM measurement on the transferred Al gratings along both horizontal and vertical directions. The transferred films show peaks at both edges, which are interpreted as the metal film from the sidewalls of the PDMS stamp, since the gratings on the master mold are not completely vertical. Along the grating direction, the fluctuation of the metal film was observed. The roughness was clearly seen in tilted SEM images and the 3D AFM image as Figure 2-17 (b)-(d) show. Therefore, it can be concluded that this process is useful to fabricate devices when the surface roughness of the films does not affect the device function.

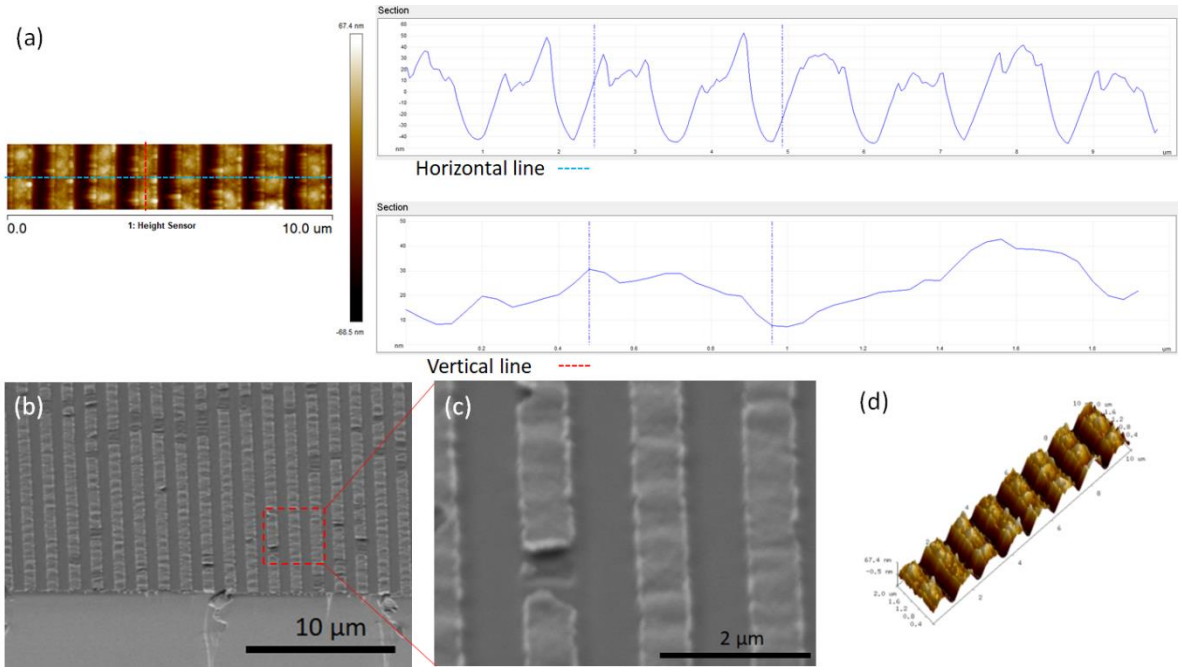

Figure 2-17 Characterizations of the transferred Al films by AFM and SEM. (a) AFM measurements perpendicular to and along the gratings. (b) A SEM image of the gratings and (c) the close image. (d) A 3D AFM image of the gratings.

2.2.4 Metal transfer assisted nanolithography by KMPR

2.2.4.1 Experimental procedure

KMPR is also known as a UV curable photoresist like SU-8 but removable by solvents even after the cure. Therefore, it can be used to replace PMMA in metal transfer assisted nanolithography while utilizing the properties of KMPR to expand the compatibility of materials as SU-8.

The same Si master mold used in the previous section was employed. Only Au/Ti with 10 nm/5 nm were chosen as the deposited metal films since they are used as the etching masks to make devices by following evaporations, but this process does not limit the

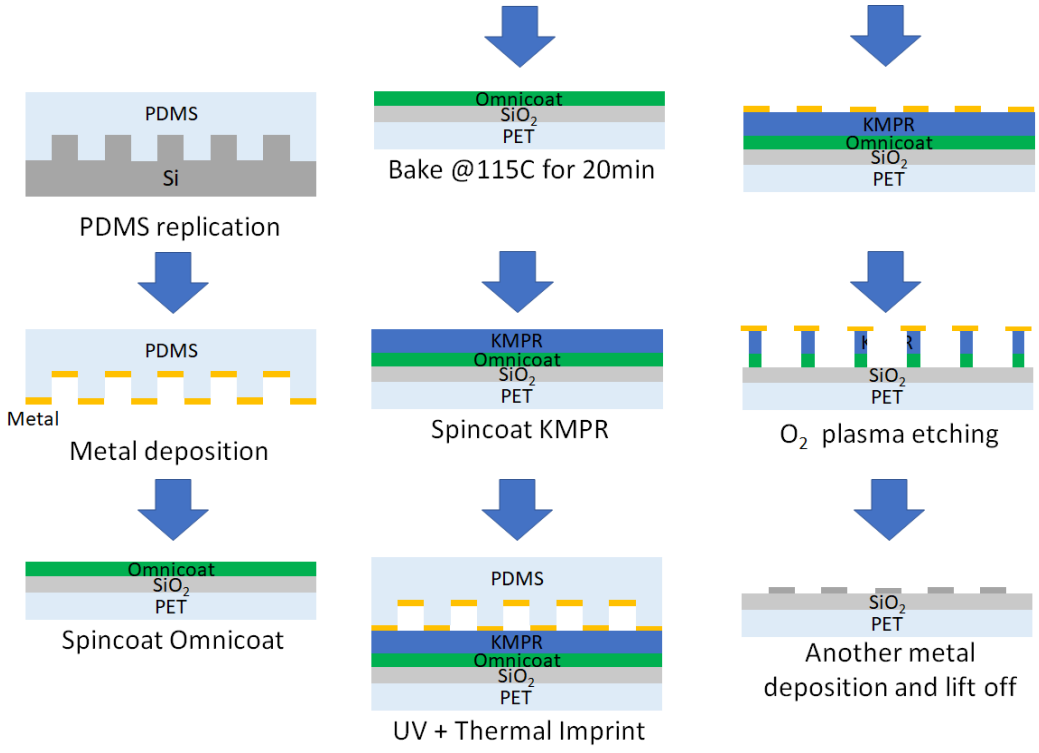

Figure 2-18 A process flow of metal transfer assisted nanolithography with KMPR.

materials choices to Au/Ti films. A PET film was used as a substrate that the metal films were transferred onto. The process flow is shown in Figure 2-18. PET films were cleaned by ultrasonication in Acetone and IPA for 5 minutes respectively. 500 nm SU-8 was spun on the PET film and it is prebaked at 95 C˚ for 1 minute, exposed by UV light (MJB45S : Karl Suss) for 20 seconds, and post baked at 95 C˚ for 1 minute. Then 20 nm of SiO_2 was deposited on the PET film as the etching stopper layer for the O_2 plasma etching. Diluted KMPR with the solid concentration of 2% was prepared by mixing KMPR 1010 with Cyclopentanone. First, OmniCoat (Kayaku Advanced Materials) was spun on the PET film fixed on a Si wafer and then baked on a hotplate at 115 C˚ for 20 minutes. After it was cooled to room temperature, the diluted KMPR was spun on it. The metal transfer assisted nanolithography was performed

by NX-2000 with the following conditions: an imprinting temperature of 70 C°, an imprinting time of 5 minutes, an imprinting pressure of 6 psi, and UV exposure for 15 seconds at the last 15 seconds of the imprinting time. Then, the photoresist was dry etched by O_2 plasma (YES-310TA (E) : Yield Engineering System) with 35 sccm of O_2 and 100 W at 60 °C for 450 seconds using the transferred metal films as the etching mask. A 24 nm thick Al layer was evaporated through the transferred metal films and then the photoresist was lifted off by Remover PG (Kayaku Advanced Materials) at 80 C° for 30-60 seconds with ultrasonication.

2.2.4.2 Results and discussions

A picture of the transferred metal films on the KMPR coated PET film is shown in Figure 2-19. The PET film fixed on the Si wafer shows the strong light interferences by the metal gratings, and the PDMS stamp still shows dark color in the pattern caused by the residual metal films on the bottom. After the O_2 plasma etching, the transferred metal films helped to create gratings with the undercuts, which made it easy for Remover PG to attack the KMPR layer as the red arrows in Figure 2-20 (a) indicate even after another metal film is evaporated. The Al gratings fabricated on the PET film is shown in Figure 2-20 (b). By employing KMPR instead of PMMA, the uniformity issue has been completely resolved in a large area, and the process has successfully resolved the thermal deformation issue when PET films are used as the substrate.

One of the advantages of the metal transfer assisted nanolithography is that polymer films are also compatible. It is usually difficult to fabricate nano patterns using the common semiconductor nanofabrication technologies such as photolithography, electron beam

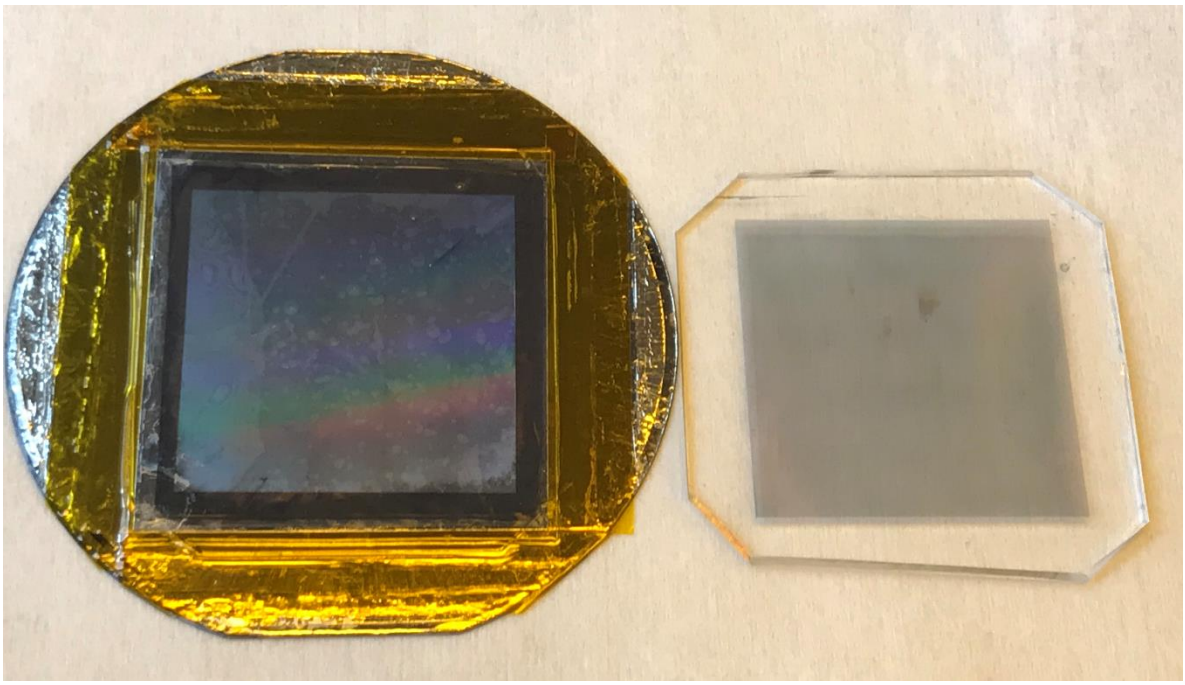

Figure 2-19 The left is the transferred Au/Ti films on the KMPR coated PET film and the right is the PDMS stamp used for it. There are residual metal films on the bottom of the PDMS stamp.

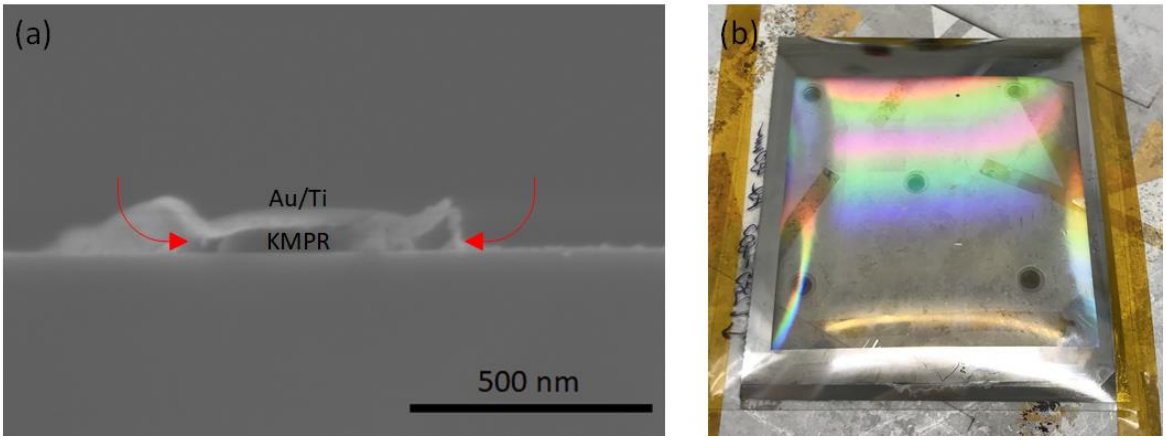

Figure 2-20 (a) A cross-sectional SEM image of the single grating fabricated by O_2 plasma etching using the transferred Au/Ti film as an etching mask. (b) Al gratings made on a PET film using metal transfer assisted nanolithography with KMPR in a 5 cm × 5 cm area.

lithography, or vacuum processes because of its transparency, low heat resistance, and contamination under the high vacuum. However, some special treatments are required when polymer film substrates are employed.

First, since the surface roughness of polymer films is typically not as smooth as Si wafers, surface planarization is important to obtain the uniform patterns in height, i.e., without the surface planarization, the transferred patterns tend to have differences in height with nanometer scale. A comparison of two AFM measurements with and without the surface planarization is shown in Figure 2-21. The top image shows the patterns transferred directly on a PET film with SU-8 as the transfer layer, and the bottom one is on a PET film planarized by spincoated SU-8 prior to the metal transfer assisted nanolithography. While the bottom line of the patterns without planarization has fluctuations, they have successfully been removed by the planarized SU-8 layer beneath the metal gratings.

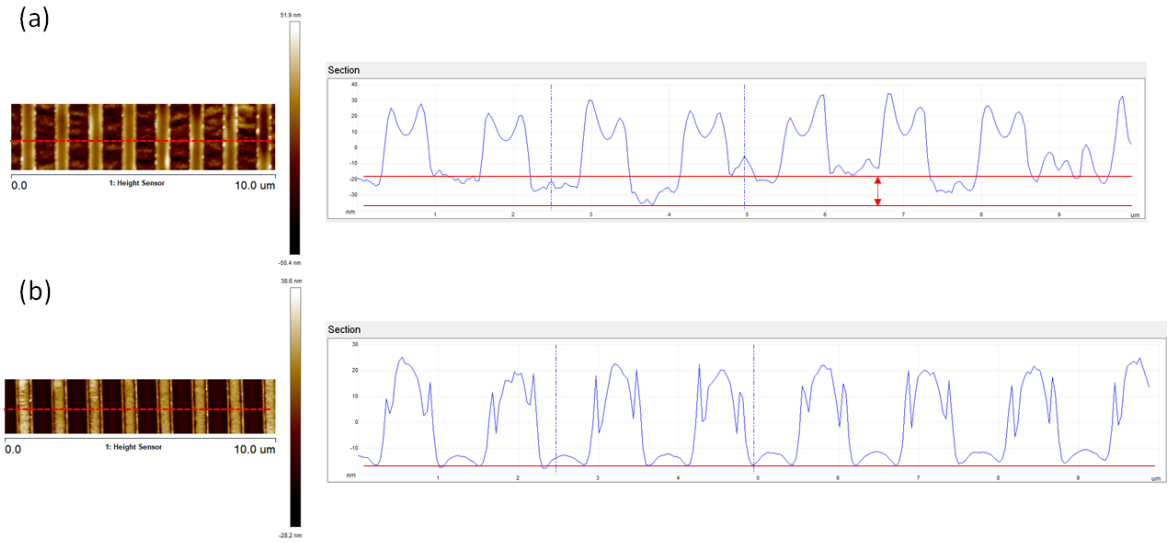

Figure 2-21 AFM images on transferred metal films (a) without the planarization and (b) with the planarization by SU-8.

When KMPR is employed as the transfer layer and dry etching process is followed through the transferred metal films, an etching stopper layer is required to ensure the KMPR layer is etched without residue, but the substrate is not etched. Otherwise, the polymer substrate is also etched by dry etching after the KMPR layer is completely etched away. Considering the compatibility with many semiconductor fabrication processes, a thin SiO_2 layer is recommended as an etching stopper. Therefore, the actual fabrication process requires the surface planarization by SU-8 first, and a thin (~20 nm) SiO_2 deposition as described in the section 2.2.4.1. However, it turned out that the thickness of the SU-8 layer for planarization also plays an important role when the KMPR layer is lifted off by remover PG. In case of the thick SU-8 layer (> 1 μm), it is easy to peel off during the lift off with a sonication since the adhesion of SU-8 to a PET film is not strong enough. On the other hand, a thin SU-8 layer (< 100 nm) has another issue that remover PG attacks the SiO_2 layer and creates large defects as the SiO_2 layer has grain boundaries corresponding to the PET film roughness. Figure 2-22 is microscope images when PET films with thin film coatings are immersed in a solvent. Figure 2-22 (a) is a successful sample showing Al gratings made on 500 nm SU-8 and 20 nm SiO_2. Figure 2-22 (b)-(d) shows the test results with different materials and thicknesses on PET films. They were immersed in Remover PG without any patterns on them, but large defects were observed on the surfaces of the samples regardless of materials or thickness of the films. Therefore, it can be concluded that 500 nm SU-8 layer with 20 nm SiO_2 film are very effective in solving the defect issues caused by the lift-off process when polymer films are employed as the substrate in metal transfer assisted nanolithography.

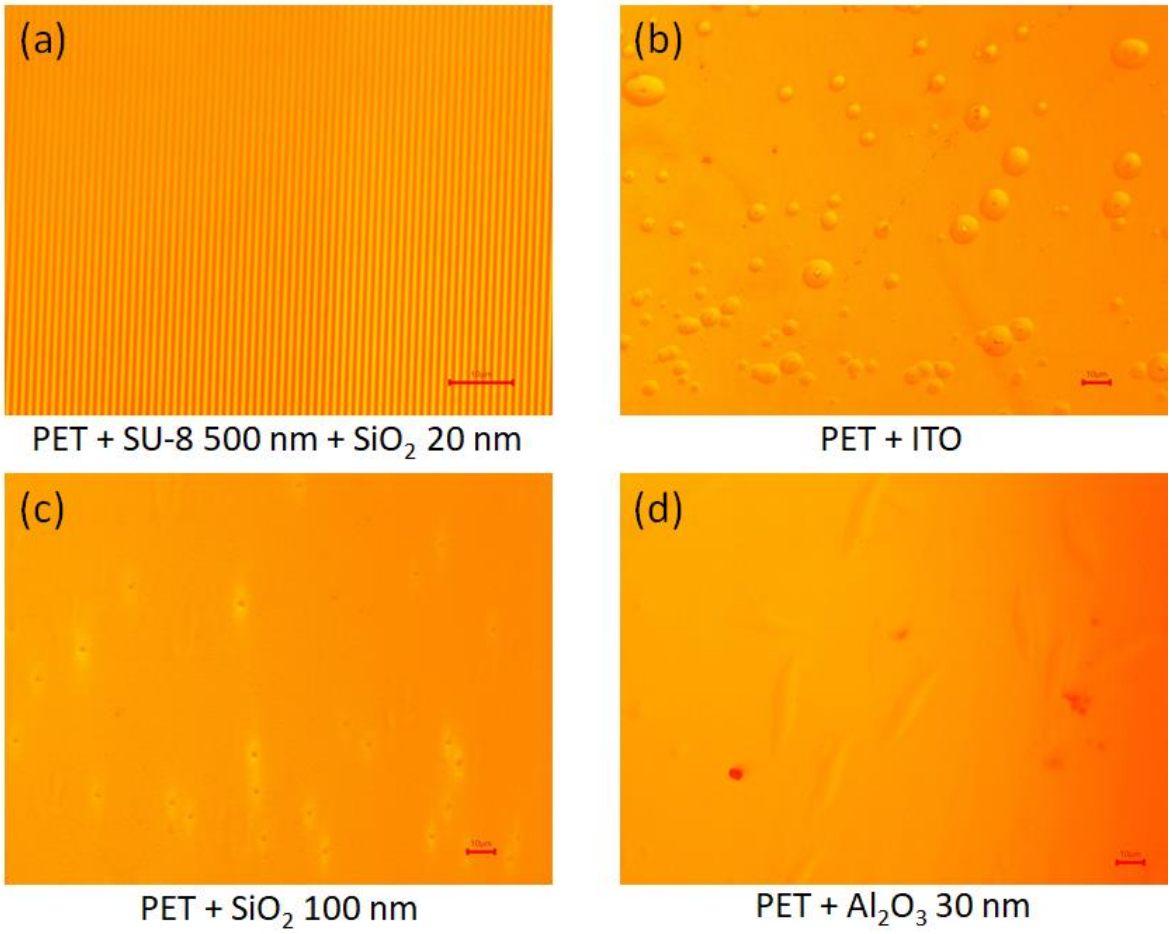

Figure 2-22 (a) Al gratings successfully fabricated on a PET film without any defects. The immersion test results in Remover PG with (b) an ITO film, (c) a 100 nm SiO_2 film, and (d) a 30 nm Al_2O_3 film.

2.3 Summary

In this chapter, two major nanoimprint lithography technologies, thermal nanoimprint and UV nanoimprint were introduced, and experiments were performed to resolve previous issues. The newly developed technology based on the aforementioned nanoimprint lithography and transfer printing technique was also performed to obtain nano patterns on

polymer films with high uniformity and compatibility. This technology is not only able to decrease the cost of fabricating nano structures on polymer films, but it can also extend the potential applications for transparent/flexible electronics technologies.

CHAPTER 3

Large Area Plasmonic Photo Roller Lithography

3.1 Plasmonic lithography

In 2000, Pendry reported the concept of a perfect lens using negative refractive index materials [37], which can resolve patterns smaller than the diffraction limit of light utilizing evanescent waves. Since then, there have been many studies on developing new technologies based on this concept [33,36,39–41,80–84]. Among them, there has been intensive research on plasmonic interference lithography, which utilizes surface plasmon polaritons (SPPs) excited at the interface between metal and dielectric layers [39,42,43,82]. In this system, evanescent waves couple with SPPs and they are enhanced to expose the photoresist layer with the resolution of the sub-diffraction limit. However, as previously mentioned, in a general system evanescent waves decay very quickly and a special environment is required to couple light with SPPs. First, in order to derive the conditions in which evanescent waves can exist, let us consider light propagating from a medium with the permittivity of ε_1 to ε_2 with the incident angle of θ_1 as Figure 3-1 shows.

$$k_{//}^2 + k_{1z}^2 = k^2\varepsilon_1 \tag{3.1.1}$$

$$k_{//}^2 + k_{2z}^2 = k^2\varepsilon_2 \tag{3.1.2}$$

where $k = \omega/c$. From these two equations,

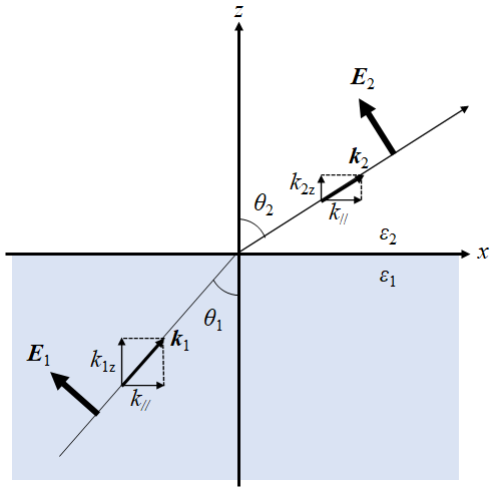

Figure 3-1 A schematic where light is propagating from a medium to another.

$$k_{//}^2 = \frac{k^2(\varepsilon_1 + \varepsilon_2) - (k_{1z}^2 + k_{2z}^2)}{2} \tag{3.1.3}$$

$$k_{1z}^2 - k_{2z}^2 = k^2(\varepsilon_1 - \varepsilon_2) \tag{3.1.4}$$

In each medium, since div$\boldsymbol{D}$ = 0,

$$k_{//}E_{1x} + k_{1z}E_{1z} = 0 \tag{3.1.5}$$

$$k_{//}E_{2x} + k_{2z}E_{2z} = 0 \tag{3.1.6}$$

By the boundary conditions for $\boldsymbol{E}$ and $\boldsymbol{D}$,

$$\varepsilon_2 k_{1z} = \varepsilon_1 k_{2z} \tag{3.1.7}$$

Therefore,

$$k_{1z}^2 = \frac{k^2\varepsilon_1^2}{(\varepsilon_1 + \varepsilon_2)} \tag{3.1.8}$$

$$k_{2z}^2 = \frac{k^2 \varepsilon_2^2}{(\varepsilon_1 + \varepsilon_2)} \tag{3.1.9}$$

and from (3.1.3), (3.1.8), and (3.1.9),

$$k_{//}^2 = \frac{k^2 (\varepsilon_1 \varepsilon_2)}{\varepsilon_1 + \varepsilon_2} \tag{3.1.10}$$

For the surface mode to exist, the conditions where k_{1z} and k_{2z} are imaginary numbers and $k_{//}$ is a real number at the interface need to be satisfied. Therefore, $\varepsilon_1 \varepsilon_2 < 0$ and $\varepsilon_1 + \varepsilon_2 < 0$ can be obtained. Next, using those equations, let us derive the dispersion relation of SPPs. Given that the medium 1 is a metal and its permittivity is expressed by a complex number as $\varepsilon_1 = \varepsilon_1' + i\varepsilon_1''$, and the medium 2 is a loss less dielectric and its permittivity is a real number, the wave number is also $k_{//} = k_{//}' + ik_{//}''$ and substituting them in (3.1.10).

$$k_{//}' \approx k \sqrt{\frac{\varepsilon_1' \varepsilon_2}{\varepsilon_1' + \varepsilon_2}} \tag{3.1.11}$$

$$k_{//}'' \approx \frac{k \sqrt{\varepsilon_1'' \varepsilon_2}}{2 \sqrt{\varepsilon_1'} \sqrt{\varepsilon_1' + \varepsilon_2}} \tag{3.1.12}$$

From (3.2.11),

$$\lambda_{\mathrm{SPP}} = \frac{2\pi}{k_{//}'} = \lambda \sqrt{\frac{\varepsilon_1' + \varepsilon_2}{\varepsilon_1' \varepsilon_2}} \tag{3.1.13}$$

Provided that the free electron model is applied for the medium 1, $\varepsilon_1' = 1 - \omega_{\mathrm{p}}^2 / \omega^2$, and the medium 2 is vacuum, $\varepsilon_2 = 1$,

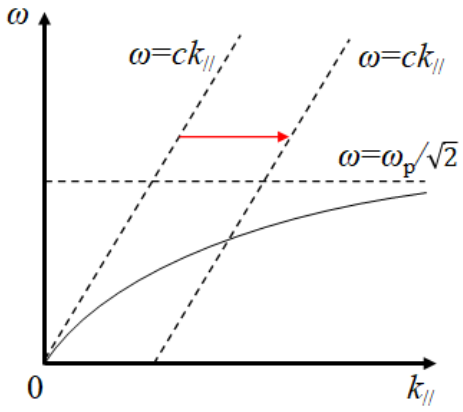

Figure 3-2 Dispersion relations of light and SPPs. The red arrow indicates overcoming the momentum mismatch when periodic metal gratings are employed.

$$k_{//}^2 = k^2 \frac{\varepsilon_1' \varepsilon_2}{\varepsilon_1' + \varepsilon_2} = \left(\frac{\omega}{c}\right)^2 \frac{1 - \frac{\omega_p^2}{\omega^2}}{2 - \frac{\omega_p^2}{\omega^2}} \tag{3.1.14}$$

Here, ω_p is the plasma frequency $\omega_p^2 = \frac{e^2 n}{\varepsilon_0 m_e}$

Since ω approaches asymptotically to $k_{//}c$ for $k_{//} \to 0$ and $\omega_p/\sqrt{2}$ for $k_{//} \to \infty$, the dispersion relation of SPPs can be drawn as Figure 3-2 shows. The dispersion relations of light and SPPs do not cross, which means SPPs cannot be excited by light in a vacuum. One of the methods to couple light with SPPs is to use periodic metal gratings made on a dielectric layer [38]. Then, the momentum mismatch can be overcome as indicated by the red arrow in Figure 3-2 and SPPs are excited at the interface.

This technique has been used to produce the sub-diffraction limit patterns using metal gratings, a regular UV light source, and a photoresist. Although the experimental results in

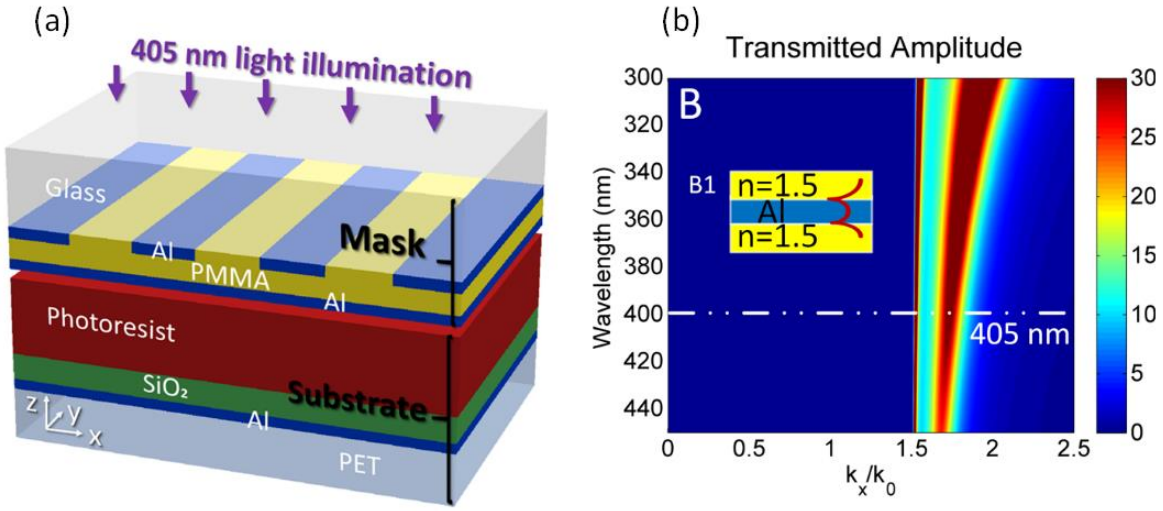

Figure 3-3 (a) The plasmonic lithography for resolving high aspect ratios patterns, and (b) the narrow transmission band of the electric field by the thin Al layer, adapted from literature [39]. Copyright (2016) ACS.

previous studies have successfully shown sub-diffraction limit resolutions, the patterns created in the photoresist layers were very shallow because evanescent waves decay easily [33,81,84,85]. Such shallow patterns are usually not useful for practical application, since dry etching or metal depositions followed by lift-off are performed through the patterns, and they typically require high aspect ratio structures. X. Chen *et al.*, have reported improved technology that can resolve patterns with high aspect ratios while the feature size of the patterns were still below the diffraction limit of the light [39]. In the study, a thin Al layer was used beneath the Al gratings planarized by a PMMA layer to obtain the narrow transmission band of the electric field, as shown in Figure 3-3. Thin layers of SiO_2 and Al were also coated on the substrate, and it sandwiches a photoresist layer with the photomask to create a Fabry-Pérot cavity. As a result, the light intensity in the photoresist layer can have

a high contrast along the horizontal direction and high uniformity along the vertical direction, with the resolved patterns having much higher aspect ratios than the previous work.

3.2 Plasmonic interference lithography utilizing ENZ HMMs

Early studies have employed comparably simple structures composed of metal gratings and a pair of dielectric and metal layers. In this scheme, the two evanescent waves propagating to the opposite directions horizontally create a standing wave with the half of the original wavelength. Therefore, the resolving patterns have a half period of the metal gratings, e.g., 122.5 nm periodic gratings were fabricated using 245 nm periodic metal gratings [39]. As described in the previous section, some metals with certain thicknesses can pass the narrow frequency band and filter other waves, which means the photomask that is able to utilize the higher order of diffractions can be engineered. One example of these experiments was implemented using hyperbolic metamaterials (HMMs) [42,86–88].

HMMs are described by an effective permittivity in a tensor form:

$$\bar{\bar{\varepsilon}} = \begin{pmatrix} \varepsilon_{\parallel} & 0 & 0 \\ 0 & \varepsilon_{\parallel} & 0 \\ 0 & 0 & \varepsilon_{\perp} \end{pmatrix} \tag{3.2.1}$$

with one of the principal components being the opposite sign of the other two, that is, $\varepsilon_{\parallel} \cdot \varepsilon_{\perp} < 0$, where $\varepsilon_{\parallel}$ and $\varepsilon_{\perp}$ are permittivities parallel and perpendicular to the anisotropy axis, respectively, and they are complex numbers. Isofrequency surfaces of transverse magnetic waves for such systems become Figure 3-4 and are given by the following equation

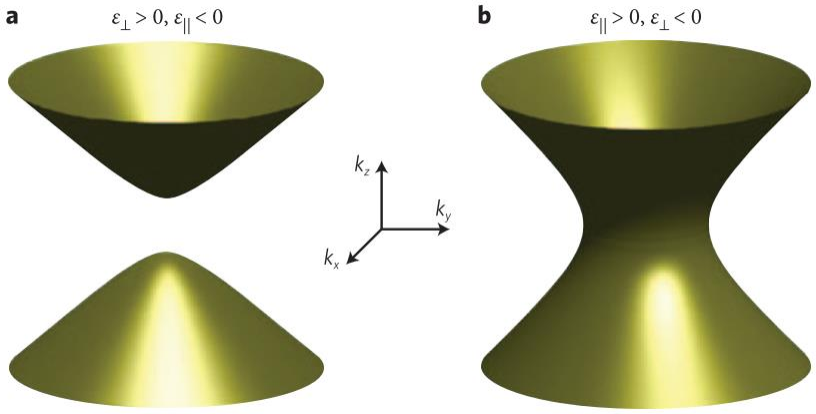

Figure 3-4 Isofrequency surfaces for transverse magnetic wave in HMMs given by (a) $\varepsilon_\perp > 0$, $\varepsilon_\parallel < 0$ and (b) $\varepsilon_\parallel > 0$, $\varepsilon_\perp < 0$, adapted from literature [86]. Copyright (2013) Nature.

$$\frac{k_x^2 + k_y^2}{\varepsilon_\parallel} + \frac{k_z^2}{\varepsilon_\perp} = \frac{\omega^2}{c^2} \tag{3.2.2}$$

where k_x, k_y, and k_z are x, y, and z components of the wave vector, respectively [86]. Another example of HMMs is alternating thin film stacks of metal and dielectric layers. When the film thicknesses of metal and dielectric layers are thinner than the wavelength of light, the permittivities of the system follow by the effective medium approximation, which is expressed as

$$f = \frac{t_\mathrm{m}}{t_\mathrm{m} + t_\mathrm{d}} \tag{3.2.3}$$

$$\varepsilon_\parallel = f\varepsilon_\mathrm{m} + (1 - f)\varepsilon_\mathrm{d} \tag{3.2.4}$$

$$\varepsilon_\perp = \frac{\varepsilon_\mathrm{m}\varepsilon_\mathrm{d}}{(1 - f)\varepsilon_\mathrm{m} + \varepsilon_\mathrm{d}} \tag{3.2.5}$$

where t_m and t_d are the thicknesses, and ε_m and ε_d are the permittivities of metal and dielectric, respectively. Therefore, effective permittivity can be engineered by choosing the metal and

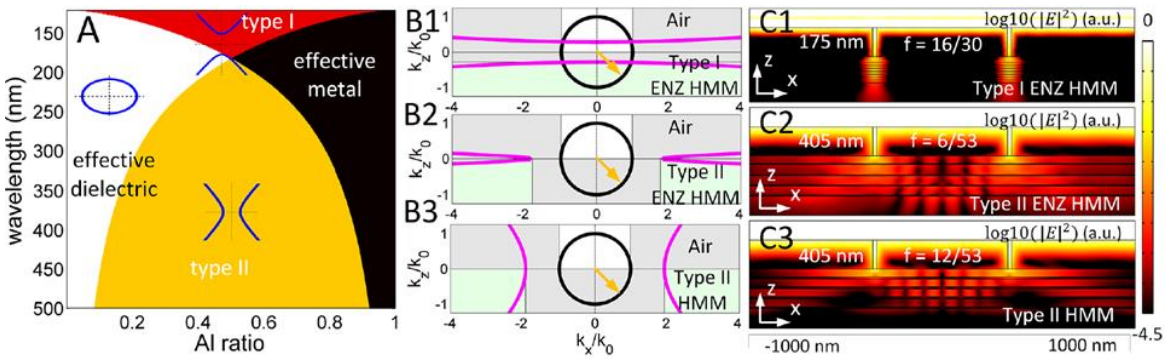

Figure 3-5 (A) Characteristics of HMMs composed of Al and Al_2O_3 for the various wavelength with the different Al ratios. (B) Isofrequency curves of air and HMMs and (C) the electric field intensity distributions for each HMMs, adapted from literature [42]. Copyright (2017) ACS.

dielectric materials and their thicknesses. In particular, HMMs whose tangential component is close to zero are called epsilon-near-zero HMMs (ENZ HMMs) [89]. X. Chen *et al*., have reported the computational results of how evanescent waves behave in three different HMMs: type I ENZ HMMs ($\varepsilon_{\parallel} \to 0$, $\varepsilon_{\perp} < 0$), type II ENZ HMMs ($\varepsilon_{\parallel} \to 0$, $\varepsilon > 0$), and type I HMMs ($\varepsilon_{\parallel} > 0$, $\varepsilon_{\perp} < 0$) as Figure 3-5 shows [42]. The intensities of the electric fields in those HMMs show very different phenomena. Type I ENZ HMMs confine the light while maintaining the high intensity, and type II ENZ HMMs result in the divergence of the diffracted light with high intensity. Type II HMMs also show similar intensity distribution with type II ENZ HMMs, but the light intensity decays vertically. For plasmonic lithography applications, type II ENZ HMMs are suitable to create the uniform light intensity distribution in the photoresist layer, as well as filtering a certain order of the diffraction light to obtain the reduced periodicity.

X. Chen *et* al., have performed experimental work using the photomask shown in

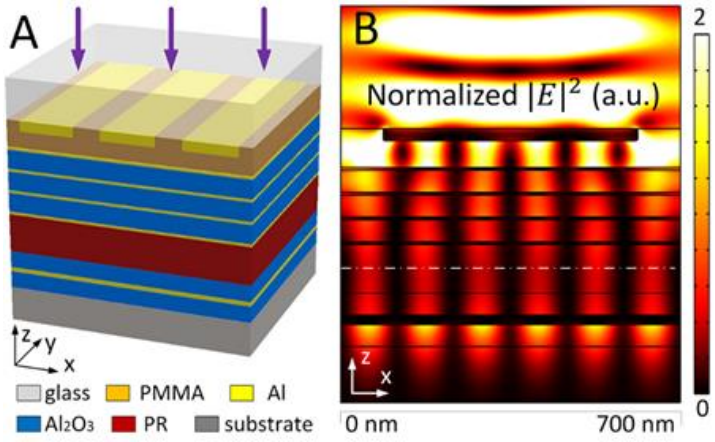

Figure 3-6 (A) A photomask and substrate design for plasmonic lithography utilizing ENZ HMMs and (B) the intensity distribution of the electric field in them, adapted from literature [42]. Copyright (2017) ACS.

Figure 3-6 which consists of 7 alternating Al/Al_2O_3 layers with a thicknesses of 6 nm and 47 nm, respectively [42]. The substrate coated with the photoresist also has 3 layers of Al_2O_3/Al/Al_2O_3 with a thicknesses of 47 nm/ 20 nm/ 47 nm. As a result, 117 nm periodic gratings were fabricated in the photoresist layer using the Al gratings with 700 nm periodicity, which corresponds to 1/6 of the original period. This technology offers a promising solution to create very fine patterns due to its ability to reduce the scale of the period in the photomask level.

So far, most studies have focused on the fabrication of sub-diffraction limit patterns using SPPs. However, we have also performed experimental work focusing on better productivity using a photo roller system with a flexible photomask [43]. In this setup, the photomask is wrapped on a quartz cylinder where the UV light can shine from the inside to realize a continuous patterning on a substrate as shown in Figure 3-7. In our previous study,

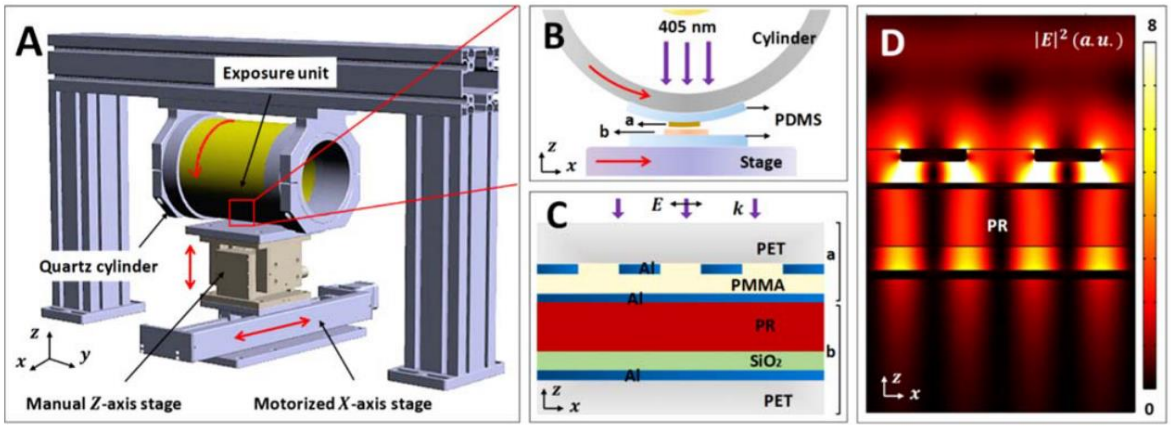

Figure 3-7 (A) A schematic of plasmonic roller lithography setup and (B) and its detailed picture of how the photomask and substrate are in contact. (C) A photomask design used in the experiment and (D) its simulated light intensity distribution, adapted from literature [43]. Copyright (2019) IOP Science.

plasmonic lithography by Al gratings with a pair of metal and dielectric layers was performed to obtain 122.5 nm periodic structures from 245 nm periodicity in a continuous manner.

There have been many studies on the plasmonic interference lithography as introduced above, but most of them are capable of patterning in a comparably small area e.g., 1 mm × 10 mm. The most challenging drawback is that the photomask design requires very fine patterning by electron beam lithography. For example, even in the plasmonic interference lithography utilizing ENZ HMMs in the previous study with larger metal gratings, the Al gratings for the photomask were 700 nm period with the duty cycle of 0.75 [42]. These structures are still difficult to fabricate, and thus electron beam lithography was used for the photomask fabrication resulting in a small size. In order to achieve the ability to pattern in a large area in a continuous manner, we propose further scaling by enlarging the period of the Al gratings to a size that can be fabricated by photolithography while keeping

the resolution smaller than the diffraction limit by utilizing higher order diffractions as well as employing the photo roller system. The most challenging part of this process is the photomask fabrication, since it needs to be made on a flexible transparent film, which typically limits the material choice to polymer films.

3.3 Photomask design

First, the photomask design was simulated by COMSOL Multiphysics. The design is based on the previous study [42,43]. The photomask consists of Al gratings, spacer, and metal/dielectric layer stacks, which are made on a PET film. A substrate coated with a photoresist is prepared separately to create a Fabry-Pérot when the photomask and substrate are in contact. It is necessary to obtain high contrast along the horizontal direction and high uniformity along the vertical direction, confining the evanescent wave in the photoresist layer. Schematics of the photomask and substrate, as well as the simulated result of normalized $|E|^2$ in them are shown in Figure 3-8. The starting substrate is a PET film, and it is planarized by 500 nm thick SU-8 followed by 20 nm SiO_2. The Al gratings of the photomask has a

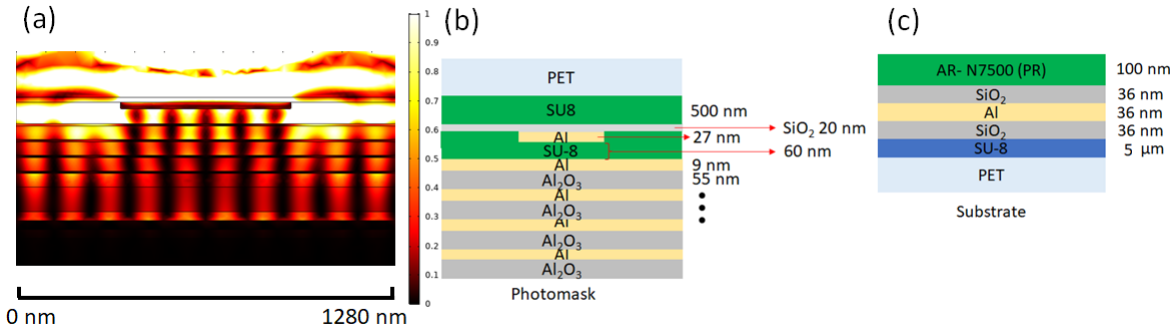

Figure 3-8 (a) The simulated $|E|^2$ in the photomask and substrate. Schematics of (b) the photomask and (c) substrate.

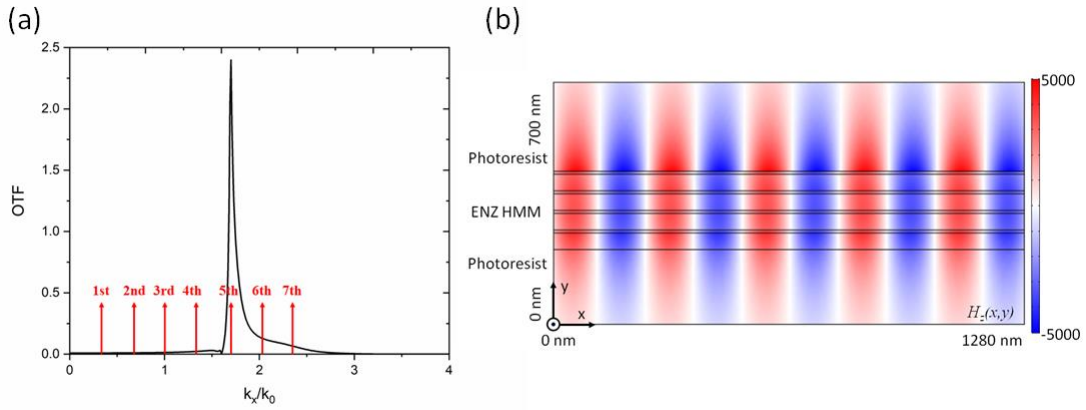

Figure 3-9 (a) The OTF of the photomask passing the 5th order diffractions while filtering the other orders. The red arrows indicate the order of each diffraction. (b) The magnetic field H_z(x,y) distribution in the ENZ HMM for the 5th order diffraction wave.

period of 1280 nm with a duty cycle of 0.45 and a thickness of 27 nm. 60 nm SU-8 is coated on them as a spacer, and 8 alternating layers of Al/Al_2O_3 with thicknesses of 9 nm and 55 nm respectively deposited on it. The photoresist coated substrate is also fabricated on a PET film with 5 μm SU-8 planarization. SiO_2/Al/SiO_2 layers with thicknesses of 36 nm each are deposited on it, and HMDS is coated on the top SiO_2 layer. Here, the interference of the 5th order diffractions of the gratings creates 10 stripes in a single period, which can expose a photoresist with a 1/10 feature size of the Al gratings. Figure 3-9 (a) shows the optical transfer function (OTF) which is defined by

$$\mathrm{OTF} = \frac{|H_\mathrm{t}|^2}{|H_\mathrm{i}|^2} \tag{3.3.1}$$

where H_t and H_i are the transmitted and incident magnetic field, respectively. The only 5th order diffraction can transmit the ENZ HMM in the photomask while the other orders are blocked. The transmitted 5th order diffraction waves propagate in the photoresist layer in

positive and negative directions, respectively. As a result, they create the standing wave with a half wavelength, i.e., the 1/10 period of the Al gratings as Figure 3-9 (b) shows.

3.4 Photomask fabrication

As previously mentioned, the most challenging part of this work concerns the creation of a photomask on a flexible transparent substrate (seen here in the form of a PET film) which enables photo roller lithography. Because of its wide material compatibility and capability of patterning in a large area, we employed metal transfer assisted nanolithography using KMPR, which is described in section 2.3.4 to make Al gratings on a PET film in a large area. A PET film was cut into 2.5″×2.5″ and cleaned in Acetone and IPA with sonication for 5 minutes each. Then, it was fixed on a Si wafer by Kapton tapes and 500 nm SU-8 was spun on it. After a 20 nm SiO_2 layer was deposited by electron beam evaporation, 27 nm thick Al gratings with a period of 1.28 μm and duty cycle of 0.45 were fabricated in a 2″×2″ area using the same procedure described in section 2.3.4.1. The Al gratings were planarized with SU8 by spincoat aiming 60 nm thick on top of the Al gratings, and the SU-8 layer was fully cured and post-exposure baked. Then the alternating 8 layers of Al/Al_2O_3 with thicknesses of 9 nm/ 55 nm were evaporated at the deposition rates of 2 Å/s and 5 Å/s, respectively. 5 min intervals for cooling were taken after each deposition. Figure 3-10 shows the cross section of the 8-layer stacks made on a Si wafer for the reference. For the photoresist coated substrate, the starting substrate is either a PET film, Si wafer, or glass substrate. The substrate was cleaned by Acetone and IPA with sonication for 5 min respectively, and then a 5 μm SU-8 layer was spun to planarize the surface. After fully curing the SU-8 and the post exposure bake,

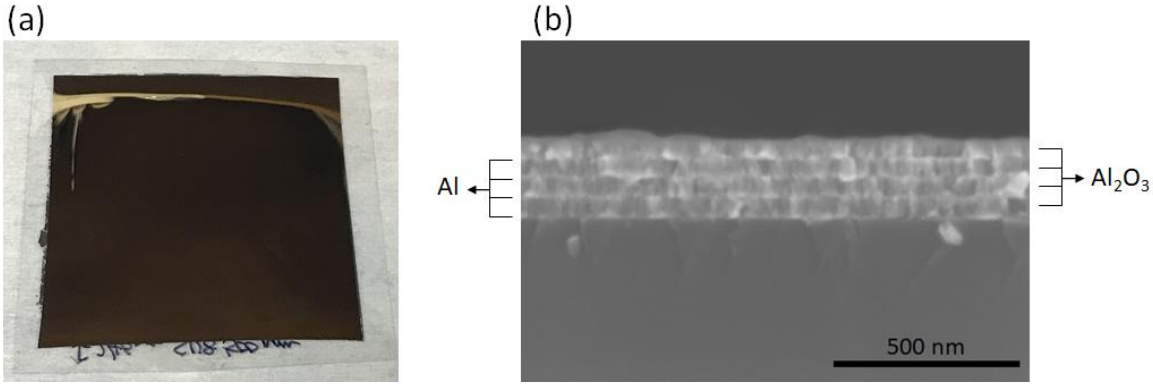

Figure 3-10 (a) The fabricated photomask and (b) a cross-sectional SEM image of the 8 layer stacks of Al/Al_2O_3 with the thicknesses of 9 nm/55 nm.

$SiO_2/Al/SiO_2$ layers with thicknesses of 36 nm/36 nm/36 nm were deposited by electron beam evaporation. For a Si or glass substrate, Al/SiO_2 layers with thicknesses of 36 nm/36 nm were deposited after the same cleaning process. HMDS was coated on the substrates by vapor prime in an oven (YES-310TA (E) : Yield Engineering System) and then TSMR-V90 (TOK America) was spun on it with a thickness of 100 nm.

3.5 Photo roller lithography and optical setup

In previous work, the photomask size was small enough for a beam waist of a regular laser. However, since the new photomask is rather large (2″×2″), the laser needs to be expanded to expose the 2″ width uniformly. The laser employed for this experiment is a 442 nm diode laser with the maximum intensity of about 5 W, and its beam waist is about 1 mm in diameter and Gaussian profile. In order to design the optical setup to obtain a line beam with homogeneous intensity in 2″ width, the ray trace simulation was carried out by Zemax OpticStudio as shown in Figure 3-11. The laser first passes a polarizer to obtain TM

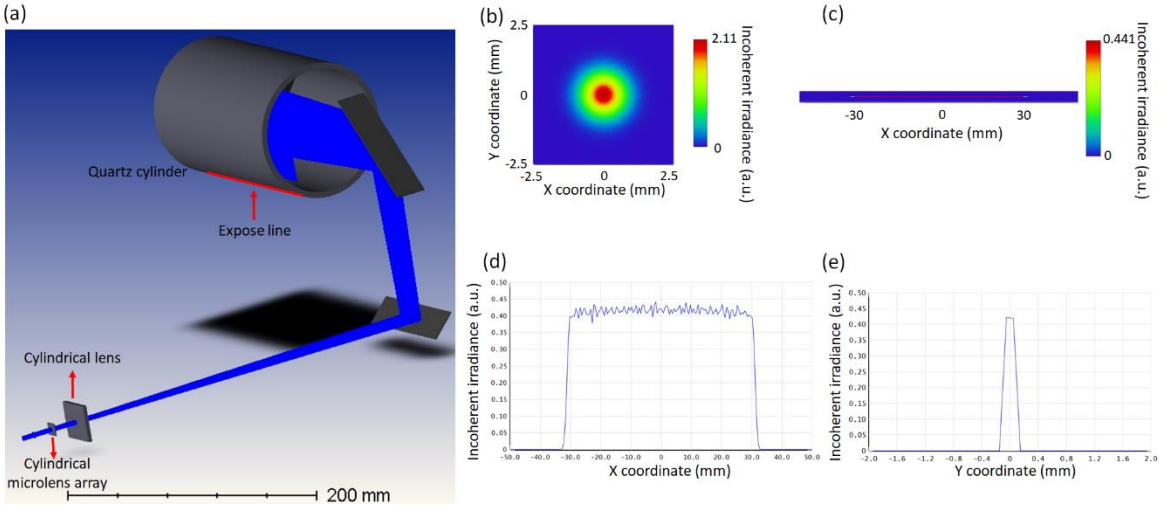

Figure 3-11 (a) The simulated optical setup by Zemax OpticStudio to obtain a homogenized line beam in 2″ width. (b) Gaussian profile of the original laser beam and (c) the homogenized beam intensity at the exposed line. The intensity profiles of the homogenized line beam along (d) the x-direction and (e) the y-direction.

polarization and then cylindrical microlens arrays with a divergence angle of 2.2˚. This homogenizes the beam intensity distribution and expands the laser horizontally. The next cylindrical lens with a long focal length gradually focuses the laser vertically. After thereflections by the three rectangular mirrors, the laser is incident on the photomask from the inside of the quartz cylinder with homogeneous intensity in a 2″ width. A schematic of the photo roller setup and its picture are shown in Figure 3-12. The stage where the photoresist coated substrate is placed is motorized and movable at an arbitrary speed. The quartz cylinder can rotate by the friction force when the motorized stage moves. Figure 3-12 (c) is a photo of the original laser beam and (d) is the homogenized line beam formed by the optical setup.

3.6 Experimental results and discussions

3.6.1 Experimental results

The SEM images shown in Figure 3-13 are the experimental result fabricated in the photoresist on the glass substrate. A point laser beam without the line beam formation was used, and the exposure was 60 seconds with the laser power of 0.322 A, which is ~40 mW.

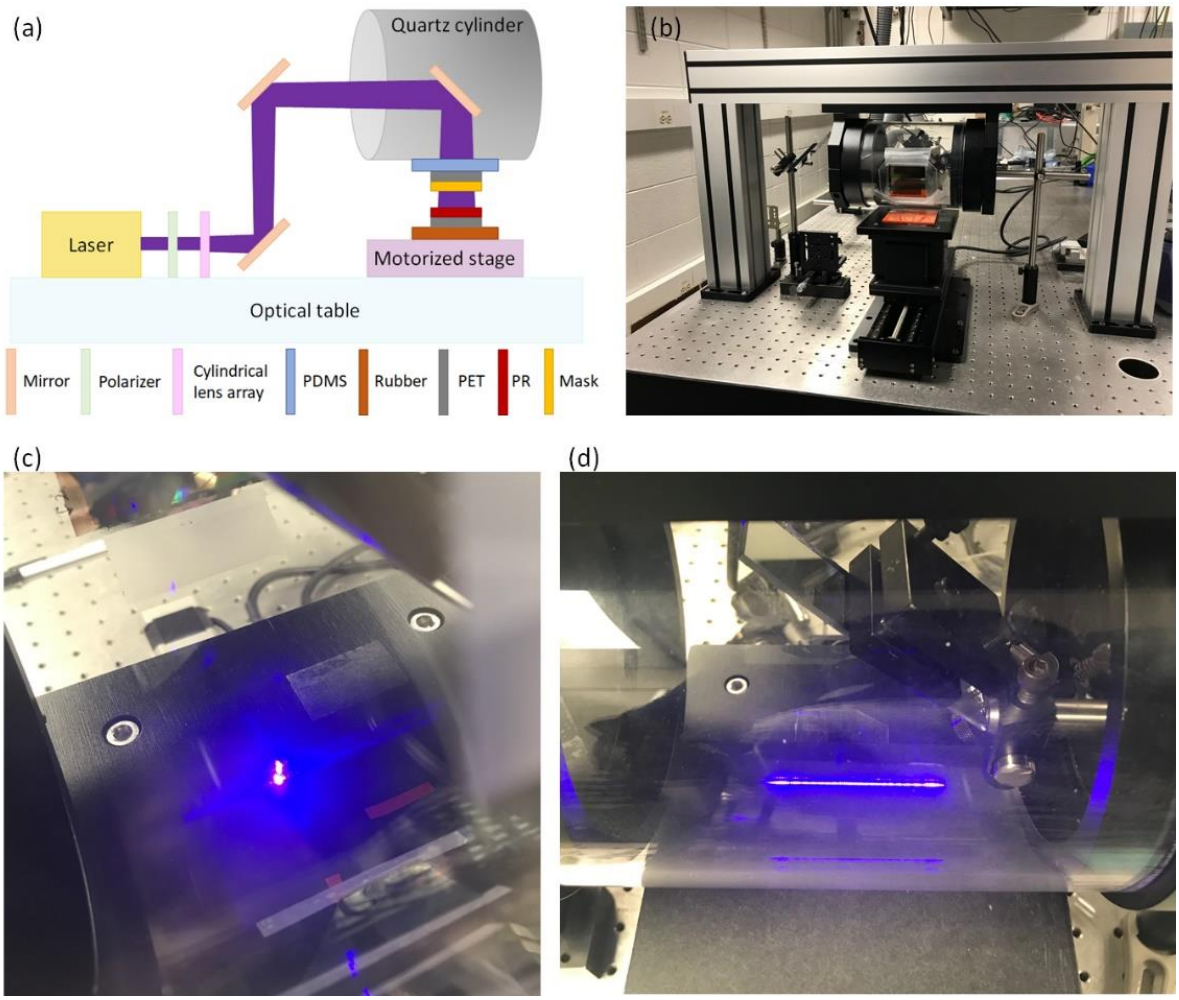

Figure 3-12 (a) A schematic of the optical setup and (b) its picture. (c) A original beam shape and (d) line beam formed by the lenses.

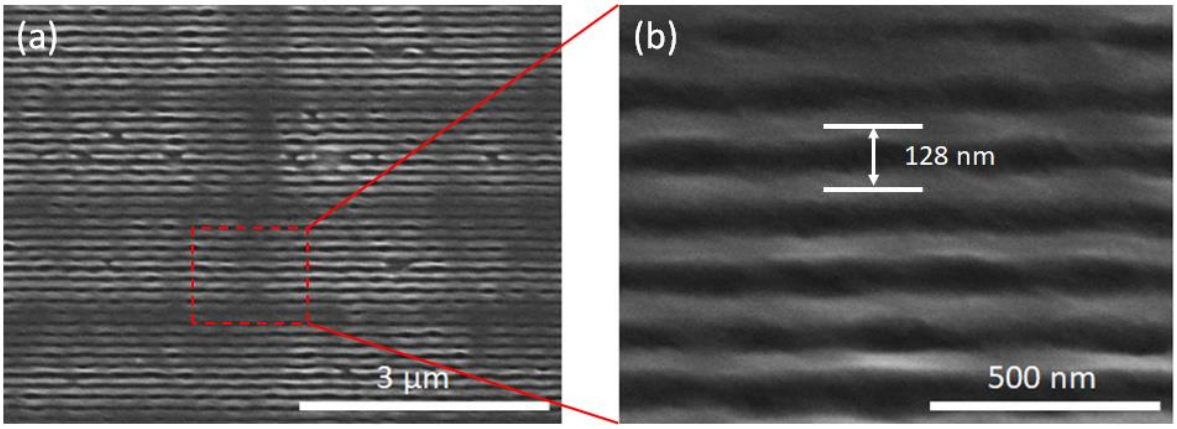

Figure 3-13 (a) The resolved pattern by plasmonic lithography and (b) its close image showing a period of 128 nm gratings created in the photoresist layer.

The gratings with a 128 nm period were successfully fabricated using the ENZ HMM photomask. However, this system is highly sensitive to the pressure applied between the photomask and substrate to make a conformal contact. Figure 3-14 shows three exposure results with different pressures, wherein lower pressure produced a better result than higher pressure. The reasons behind this pressure sensitivity and the characterizations of the photomask will be discussed in the next section.

3.6.2 Characterization of the ENZ HMM photomask

First, AFM was performed on the photomask to characterize it. As Figure 3-15 shows, a few nm fluctuations were observed on the surface whose period corresponds to the period of the Al gratings. This is most likely because the planarization by SU-8 was not perfect enough to obtain the flat surface. For further understanding, AFM measurements were also performed on the Al gratings after being fabricated on a PET film by metal transfer assisted nanolithography. Figure 3-16 shows the measurements on the same area of the photomask

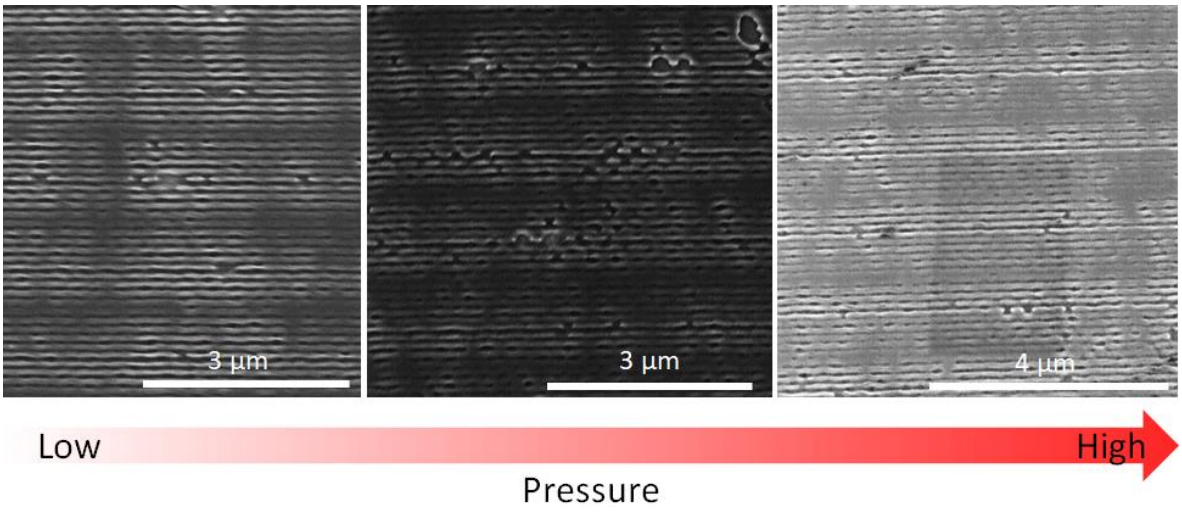

Figure 3-14 SEM images of three exposure results with different applied pressures from low to high.

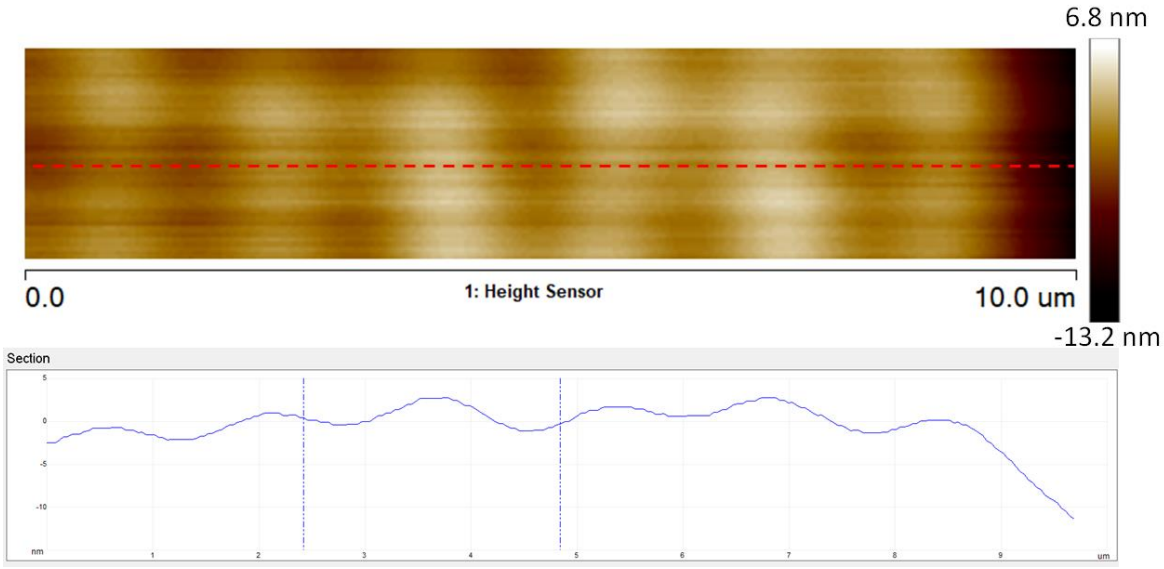

Figure 3-15 An AFM image on the photomask.

with different amplitude setpoints. The difference of the amplitude setpoints is only 3 mV, but the measurements show different results. To interpret these results, the principle of AFM will be discussed first. AFM can characterize the mechanical properties as well as the surface roughness of the sample. In the tapping mode, an AFM tip oscillates as seen in Figure 3-17 and sweeps the surface of the sample. The strength of the tapping is related to the amplitude setpoint, that is, a higher amplitude setpoint means the AFM tip taps the surface more strongly. Therefore, one can tell the hardness of the sample from the measurement data with different amplitude setpoints. By comparing the two measurements shown in Figure 3-16, it can be seen that the hardness at two points on the Al gratings and spacings are different. Thus, when the photomask is pressurized, the two regions are compressed differently, which results in the deformation of the photomask. To gain further insight, the Mises stress distribution in the photomask and substrate when it is pressurized was simulated by COMSOL Multiphysics as shown in Figure 3-18. Because the photomask consists of different materials: a metal, metal oxides, and polymers, it does not deform uniformly along the vertical direction. Moreover, the substrate is a 127 μm thick PET film, and it can also be deformed when pressurized. Therefore, the experimental results showing this sensitivity to applied pressure can be interpreted as the deformation of the photomask arising from the material compositions of the photomask.

3.6.3 Computational analysis on the effects caused by the roughness and deformation

In previous studies, the surface fluctuations caused by the periodic metal gratings have not been taken into account in plasmonic lithography. In this section, the effects of them

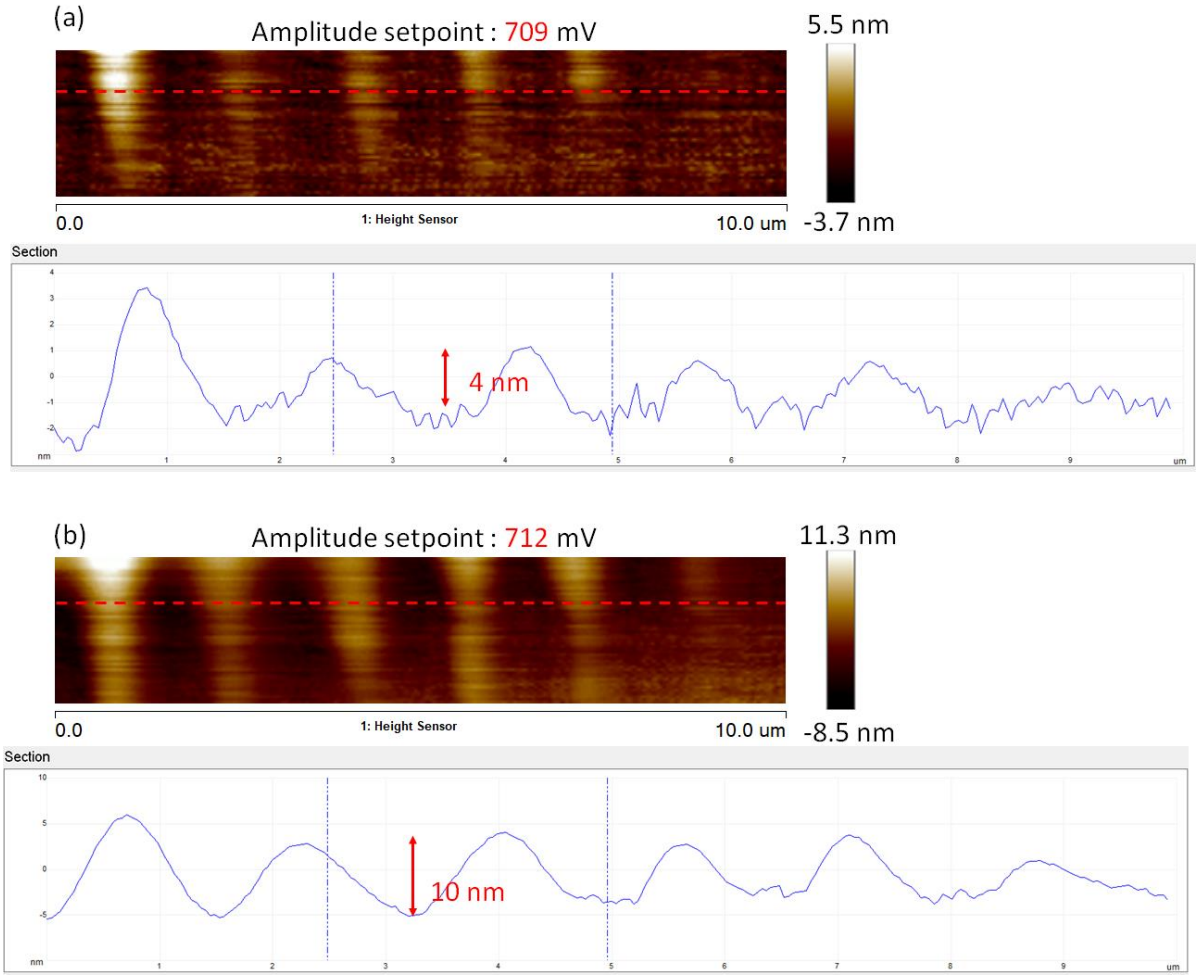

Figure 3-16 AFM measurements on the Al gratings made on a PET film with an amplitude setpoint of (a) 709 mV and (b) 712 mV.

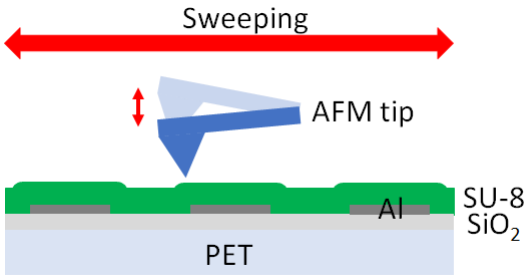

Figure 3-17 A schematic of AFM.

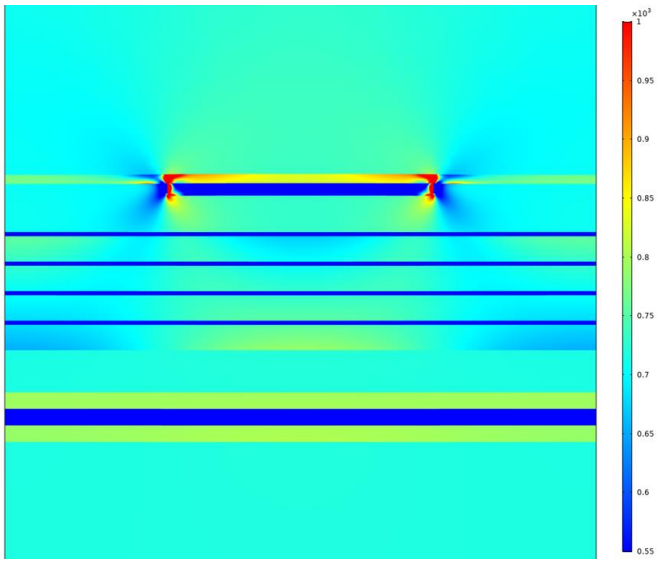

Figure 3-18 The simulated Mises stress distribution in the photomask and substrate when pressurized.

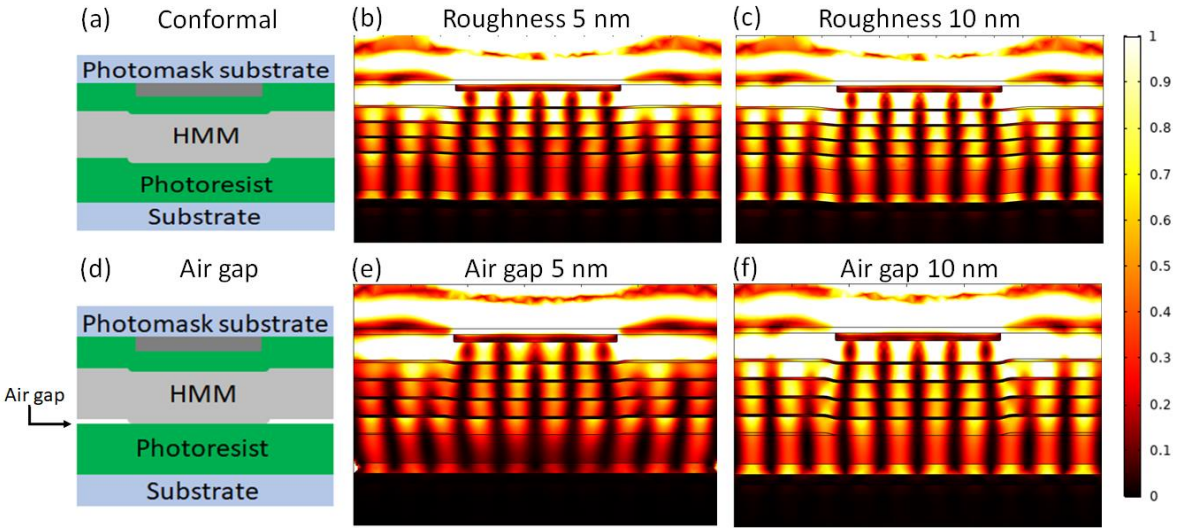

Figure 3-19 (a) Schematics of the situations when the photomask and substrate are in conformal contact and (d) when there are air gaps between them. Simulation results when the roughness of the photomask is (b) 5 nm and (c) 10nm, and when the air gaps are (e) 5 nm and (f) 10 nm. All simulation results are under the conditions where the Al gratings are 27 nm and 1.28 μm period with the duty cycle of 0.45, the SU-8 spacer is 60 nm thick, the ENZ HMM is 8 alternating layers of Al/Al_2O_3 = 9 nm/55 nm, the photoresist thickness is 100 nm, and the substrate has SiO2/Al/SiO2 = 36 nm/ 36 nm/ 36 nm layers.

will be discussed based on the simulated results by COMSOL Multiphysics. Figure 3-19 shows the simulated results with different roughness: no roughness, 5 nm, and 10 nm, for two different situations where the photomask and substrate are in conformal contact or there are air gaps between them. Even though the roughness is up to 10 nm, it changes the light intensity distributions in the photoresist layer significantly, and the contact of the photomask and substrate plays a very important role. In the cases of Figure 3-19 (a), the simulated results with roughnesses of 5 nm and 10 nm show even higher light intensity in the photoresist layer, although a slight deformation along the vertical direction is observed. However, in the latter situation, despite the fact that 10 nm air gaps do not affect the contrast of the light intensity in the photoresist layer along the horizontal direction, in the case of 5 nm air gaps the light intensity distribution deforms in the photoresist layer and shows poorer contrast along the horizontal direction. These results show that when the photomask and substrate are in strong contact, since the photoresist layer is deformed to make a conformal contact, the roughness on the photomask will not affect the pattern fidelity of the photoresist. However, when they are in weak contact, there will be air gaps that might spoil the plasmonic lithography depending on the thickness of the air gaps.

3.6.4 Importance of other parameters: incident angle of light, refractive index of materials, and material choice for substrate

There are several works investigating the effects caused by the parameters of the photomask design such as the period of the metal gratings, duty cycle of the gratings, and thicknesses of each layer [40,42]. However, there are several more parameters that need to

be considered. First, the refractive index of the dielectric layer, Al_2O_3 here, is discussed. Usually, thin layers of metal and dielectric are deposited by thermal/electron beam evaporations because of its ease and accuracy in thickness control. While metals show high reproducibility in terms of the refractive index of the deposited film, the refractive indices of metal oxides are sometimes changed in the range of ~0.1. This is mainly because the crystal structures are different from bulk and the composition of the material source changes through many evaporations. In the case of Al_2O_3, the evaporated thin film may form amorphous crystals, and the ratio of Al and Oxygen in the source may change from 2:3. According to the reference [90], the refractive index of Al_2O_3 for 442 nm, is about 1.69, but the actual values were confirmed to be as low as 1.58 to 1.65 for the electron beam evaporated thin films in this study. Figure 3-20 shows four different simulated results for the refractive indices of Al_2O_3 from 1.57 to 1.69, which may occur in physical fabrications. Although the 10 stripes are resolved in the photoresist layer in all the cases, their contrast and uniformity vary substantially. In particular, for n = 1.57 and 1.69, it is hard to obtain well-resolved patterns in the photoresist layer due to poor contrasts along the horizontal direction. These situations can be improved by adjusting other relevant parameters. For example, in the case that the refractive index of Al_2O_3 is 1.57, changing the 4 metal layers thickness to 11 nm while the other parameters remain the same can solve this problem, as Figure 3-21 (a) shows. Similarly, when the refractive index is 1.69, changing the thickness of SU-8 spacer to 30 nm, 4 Al layers thickness to 7 nm, and 4 Al_2O_3 layers thickness to 45 nm creates a better result as seen in Figure 3-21 (b). Therefore, it is recommended that the optical property of a thin Al_2O_3 film be measured prior to the photomask fabrication, and the photomask design

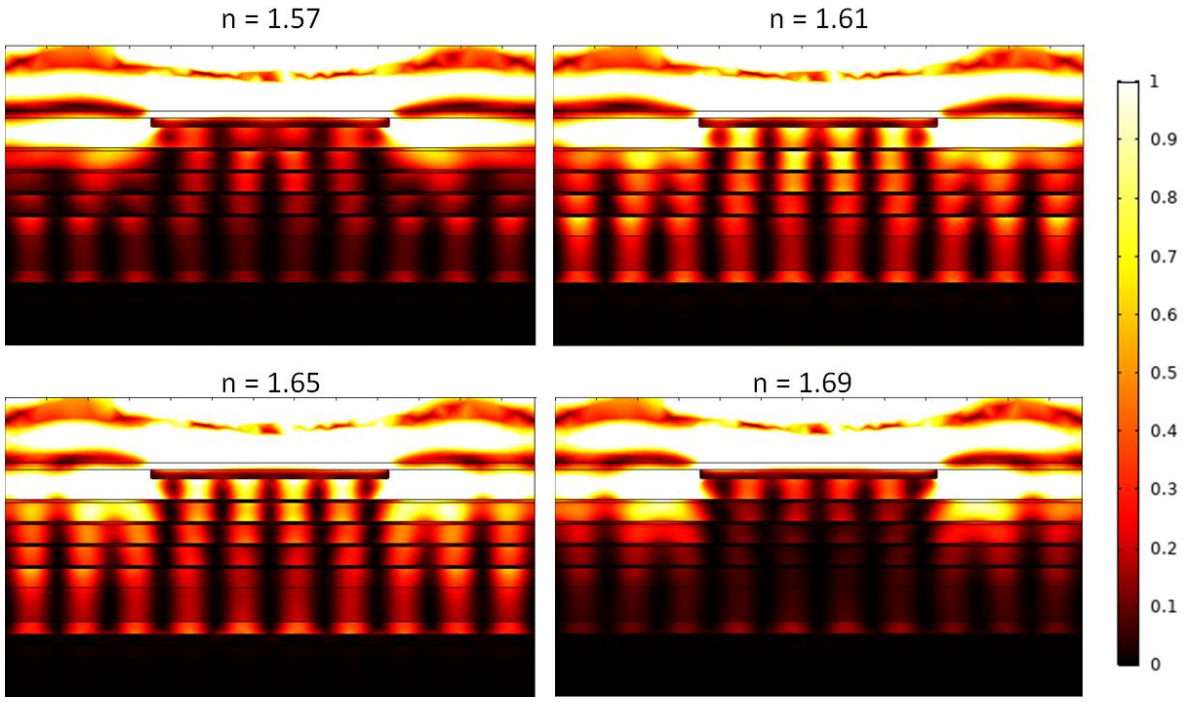

Figure 3-20 Simulation results with the different refractive indices of Al_2O_3 from 1.57 to 1.69 where the other conditions are all same.

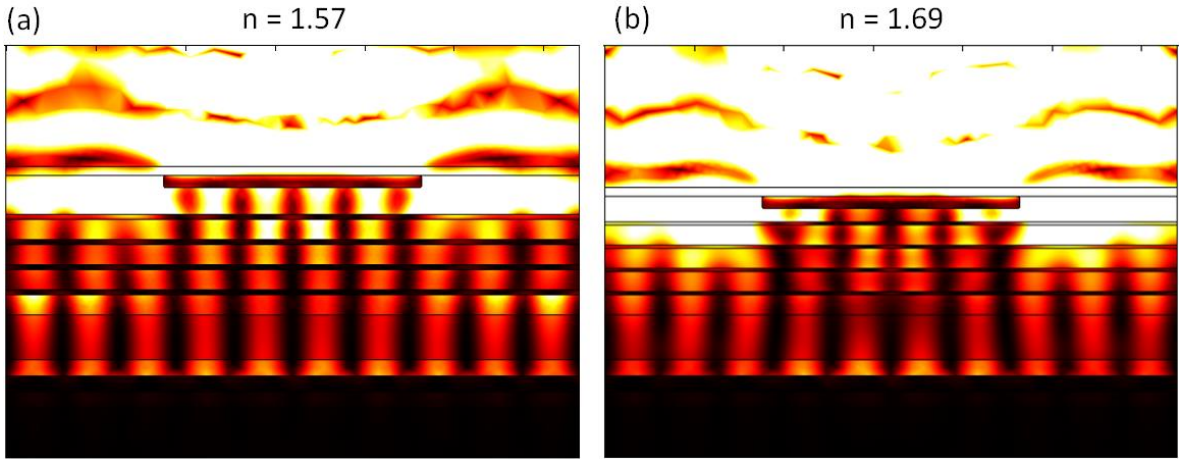

Figure 3-21 Good simulation results (a) with the refractive index of Al_2O_3 1.57 and the thickness of 4 Al layers 11 nm, and (b) the refractive index of Al_2O_3 1.69, SU-8 thickness 30 nm, 4 Al layers 7 nm, and 4 Al_2O_3 layers 45 nm.

finalized accordingly.

Although there is no concern in the case of small area plasmonic lithography using a point laser beam, when the beam expansion for a large area is required, the incident angle of light plays an important role. As described in the former section, cylindrical microlens arrays are used in this work to get a line beam that has a divergence angle of 2.2˚, which means the laser has an incident angle of up to 2.2˚ to the photomask from the center to the edge of the line beam. Figure 3-22 shows simulated results for different incident angles from 0 to 75˚ to the photomask. In cases where the incident angle is small, the light intensity distributions in the photoresist layer do not change much. However, for larger angles e.g., over 15˚, the interferences in the photoresist layer cannot resolve the patterns well. Therefore, cylindrical

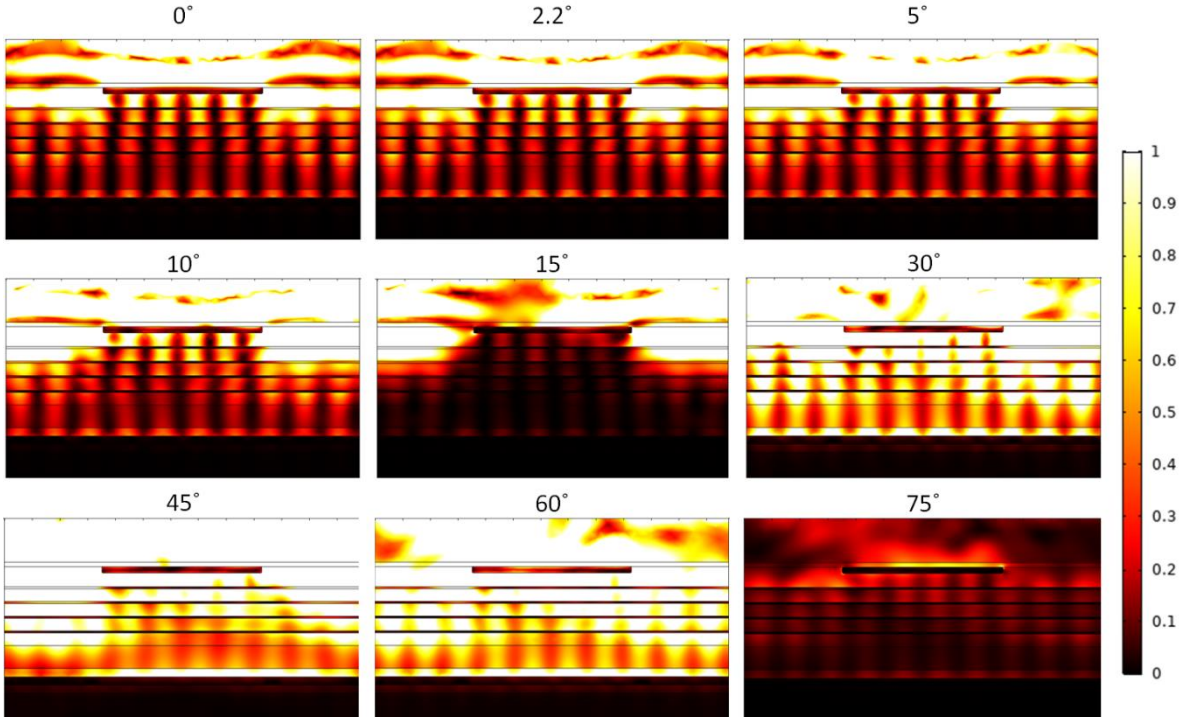

Figure 3-22 Simulated results with different incident angles from 0˚ to 75˚.

microlens arrays with a small divergence angle are suitable for the beam expansion despite that it requires a long distance to the exposure surface from the lens to obtain a long line beam.

Lastly, for the wider applications of this technology, the importance of the material choice for the substate will be evaluated. The photoresist-coated substrate discussed so far has layers of SiO_2/Al/SiO_2 with thicknesses of 36 nm/ 36 nm/ 36 nm. These layers are important to create a Fabry-Pérot cavity for high uniformity in the light intensity distribution along the vertical direction, and it enables the fabrication of high aspect ratio patterns. However, the necessity of the layers also limits the applications. Although this is inevitable for a transparent substrate such as a glass or polymers, it is desirable for reflective substrates, especially Si, to be employed without any additional layers on it. Figure 3-23 shows the simulated results when Si is the substrate, and no additional layers are used. Even in the case that the same photomask (the one which gave the best result on the substrate with

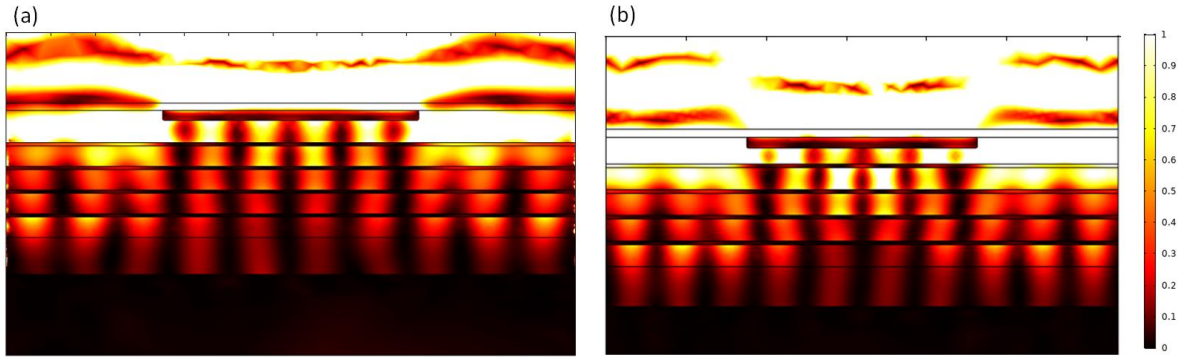

Figure 3-23 Simulation results when Si is used as a substrate. (a) The same photomask with the best result on the SiO_2/Al/SiO_2 = 36 nm/ 36 nm/ 36 nm coated substrate, and (b) the better result with the SU-8 spacer thickness 40 nm.

$SiO_2/Al/SiO_2$ = 36 nm/36 nm/36 nm films) is used with a different substrate, the 10 interference patterns in the photoresist layer can be resolved. Figure 3-23 (b) shows the best result, reducing the SU-8 spacer thickness to 40 nm. If the photomask design is optimized for the Si substrate, the contrast and uniformity of the light intensity distributions in the photoresist layer can be improved. Therefore, plasmonic lithography can be used to fabricate patterns directly on Si substrates using the developed photoresist as an etching or deposition mask.

3.7 Summary

In this chapter, the mechanism of plasmonic lithography and experimental studies to scale up the patternable area size were discussed. While the pressure applied to the photomask needs to be carefully considered due to the complexity of the photomask, plasmonic lithography using ENZ HMMs has been shown to be a very promising technology for fabricating sub diffraction limit patterns from comparably large-scale structures. Several parameters that were not previously studied which could affect the lithography results were also discussed. Although a careful study on the photomask design is required for the photomask fabrication, this technology shows huge potential for industry applications due to its scalability and resolution.

CHAPTER 4

Nano-scale Electro/Electroless Plating for Optics/Photonics Applications

4.1 Introduction to electro/electroless plating

Electroplating and electroless plating technologies have been widely used since the 19th century because of their plainness and broad applications. For conventional applications such as anti-rust coatings, mirrors, and jewelries, the characteristics of plating technologies (e.g., the deposition rate, surface morphology, or thickness control) are not particularly vital for fabrication. As nanotechnologies develop and share a significant role in modern technology, the demand for technology that can deposit various materials with a nanometer scale at a low cost has become increasingly desirable. In the current industry, those fabrications are mostly done by physical vapor deposition or chemical vapor deposition because of their wide material compatibility, excellent thickness controllability, and plainness of the process. However, those technologies require high vacuum for depositions, which increases the fabrication cost significantly as it takes substantial time to pump down the chamber and the vacuum chamber limits the size of substrates.

As low-cost alternative technologies, electroplating and electroless plating have attracted significant attention. Since both technologies are wet chemical processes, high vacuum and pumping time are not required and scaling up is simpler, as they do not use a vacuum chamber. Electroplating is performed with applied voltage to reduce metal ions to pure metals. Hence, the substrate needs to be conductive, and it limited the material in the

early stages of this technology. However, owing to the development of transparent semiconductor materials such as Zinc Oxide (ZnO) and Indium Tin Oxide, as well as the development of electroplating technology for metal oxides, the applications of electroplating have been greatly expanded [49–51]. On the other hand, electroless plating is compatible with both conductive and nonconductive substrates, but catalysts are required on the substrate to reduce metal ions to pure metals. Therefore, the technology used to deposit catalysts on the substrate plays a significant role in electroless plating technology [91].

4.2 Catalytic Palladium colloidal solution for electroless plating

As a catalytic material, Pd is widely used because of its stability in many solutions and its ability to catalyze various metals [92–94]. To utilize the advantage of electroless plating, a wet chemical process for the Pd deposition is desirable. Moreover, the minimum amount of Pd that can produce uniform coating on the substrate is preferred for the majority of applications, since Pd is an expensive material. S. Horiuchi and Y. Nakao have reported a simple method of depositing catalytic Pd colloids on various kinds of materials such as polymer films, glass, metals, and more [52]. The Pd colloid is about 5 nm in a diameter and can effectively catalyze various metal depositions, e.g., Cu, Ag, Au, and Pt. It should also be noted that the Pd colloidal solution can be left for years under a normal atmosphere without losing its function, and most of the chemicals used here are environmentally friendly.

The Pd colloidal solution is prepared by the following recipe. First, 1 g of Sucrose and 10 mg of Dextran (MW : 100,000-200,000) was dissolved in 92.5 mL of DI water and stirred. Adding 2.5 mL of the mixture of $PdCl_2$ (20 mM) and NaCl (100 mM), and 5 mL of

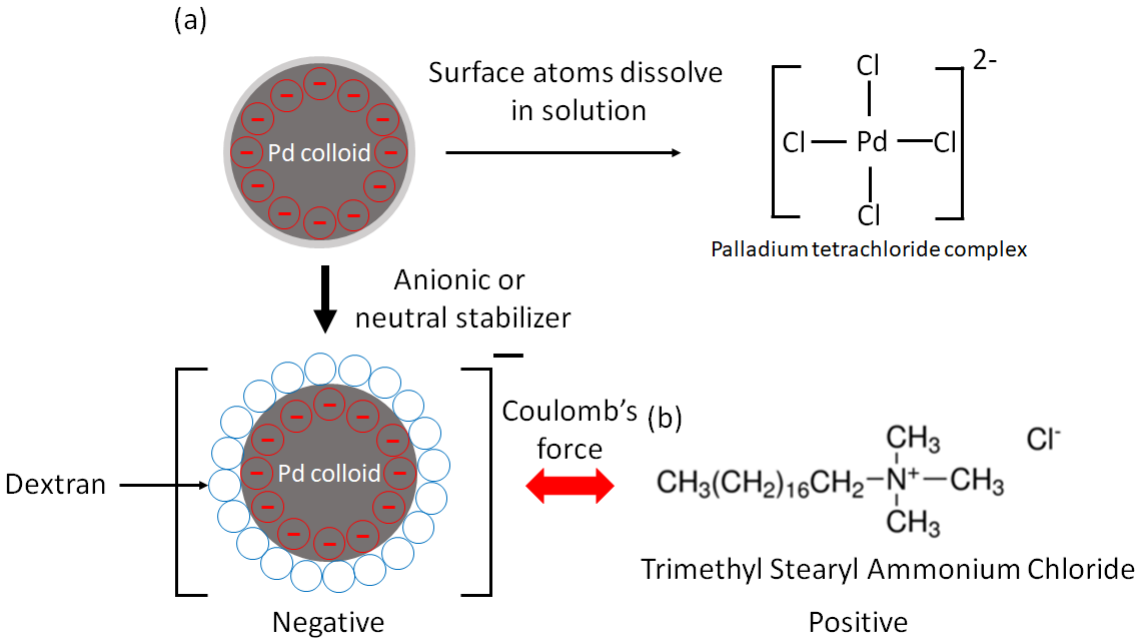

Figure 4-1 (a) Schematics of synthesizing Pd colloids and (b) the chemical structure of Trimethyl Stearyl Ammonium Chloride.

$NaBH_4$ (40 mM) to it, the solution was heated at 80 ˚C for 24 hours in an oil bath. Because the Pd colloids made by this process are negatively charged, they can be adsorbed on a positively charged surface by Coulomb's force and such a surface can be prepared by cationic surfactants. Here, Stearyl Trimethyl Ammonium Chloride (SC) was used as one of them. Schematics of the mechanism of synthesizing Pd colloids and their adsorption on the treated surface are shown in Figure 4-1. Pd atoms create clusters in the solution and some atoms that are on the surface of the clusters are dissolved in the solution as Pd^{2+} even though the solubility of Pd in the solution is very low. As a result, the Pd clusters are negatively charged enough to satisfy the electrical neutrality. A water-soluble polymer, used here in the form of Dextran, is adsorbed on the surface of the Pd clusters to create Pd colloids with negative

charges. On the other hand, SC is ionized to a SC ion in the solution by releasing Cl^- into the solution, and since its long carbon chain is hydrophobic, it tends to be adsorbed on a hydrophobic surface. Those positive ions and negative colloids attract each other and as a result, the sample surface will be coated with Pd colloids with a single colloidal layer.

4.3 Electroless plating for broadband light absorber applications

Broadband light absorbers have been studied intensively in recent years because of their wide applications, such as solar energy harvesting [45,95–97], stealth devices [98,99], and sensors [100]. Among various designs for broadband light absorbers, the major ones are porous materials coated with a metal [45,95,101,102], multi-layer films of metal/dielectric materials [103,104], nanowire arrays [105,106], and ring resonators [107–109]. While many experimental works based on these designs have been studied, most fabrication methods require expensive processes such as the chemical vapor deposition (CVD), sputtering, or dry etching. This is mainly due to two reasons: fabricating porous structures, and difficulty in coating thin absorptive metals. To improve these aspects, we propose to use an Anodized Aluminum Oxide (AAO) membrane as a substrate and electroless plating of metals on it using the Pd colloidal solution introduced in the previous section. AAO membranes are known as an inexpensive porous material that can be fabricated by a wet chemical process, called anodized oxidation [110], of Al as shown in Figure 4-2. Many parameters such as the diameter of the hole, interpore distance, and thickness of the membrane can be engineered by the fabrication conditions. The holes can even be less than 100 nm in a diameter while penetrating the entire membrane, e.g., 50 μm, resulting in the ultrahigh aspect ratio (>1:500).

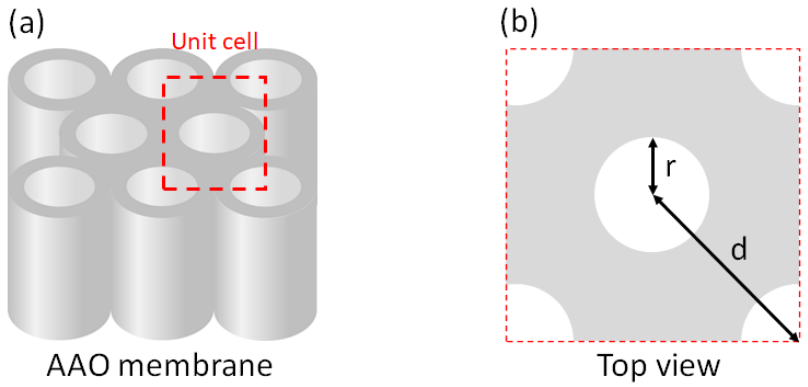

Figure 4-2 Schematics of (a) AAO membrane and the unit cell of it is indicated by the red dashed square, and (b) the top view of the unit cell. r is the pore radius and d is the interpore distance.

These membranes are commercially available, and the commercial price of single piece is about $25 for a circular AAO membrane whose diameter is 1 cm, thickness is 50 μm, and hole diameter is 200 nm. There are several previous studies on broadband light absorbers using AAO membranes as a template [45,111,112], but to the best of our knowledge, vacuum processes such as CVD or sputtering were employed to coat a thin metal layer on the holes. As previously mentioned, these processes are expensive, and they have the disadvantage of being unable to deposit metals deeply on the inner walls of the holes. Therefore, even though ultrahigh aspect ratio structures are employed in those studies, the entirety of the holes were not completely utilized to achieve high absorption, leaving room for improvement. Our process using electroless plating can coat metal on the sidewalls of the holes deeply, since the solution can flow into the depth of the holes, and the chemical reaction reducing the metal ions to pure metals occurs simultaneously where the Pd colloids are. As a result, very uniform and conformal coating can be achieved even on porous, ultrahigh aspect ratio structures.

4.4 Simulation and design of the broadband light absorber using an AAO membrane

First, the absorptance simulation was carried out by RETICOLO in Matlab. RETICOLO can implement the rigorous coupled wave analysis (RCWA). RCWA can only be applied for periodic structures, but it can calculate the reflectance, transmittance, or diffraction very fast. In this study, since the absorptance of the device (which can be calculated from the reflectance and transmittance) is of interest, RCWA is one of the best methods for these computations. The simulation model is shown in Figure 4-3. In RCWA, the simulation model is defined by its periodic structures using the cross-section. This model consists of the air on both sides, and the metal cylinders coated on the inner walls of the AAO pores. A linearly polarized wave is incident from top to the z direction with the incident angle

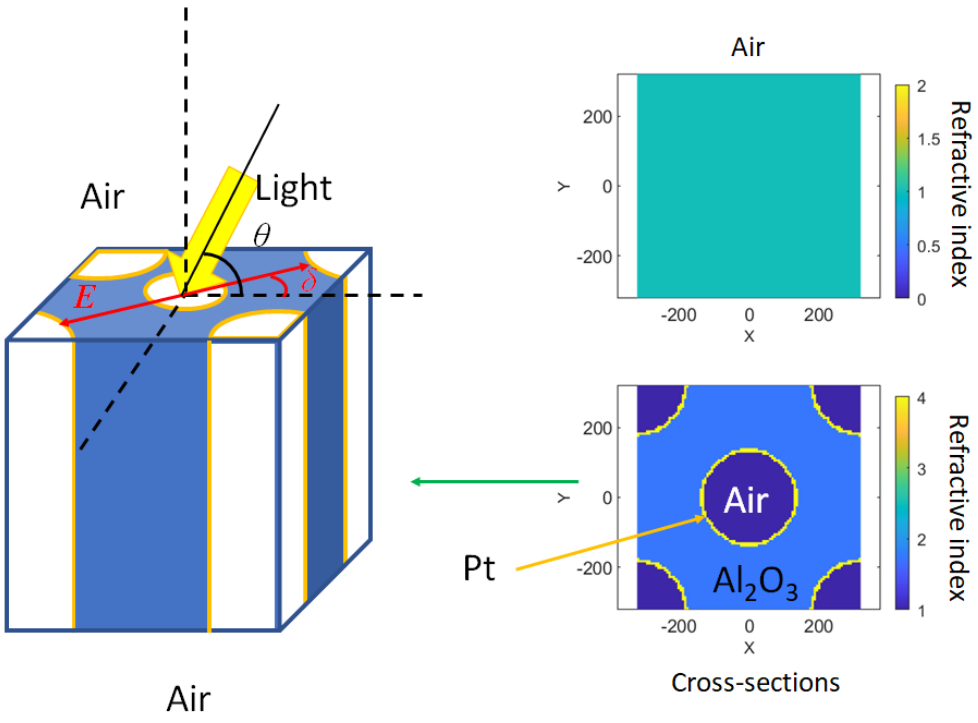

Figure 4-3 A simulation model by RCWA.

θ of 0-75˚. Since RETICOLO requires a specific polarization for the incident light, simulations were performed for several major angles. As the periodic structures of this device is C4 symmetry, the simulated results for δ = 0˚, 15˚, 30˚, and 45˚ were averaged to calculate the absorptances for unpolarized light. The parameters for the AAO membrane swept in this study are the interpore distance, pore radius, coated metal, and its thickness. The thickness of the AAO membrane was fixed at 50 μm, the pores are close packed, and the coated metal covers the whole sidewalls of the pores uniformly.

Figure 4-4 (a)-(c) show simulation results in which the interpore distance d is 450 nm, the coated metal is Pt, and its thickness t is 20 nm with the incident angles of the light θ from 0˚ to 75˚ for r = 100 nm, 140 nm, and 180 nm. All of them show very high absorptions (> 90%) for 0-30˚ and the absorptions are around 60% even for the large angle, 75˚. It is also observed that the larger the radius becomes, the higher the absorption gets in the whole range (300-2400 nm). Figure 4-4 (d)-(f) shows simulation results in which the coated metal is 20 nm thick Pt but the interpore distance d and the radius r are 400-500 nm and 100-180 nm, respectively. When the radius is 100 nm or 140 nm, different interpore distances show very similar absorptions. However, in the case that the radius is 180 nm, the differences in the interpore distance largely change the absorptions in the near IR range. According to those results, the best conditions when the coated metal is 20 nm thick Pt, is r = 180 nm and d = 450 nm.

Figure 4-5 shows the results with d = 450 nm, r = 180 nm, the incident angle of light is 0˚, and Pt is coated with t = 3-20 nm. In the visible wavelength range, they show almost

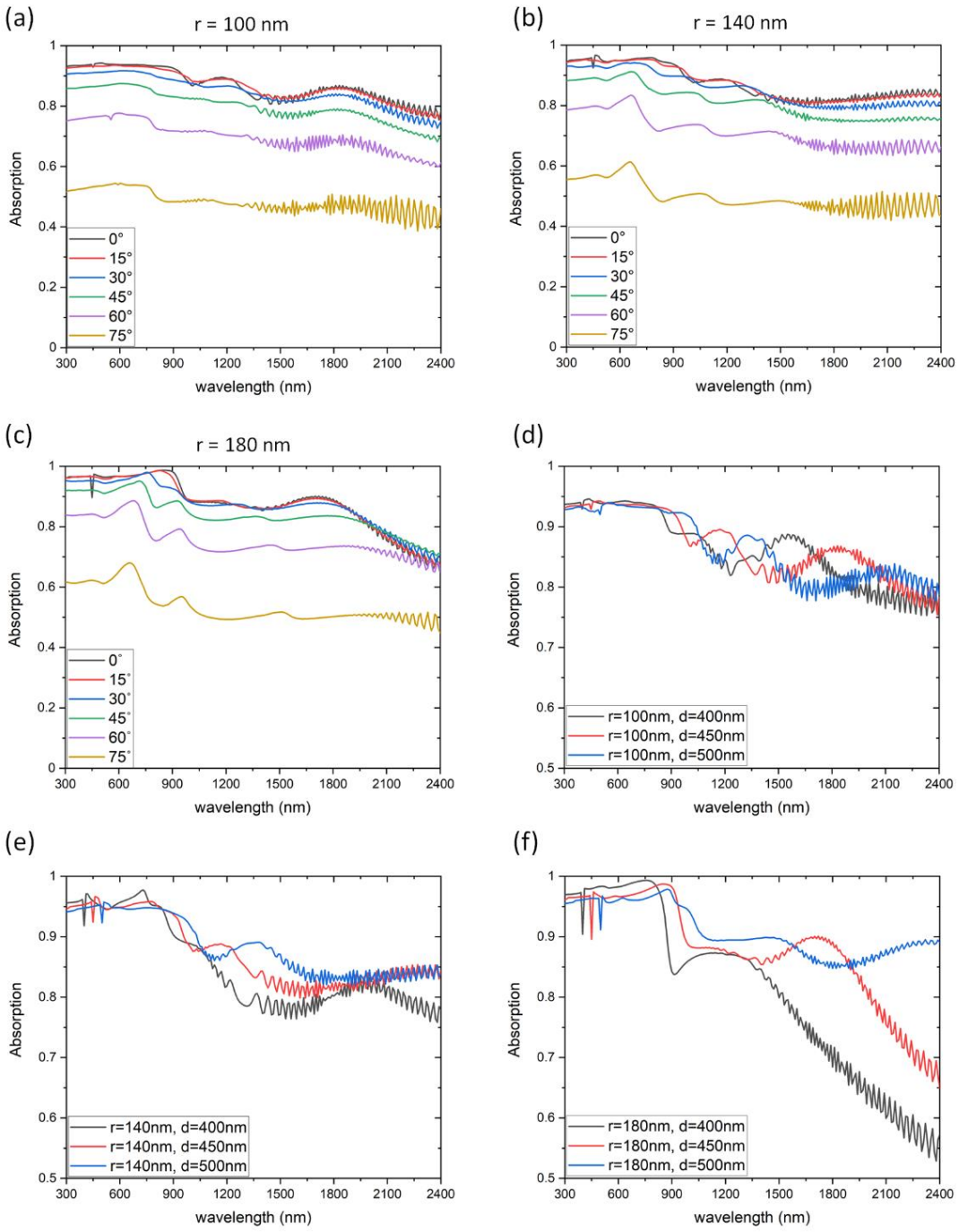

Figure 4-4 Simulation results for various parameters. The coated metal is Pt, d = 450 nm, t = 20 nm, and the incident angle of θ = 0-75˚ for (a) r = 100nm, (b) r = 140 nm, and (c) r =180 nm. The coated metal is Pt, t = 20 nm, and the incident angle of θ = 0˚ for (d) r = 100 nm and d = 400-500 nm, (e) r = 140 nm, d = 400-500 nm, and (f) r = 180 nm, d = 400-500 nm.

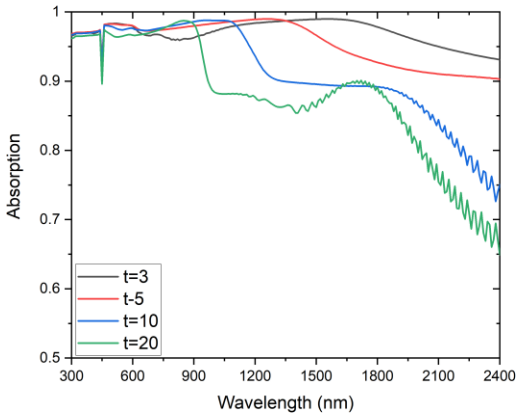

Figure 4-5 Simulation results for different Pt thicknesses. The interpore distance d = 450 nm, the radius r is 180 nm, the incident angle of light is 0˚, and the thickness of Pt is swept from 3 nm to 20 nm.

the same absorptions, but the thinner metal has higher absorption in the near IR range. This is because the incident light transmits more when the metal is thinner and experiences reflections and absorptions like a Fabry-Pérot cavity. The dips observed at 450 nm for all curves are believed to correspond to the interpore distance d = 450 nm. With this minor exception, our designs show very high absorptions (> 95%) in 400-1100 nm, which exceeds the results reported in previous studies using more complicated fabrication process as shown in the comparison of Figure 4-6 [45]. A similar design was employed in the previous study, but atomic layer deposition (ALD) was used to deposit a thin Ir layer on the sidewalls of the pores. Since ALD is a vacuum process and the deposition rate can be as slow as one atomic layer per cycle, the fabrication cost becomes more expensive than a wet chemical process. Thus, not only are the simulated absorptions for the broadband light shown, but also the advantages of the fabrication process and cost.

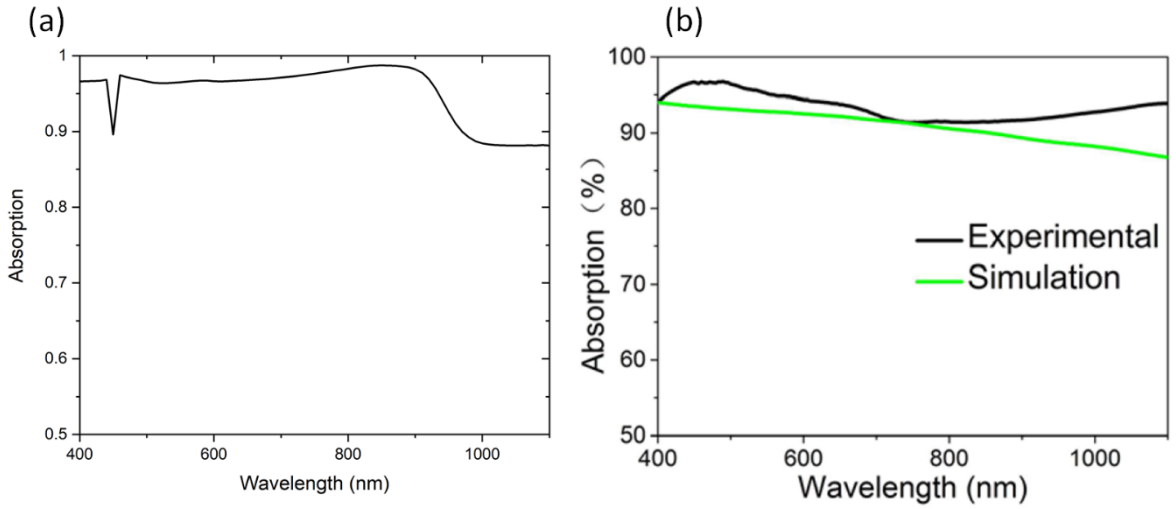

Figure 4-6 A comparison of the simulation result of this study with the previous work. (a) The absorption when d = 450 nm, r = 180 nm, Pt thickness t = 20 nm, and the incident angle is 0˚. (b) The reference data from the previous study when the AAO thickness is 200 nm and it is on a glass substrate, d = 100 nm, r = 48 nm, the metal is 3 nm thick Ir, adapted from literature [45]. Copyright (2017) AIP Publishing.

4.5 Experimental results and discussions

Three different AAO membranes were obtained from Shenzhen Topmembranes Technologies Co., Ltd. These AAO membranes have holes through the entire substrate (50 μm) and they are closely packed in plane. The interpore distance of them is 450 nm, and the radii are 100 nm, 140 nm, and 180 nm. The electroless plating process used here is the same process described in the section 4.2, but in order to enhance diffusions, each step was done with sonication. After the Pd colloids deposition, Pt electroless plating was performed in 20 mM of H_2PtCl_6 and 80 mM of Ascorbic acid with sonication and heat. Figure 4-7 shows the AAO membranes at each step of the fabrication. The original AAO membranes are all semitransparent, but after the Pd colloids deposition, they already showed dark colors. Although the samples appear slightly nonuniform at this stage, after the Pt electroless plating

with sonication, all of them appear very deep black, which indicates high absorption in the visible wavelength range. Figure 4-8 shows SEM images of the Pt coated AAO membrane and exposed Pt tubes by removing the AAO membrane with an acid solution. Because of the capillary force, the Pt tubes aggregated in the picture, but long Pt tubes with thin thickness were successfully fabricated.

The transmittances and specular reflections for the wavelength of 300-2400 nm and θ = 8-60˚ were measured by a UV/Vis/NIR spectrometer (LAMBDA 1050: PerkinElmer), and the normal reflectance was measured by a lab-made spectrometer. Figure 4-9 (a) and (b) show the measured transmittances for r = 140 nm and 180 nm, (c) shows the measured normal

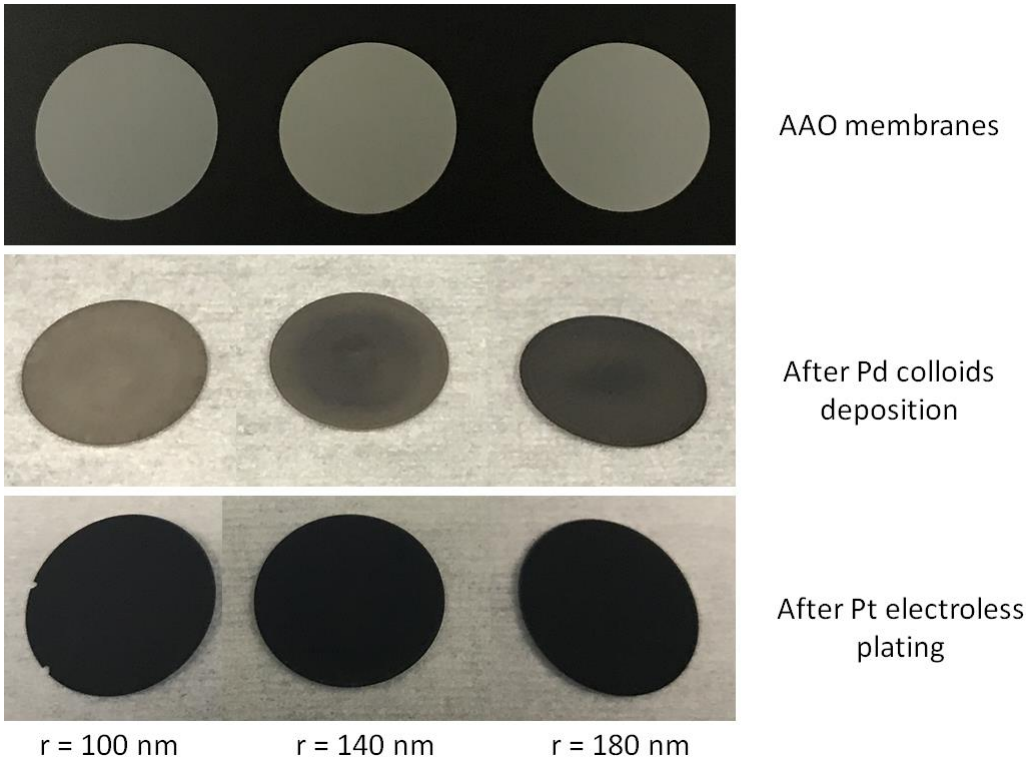

Figure 4-7 AAO membranes at each step. Semitransparent appearances became deep black after the Pt electroless plating process.

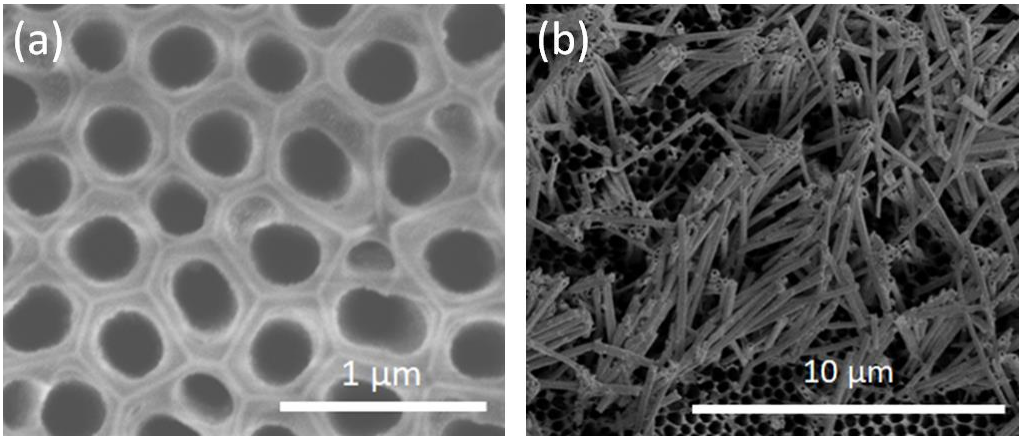

Figure 4-8 SEM images of Pt coated AAO membranes. (a) A top view and (b) exposed Pt tubes after AAO was dissolved in an acid solution.

reflectance for r = 140 nm, and (d) is the specular reflectances for the samples with r = 140 nm. Comparing with the simulated results shown in Figure 4-9 (e) and (f), very low transmittances were observed for both samples, and the reflectances are also lower than the simulation. This is most likely due to the difference of the pore structures in the real device from the simulation model. Although the simulation model employs a circular pore with a completely periodic structure, as Figure 4-8 (a) shows, the real device has an imperfect circular pore shape and a comparably random configuration rather than periodic. These parameter fluctuations improve the absorptions in the broadband range. A similar study also revealed the same tendency, i.e., the experimental result shows better absorption than the simulation [45]. Figure 4-10 shows a comparison of the simulated absorptions for different metals with the previous study employing a similar design. Not only does our design show higher absorption for various metals, but the fabrication process has a huge cost advantage, since only wet chemical processes were employed. Though the metal used in our work is Pt,

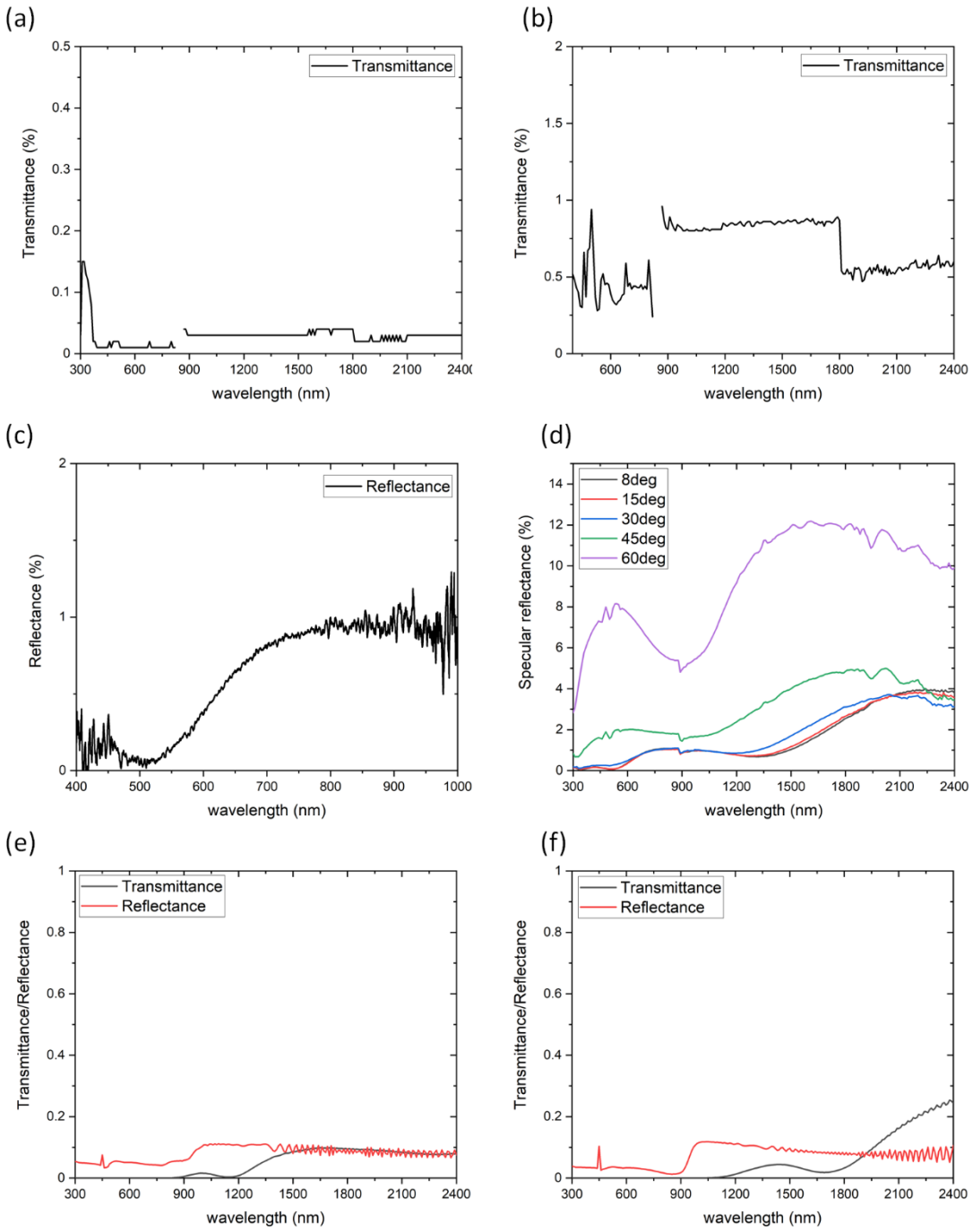

Figure 4-9 The transmittance and reflectance. The experimental measurements of transmittance for (a) r = 140 nm and (b) r = 180 nm, and of (c) the normal reflection for r =140 nm in the range of 400-1000 nm and (d) specular reflection for θ = 8-60˚. Simulated transmittance and reflectance for (e) r = 140 nm and (f) r = 180 nm.

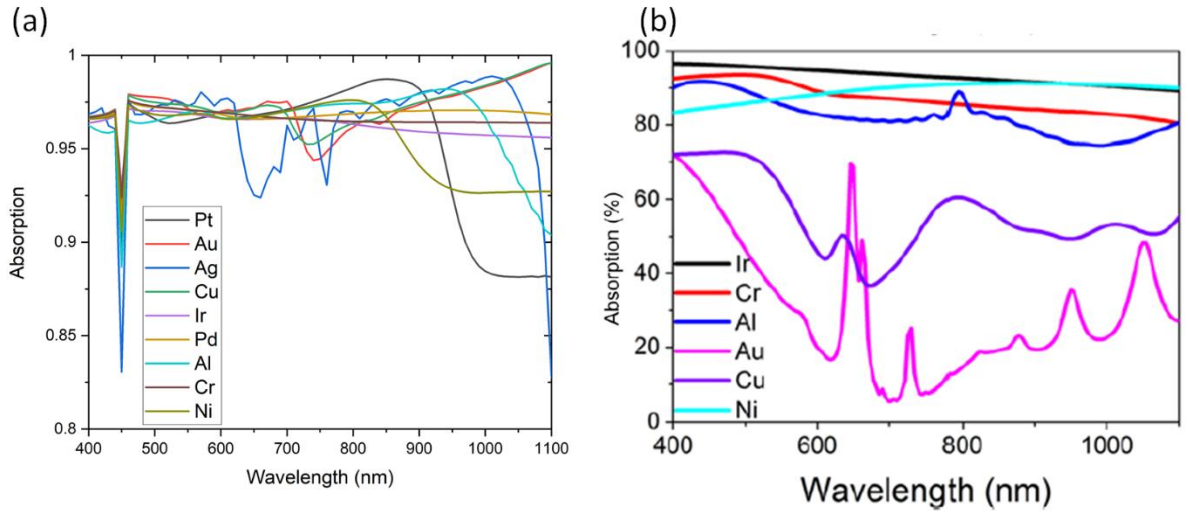

Figure 4-10 A comparison of simulated results for various metals. (a) The result simulated in this work for d = 450 nm, r = 180 nm, t = 20 nm, and $\theta = 0^{\circ}$. (b) The reference, adapted from literature [45]. Copyright (2017) AIP Publishing.

other less expensive metals such as Cu, Cr, and Ni can produce the same or similar absorptions. This work shows a promising process for producing fabrications of broadband light absorbers at a low cost. Moreover, this confirmed the ability of electroless plating to coat thin metal films deeply into tiny structures. This technique could be used to resolve issues in current conventional processes, such as using a vacuum deposition which cannot deeply deposit materials.

4.6 Structural colors using metal/dielectric/metal Fabry-Pérot cavities

Most paint colors are composed of organic pigments or inorganic pigments which absorb certain wavelengths of light and reflect the rest. This is how we see colors from those materials. On the other hand, a new type of color paints called structural colors have been studied intensively in recent years because of their superior characteristics to conventional

paints [113]. For example, structural colors can have higher reflectance than the pigment-based colors, i.e., the color looks brighter, and they will not degrade from exposure to sunlight.

The major schemes of the structural color are based on the plasmonic resonances [114,115], wave-guide mode resonances [116,117], and Fabry-Pérot cavities [47,48]. The ones utilizing plasmonic resonances or wave-guide resonances are typically too expensive to introduce into industries because they require nanofabrications such as lithography or etching. The other one using Fabry-Pérot cavities consists of thin metal/dielectric/metal layers, and could potentially overcome the fabrication cost issue if a scalable low-cost deposition process is employed. The basic design of the structural color using Fabry-Pérot cavities is shown in Figure 4-11. When the light is incident to the top metal layer with an incident angle of θ_1, it partially transmits into the dielectric layer and partially reflects. The transmitted light propagates into the dielectric layer and reflects at the bottom

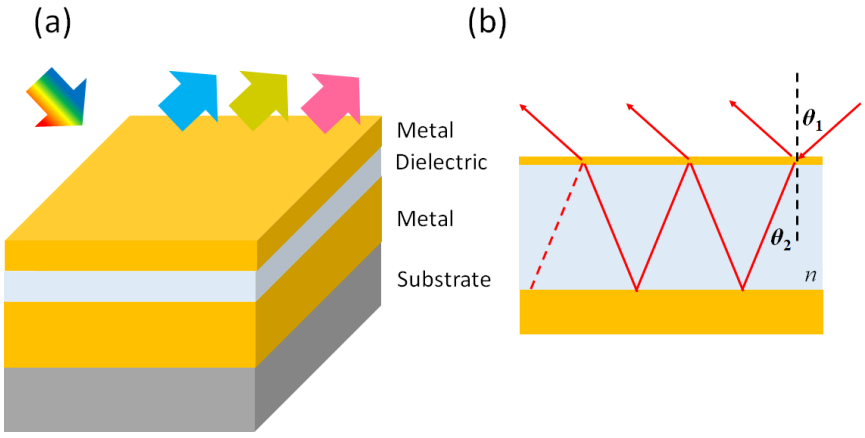

Figure 4-11 Schematics of the structural color based on a Fabry-Pérot cavity. (a) Metal/dielectric/metal layers and (b) a schematic of the cavity.

metal layer. The reflected light at the bottom metal layer partially transmits the top layer and partially reflects again. As these go on, both constructive and destructive interferences of light will be created, which results in a certain color depending on the wavelength of the constructive interference. One of the advantages of this structural color design is that the color created by the Fabry-Pérot cavity can be engineered by changing the thickness of the dielectric layer while fixing the two metal layer thicknesses and material choices. Moreover, when the refractive index of the dielectric layer is comparably high (e.g. n = 2 for visible wavelength), the created color shows an excellent angular independency, which means the color does not change depending on the viewing angle. Given that the diffracted angle of the incident light in the dielectric layer is θ_2, by Snell's law,

$$\sin\theta_1 = n\sin\theta_2 \tag{4.6.1}$$

$$\theta_2 = \sin\theta^{-1}\frac{\sin\theta_2}{n} \tag{4.6.2}$$

are satisfied. Therefore, for the high n, θ_2 becomes almost independent of θ_1. This is the mechanism of the angular independent color.

In 2018, Toyota sold the first automobile painted with structural color paints. Despite the fact that they commercialized the structural color paints, the price of the car was more expensive compared to the same model using conventional paints. This price difference was attributed to the fabrication cost, which produced the structural color paints using a vacuum process. In a recent study, a non-vacuum process using wet chemical depositions has been performed to reduce costs [47]. In the study, Au/CuO_2/Au layers were used as a Fabry-Pérot cavity to create three primary colors: Cyan, Magenta, and Yellow. However, the CuO_2

electroplating process is slightly complicated, and the electroplating solution degrades easily in a normal environment. This makes it difficult to use in industries, and increases the fabrication cost in addition to the cost of the Au used for both metal layers. Thus, there is a great need for alternative processes which can deposit the dielectric layer and metal layers.

In this dissertation, Zinc Oxide (ZnO) electroplating is introduced as an alternative process for the dielectric layer deposition, as well as Cu electroless plating using Pd catalytic colloids for the top metal layer. ZnO is known as a transparent semiconductor and has a comparably high refractive index (~1.9 for the visible wavelength [118]) which enables the angular independent structural colors. Although the process requires bubbling O_2 gas into the electroplating solution, the solution itself is very simple and stable in a normal environment. Since the cost of Cu is much less expensive compared with Au while showing the high reflectance in the visible wavelength and high stability, it is a promising candidate to replace Au in this technology.

4.7 Transfer-matrix method

First, in order to simulate the performance of ZnO and Cu layers for structural colors, the transfer-matrix method was employed. The transfer-matrix method is a method that can calculate the optical properties for multi-layer films. Given that the light is incident on N layers and a substrate as Figure 4-12 shows where the refractive index of the *i*th layer is n_i and the incident angle to the first layer is θ_0. The electric field in the *i*th layer can be expressed by superposing two waves propagating the z+ and z- directions respectively as

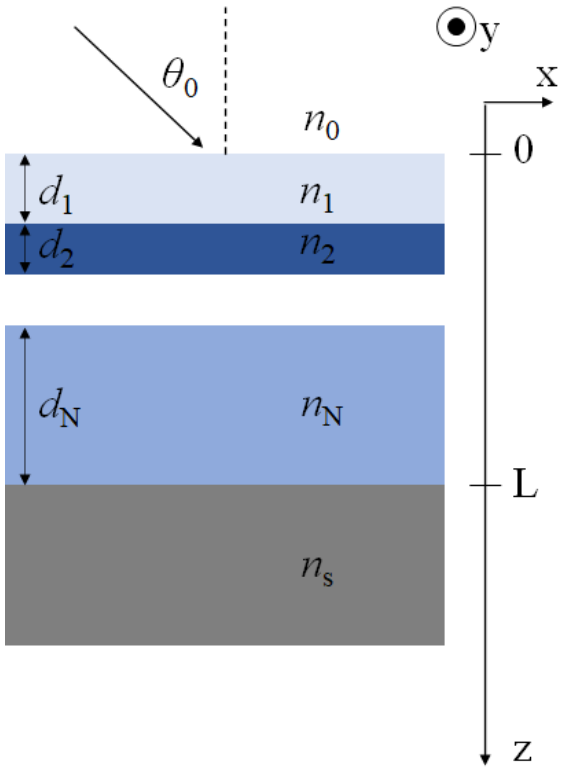

Figure 4-12 A schematic of multi-layer films.

$$E_{iy}(\boldsymbol{r}) = E_i e^{i(\mathbf{k_{i+}}\cdot\boldsymbol{r}-\omega t)} + E_i' e^{i(\mathbf{k_{i-}}\cdot\boldsymbol{r}-\omega t)}, \qquad r = (x, y, z - L_i) \tag{4.7.1}$$

$$\mathbf{k_{i+}} = (k_x, 0, k_{iz}) \,, \mathbf{k_{i-}} = (k_x, 0, -k_{iz}) \tag{4.7.2}$$

and by Snell's law

$$k_x = n_i k_0 \sin\theta_i = n_{i-1} k_0 \sin\theta_{i-1} = \cdots = n_0 k_0 \sin\theta_0 \tag{4.7.3}$$

$$k_{iz} = \sqrt{n_i^2 k_0^2 - k_x^2} = \sqrt{n_i^2 k_0^2 - n_i^2 k_0^2 \cos\theta_i} = n_i k_0 \cos\theta_i \tag{4.7.4}$$

By Maxwell's equation, the x component of the magnetic field is

$$-\frac{\partial \mathbf{B}}{\partial t} = i\omega\mu_0 \mathbf{H} = \nabla \times \mathbf{E} \tag{4.7.5}$$

$$= -\frac{\partial E_{iy}}{\partial z} \tag{4.7.6}$$

$$= -E_i i k_z e^{i(\mathbf{k_{i+}}\cdot \boldsymbol{r} - \omega t)} + E_i' i k_z e^{i(\mathbf{k_{i-}}\cdot \boldsymbol{r} - \omega t)} \tag{4.7.7}$$

$$H_{ix}(z) = \frac{-k_{iz}}{\omega\mu_0}\left(E_i e^{i(\mathbf{k_{i+}}\cdot \boldsymbol{r} - \omega t)} - E_i' e^{i(\mathbf{k_{i-}}\cdot \boldsymbol{r} - \omega t)}\right) \tag{4.7.8}$$

Substituting $z = L_i$ in (4.7.1) and (4.7.8),

$$E_{iy}(z = L_i) = (E_i + E_i')e^{ik_x x - i\omega t} \tag{4.7.9}$$

$$H_{ix}(z = L_i) = \alpha_i(-E_i + E_i')e^{ik_x x - i\omega t} \tag{4.7.10}$$

where $\alpha_i = \frac{k_{iz}}{\omega\mu_0}$

Therefore,

$$E_i = \frac{1}{2}\left(E_{iy}(z = L_i) - \frac{H_{ix}(z = L_i)}{\alpha_i}\right)e^{-ik_x x + i\omega t} \tag{4.7.11}$$

$$E_i' = \frac{1}{2}\left(E_{iy}(z = L_i) + \frac{H_{ix}(z = L_i)}{\alpha_i}\right)e^{-ik_x x + i\omega t} \tag{4.7.12}$$

Then substituting them to (4.7.1) again

$$E_{iy}(\boldsymbol{r}) = \frac{1}{2}\left(E_{iy}(z=L_i) - \frac{H_{ix}(z=L_i)}{\alpha_i}\right)e^{ik_{iz}z} + \frac{1}{2}\left(E_{iy}(z=L_i) + \frac{H_{ix}(z=L_i)}{\alpha_i}\right)e^{-ik_{iz}z} \quad (4.7.13)$$

$$= \frac{1}{2}\left(e^{ik_{iz}z} + e^{-ik_{iz}z}\right)E_{iy}(z=L_i) - \frac{1}{2\alpha_i}\left(e^{ik_{iz}z} + e^{-ik_{iz}z}\right)H_{ix}(z=L_i) \quad (4.7.14)$$

and to (4.7.8)

$$H_{ix}(\boldsymbol{r}) = -\frac{\alpha_i}{2}\left(e^{ik_{iz}z} - e^{-ik_{iz}z}\right)E_{iy}(z=L_i) + \frac{1}{2}\left(e^{ik_{iz}z} + e^{-ik_{iz}z}\right)H_{ix}(z=L_i) \quad (4.7.15)$$

These can be written in the matrix form

$$\begin{pmatrix}E_{iy}(z)\\H_{ix}(z)\end{pmatrix} = \begin{pmatrix}\frac{1}{2}\left(e^{ik_{iz}z} + e^{-ik_{iz}z}\right) & -\frac{1}{2\alpha_i}\left(e^{ik_{iz}z} + e^{-ik_{iz}z}\right)\\ -\frac{\alpha_i}{2}\left(e^{ik_{iz}z} - e^{-ik_{iz}z}\right) & \frac{1}{2}\left(e^{ik_{iz}z} + e^{-ik_{iz}z}\right)\end{pmatrix}\begin{pmatrix}E_{iy}(z=L_i)\\H_{ix}(z=L_i)\end{pmatrix} \quad (4.7.16)$$

$$\equiv \mathrm{M}_i\begin{pmatrix}E_{iy}(z=L_i)\\H_{ix}(z=L_i)\end{pmatrix} \quad (4.7.17)$$

In case that the medium is loss less, since *k* is a real number, (4.7.16) can be

$$\begin{pmatrix}E_{iy}(z)\\H_{ix}(z)\end{pmatrix} = \begin{pmatrix}\cos(k_{iz}z) & -\frac{i}{\alpha_i}\sin(k_{iz}z)\\ -i\alpha_i\sin(k_{iz}z) & \cos(k_{iz}z)\end{pmatrix}\begin{pmatrix}E_{iy}(z=L_i)\\H_{ix}(z=L_i)\end{pmatrix} \quad (4.7.18)$$

$$\begin{pmatrix}E_{iy}(z=L_i)\\H_{ix}(z=L_i)\end{pmatrix} = \mathrm{M}_i^{-1}\begin{pmatrix}E_{iy}(z)\\H_{ix}(z)\end{pmatrix} \quad (4.7.19)$$

where

$$\mathrm{M}_i^{-1} = \begin{pmatrix} \cos(k_{iz}z) & \frac{i}{\alpha_i}\sin(k_{iz}z) \\ i\alpha_i \sin(k_{iz}z) & \cos(k_{iz}z) \end{pmatrix} \tag{4.7.20}$$

Considering multilayer structures,

$$\begin{pmatrix} E_{0y}(0) \\ H_{0x}(0) \end{pmatrix} = \mathrm{M} \begin{pmatrix} E_{sy}(L) \\ H_{sx}(L) \end{pmatrix} \tag{4.7.21}$$

where

$$\mathrm{M} = \mathrm{M}_1^{-1}\mathrm{M}_2^{-1}\mathrm{M}_3^{-1} \cdots \mathrm{M}_\mathrm{n}^{-1} \tag{4.7.22}$$

and since there are only the incident wave and reflected wave in the top region, and the transmitted wave in the bottom region,

$$E_{0y}(z) = (\exp(ik_{0z}z) + r\exp(-ik_{0z}z))\exp(ik_x x) \tag{4.7.23}$$

$$E_{sy}(z) = t\exp\big(ik_{sz}(z-L)\big)\exp(ik_x x) \tag{4.7.24}$$

Here, *r* is the reflectance and *t* is the transmittance. The magnetic fields can be calculated by the derivatives of (4.7.23) and (4.7.24) respect to z.

$$H_{0x}(z) = -\alpha_0(\exp(ik_{0z}z) - r\exp(-ik_{0z}z))\exp(ik_x x) \tag{4.7.25}$$

$$H_{sx}(z) = -\alpha_s t\exp\big(ik_{sz}(z-L)\big)\exp(ik_x x) \tag{4.7.26}$$

Substituting z = 0 for (4.7.23) and (4.7.25), and z = L for (4.7.24) and (4.7.26),

$$E_{0y}(0) = (1 + r)\exp(ik_x x) \tag{4.7.27}$$

$$H_{0x}(0) = -\alpha_0(1 - r)\exp(ik_x x) \tag{4.7.28}$$

$$E_{sy}(L) = t\exp(ik_x x) \tag{4.7.29}$$

$$H_{sx}(L) = -\alpha_s t\exp(ik_x x) \tag{4.7.30}$$

Expressing these using matrices,

$$\begin{pmatrix} 1+r \\ \alpha_0(-1+r) \end{pmatrix} = \mathrm{M}\begin{pmatrix} t \\ -\alpha_s t \end{pmatrix} \tag{4.7.31}$$

$$\begin{pmatrix} 1 \\ -\alpha_0 \end{pmatrix} + \begin{pmatrix} 1 \\ \alpha_0 \end{pmatrix} r = \mathrm{M}\begin{pmatrix} 1 \\ -\alpha_s \end{pmatrix} t \tag{4.7.32}$$

$$\begin{pmatrix} 1 \\ \alpha_0 \end{pmatrix} r - \begin{pmatrix} \mathrm{M}_{11} & \mathrm{M}_{12} \\ \mathrm{M}_{21} & \mathrm{M}_{22} \end{pmatrix}\begin{pmatrix} 1 \\ -\alpha_s \end{pmatrix} t = -\begin{pmatrix} 1 \\ -\alpha_0 \end{pmatrix} \tag{4.7.33}$$

$$\begin{pmatrix} 1 & -(\mathrm{M}_{11} - \alpha_s \mathrm{M}_{12}) \\ \alpha_0 & -(\mathrm{M}_{21} - \alpha_s \mathrm{M}_{22}) \end{pmatrix}\begin{pmatrix} r \\ t \end{pmatrix} = \begin{pmatrix} -1 \\ \alpha_0 \end{pmatrix} \tag{4.7.34}$$

Since the determinant is

$$\det\begin{pmatrix} 1 & -(\mathrm{M}_{11} - \alpha_s \mathrm{M}_{12}) \\ \alpha_0 & -(\mathrm{M}_{21} - \alpha_s \mathrm{M}_{22}) \end{pmatrix} = \alpha_0 \mathrm{M}_{11} - \alpha_0 \alpha_s \mathrm{M}_{12} - \mathrm{M}_{21} + \alpha_s \mathrm{M}_{22} \tag{4.7.35}$$

$$\begin{pmatrix} 1 & -(\mathrm{M}_{11} - \alpha_s \mathrm{M}_{12}) \\ \alpha_0 & -(\mathrm{M}_{21} - \alpha_s \mathrm{M}_{22}) \end{pmatrix}^{-1}$$

$$= \frac{1}{\alpha_0 \mathrm{M}_{11} - \alpha_0 \alpha_s \mathrm{M}_{12} - \mathrm{M}_{21} + \alpha_s \mathrm{M}_{22}}\begin{pmatrix} -(\mathrm{M}_{21} - \alpha_s \mathrm{M}_{22}) & \mathrm{M}_{11} - \alpha_s \mathrm{M}_{12} \\ \alpha_0 & 1 \end{pmatrix} \tag{4.7.36}$$

$$r = \frac{\alpha_0 \mathrm{M}_{11} - \alpha_0 \alpha_s \mathrm{M}_{12} + \mathrm{M}_{21} - \alpha_s \mathrm{M}_{22}}{\alpha_0 \mathrm{M}_{11} - \alpha_0 \alpha_s \mathrm{M}_{12} - \mathrm{M}_{21} + \alpha_s \mathrm{M}_{22}} \tag{4.7.37}$$

$$t = \frac{2\alpha_0}{\alpha_0 \mathrm{M}_{11} - \alpha_0 \alpha_s \mathrm{M}_{12} - \mathrm{M}_{21} + \alpha_s \mathrm{M}_{22}} \tag{4.7.38}$$

Thus, the reflectance and transmittance of the multi-layers can be calculated.

4.8 Computations of reflectance using transfer-matrix method

Simulations were performed on Matlab using the transfer-matrix method to calculate reflectance spectra in the visible wavelength range and their angular dependencies for 0-90˚. Figure 4-13 (a) shows the reflectances for three colors: yellow, magenta, and cyan, reported in the previous study using Au 20 nm/Cu_2O 20-75 nm/Au 100 nm from the top to bottom layer [47]. The colors of each curve correspond to the actual colors. Figure 4-13 (b) shows the simulation results when Cu_2O is replaced with ZnO with thicknesses of 40, 70, and 110 nm while the top and bottom layers are Au. All three curves show lower reflectances at their dips than the previous design, and cyan has a higher reflectance, i.e., the higher quality colors are expected for the new design. As seen in Figure 4-13 (c), when the top Au layer is replaced by Cu, there is little difference observed for all three curves. As Figure 4-14 shows, since reflectance, transmittance, and absorption spectra for Au and Cu are very similar, Cu is a promising candidate for replacing Au to achieve cost reduction.

Next, angular dependencies of these designs were simulated with an incident angle of 0-90˚. Figure 4-15 shows the results for all designs introduced above. All new designs have better angular independencies, especially for the large incident angles, which is simply

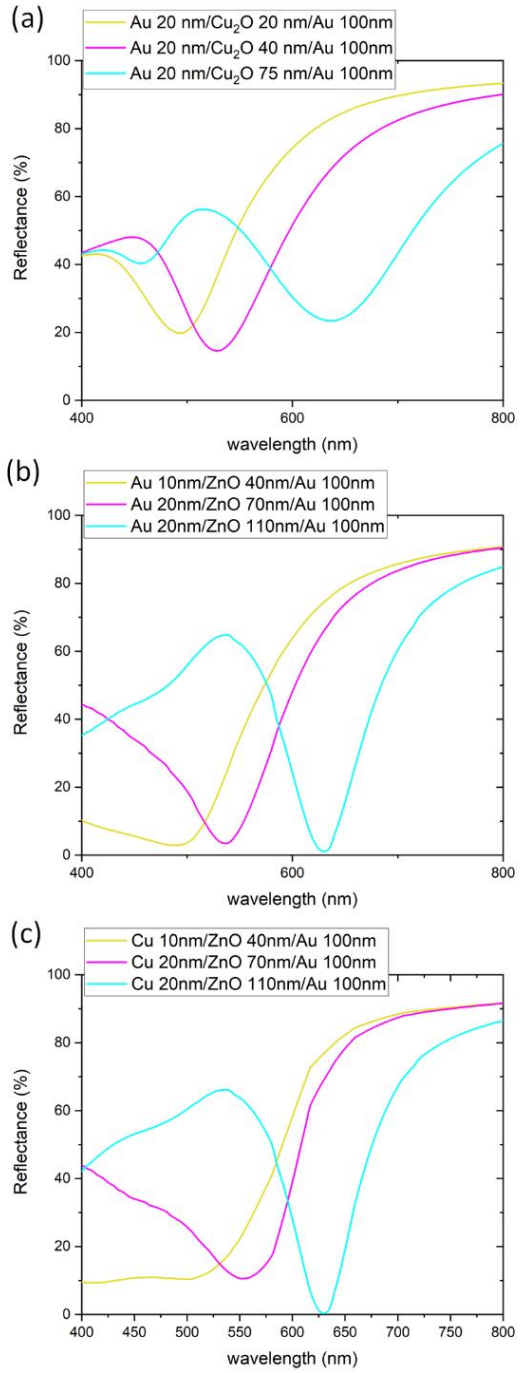

Figure 4-13 Simulation results of reflectances for different metal/dielectric/metal films by the transfer-matrix method. (a) The design employed in the previous work, Au 20 nm/Cu_2O x nm/ Au 100 nm for x = 20, 40, and 75 nm. (b) When Cu_2O is replaced by ZnO with the thicknesses of 40, 70, and 110 nm. (c) When the top Au layer is replaced with Cu and the ZnO thicknesses are 40, 70, and 110 nm.

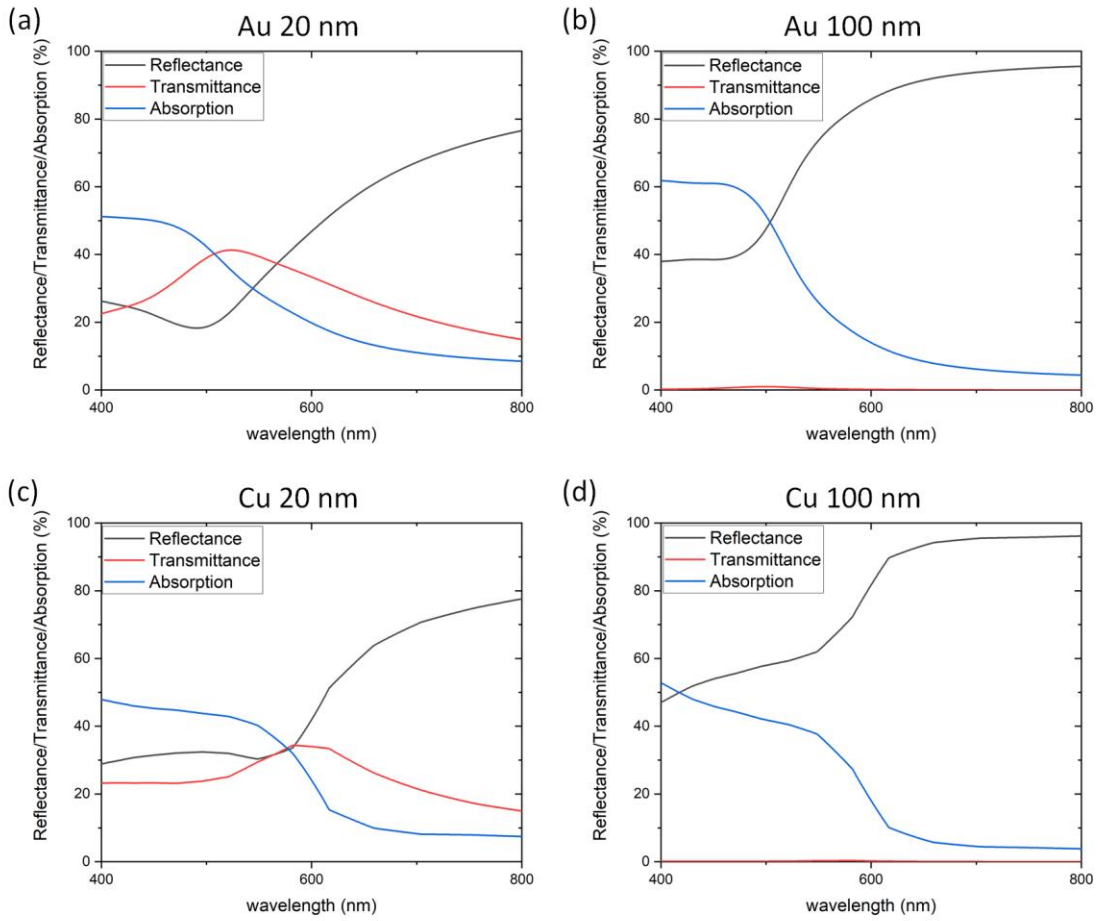

Figure 4-14 The reflectance, transmittance, and absorption for Au and Cu with 20 nm and 100 nm.

attributed to the high refractive index of ZnO. Thus, it has been computationally confirmed that replacing Cu_2O with ZnO and Au with Cu could improve both the quality of the structural colors and fabrication cost.

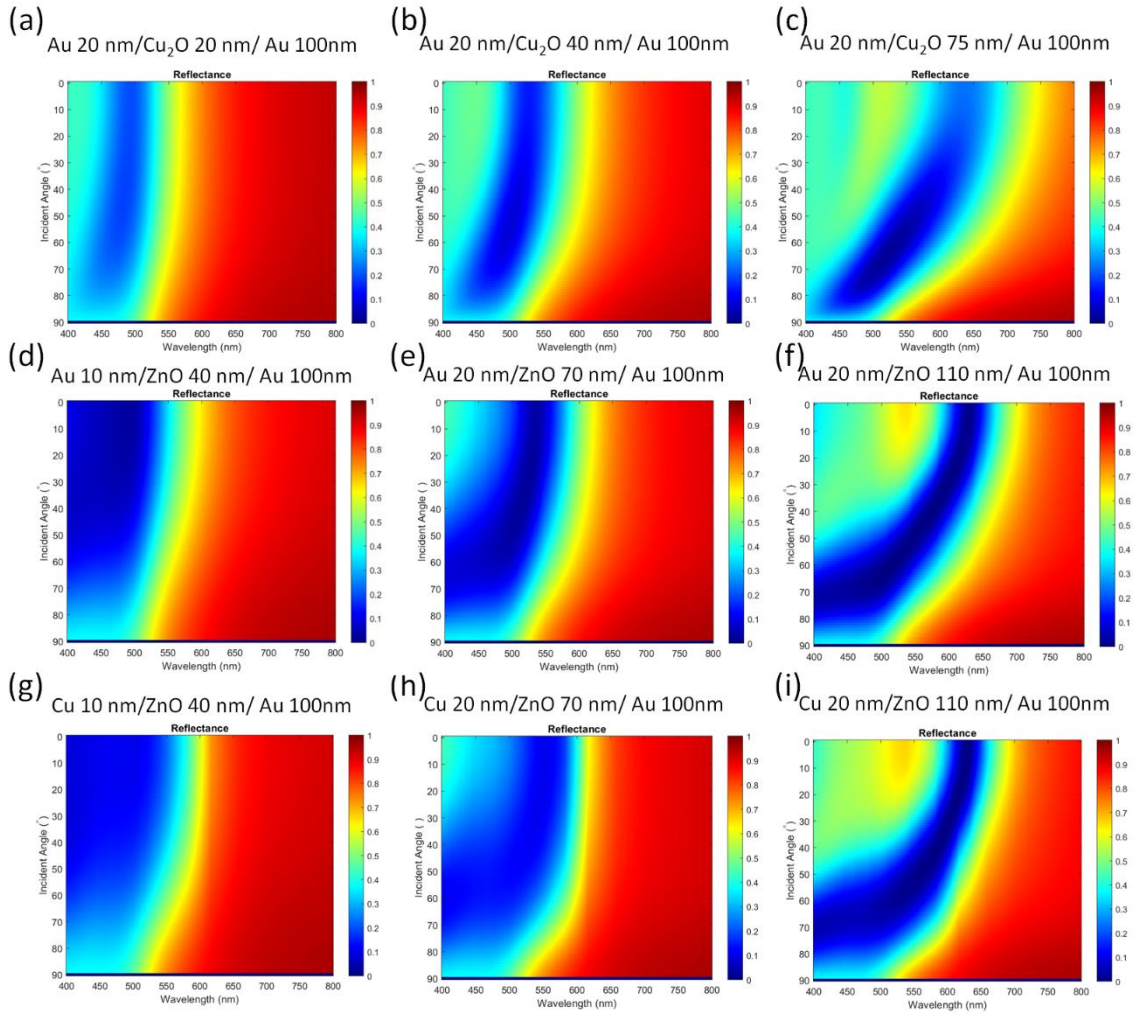

Figure 4-15 Angular dependencies of the reflectances for each design.

4.9 Experimental procedures for ZnO electroplating and Cu electroless plating

The reaction of ZnO electroplating is expressed by the following equations

$$\mathrm{Zn^{2+}} + \frac{1}{2}\mathrm{O_2} + 2\mathrm{e^-} \rightarrow \mathrm{ZnO}, \qquad E_0 = 0.93\ \mathrm{V/NHE} \tag{4.9.1}$$

$$\mathrm{Zn^{2+}} + 2\mathrm{e^-} \rightarrow \mathrm{Zn}, \qquad E_0 = -0.76\ \mathrm{V/NHE} \tag{4.9.2}$$

The ZnO electrodeposition solution is composed of $ZnCl_2$ (which is ionized to Zn^{2+} in the solution) with the concentration of 5×10^{-4} M to 5×10^{-2} M and KCl with the concentration of 0.1 M. The previous study on ZnO electrodeposition has reported that the surface morphology varies depending on the concentration of Zn^{2+}, and the deposited ZnO is conductive only when the solution temperature is over 50 ˚C [49]. This is because the deposited ZnO at the lower Zn^{2+} concentration and temperature forms hydroxide-containing films. Also, the higher Zn^{2+} concentrations can deposit zinc hydroxy-chloride films resulting in different surface morphologies [119]. This characteristic could have great potential for structural color applications, since by changing the process conditions, both a mirror-like surface and diffusive surface can be obtained, which expands the applications of this technology. A schematic of ZnO electroplating is shown in Figure 4-16. It is the three-electrode electroplating with O_2 bubbling using a Pt counter electrode and a saturated calomel reference electrode (SCE). As the starting substrate, Ti/Au with 5 nm/ 100 nm thicknesses were deposited on Si wafers by electron beam evaporations. The electroplating solution was placed in a water bath keeping the temperature at 60 ˚C, and O_2 gas was bubbled in the solution for 10 minutes before the electroplating.

Cu electroless plating was performed utilizing Pd catalytic colloids deposited on the ZnO coated substrates using the same process described in section 4.2. The Cu electroless plating solution is composed of 0.15 M of $CuSO_4$, 0.30 M of $KNaC_4H_6\cdot4H_2O$, 0.21 M of NaOH, and 4.2 M of Formaldehyde. They were prepared separately and mixed before the process. Since the deposition rate of Cu is high, the electroless plating was performed only for 10-20 seconds.

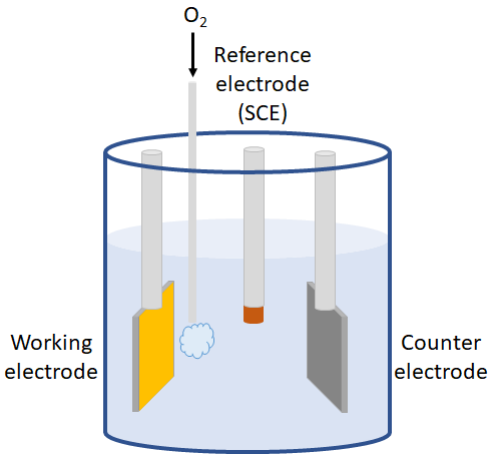

Figure 4-16 A schematic of ZnO electroplating.

4.10 Results and discussions

First, the deposited ZnO surface morphologies for three different concentrations: Zn^{2+} = 5×10^{-4} M, 5×10^{-3} M, and 5×10^{-2} M were investigated by SEM as seen in Figure 4-17. The lower concentration of Zn^{2+} resulted in sparse ZnO pillars as the SEM image shows. Thus, even though the ZnO film on the Au coated substrate appears transparent and flat, it is not suitable for use in structural color applications. On the other hand, the high concentration case where Zn^{2+} is 5×10^{-2} M, the deposited film became very hazy, and as the SEM image shows, the ZnO film consists of thin-film-like crystals orienting random directions. The case that the concentration of Zn^{2+} is 5×10^{-3} M, the ZnO film consists of dense pillar-like crystals but the surface is flat, which gives the transparent and shiny appearance in the picture. Therefore, this is the most suitable condition for structural color applications.

Next, in order to create the color, the top metal film was deposited. First, to confirm that ZnO films work for this application, Au was deposited on the ZnO films with a thickness

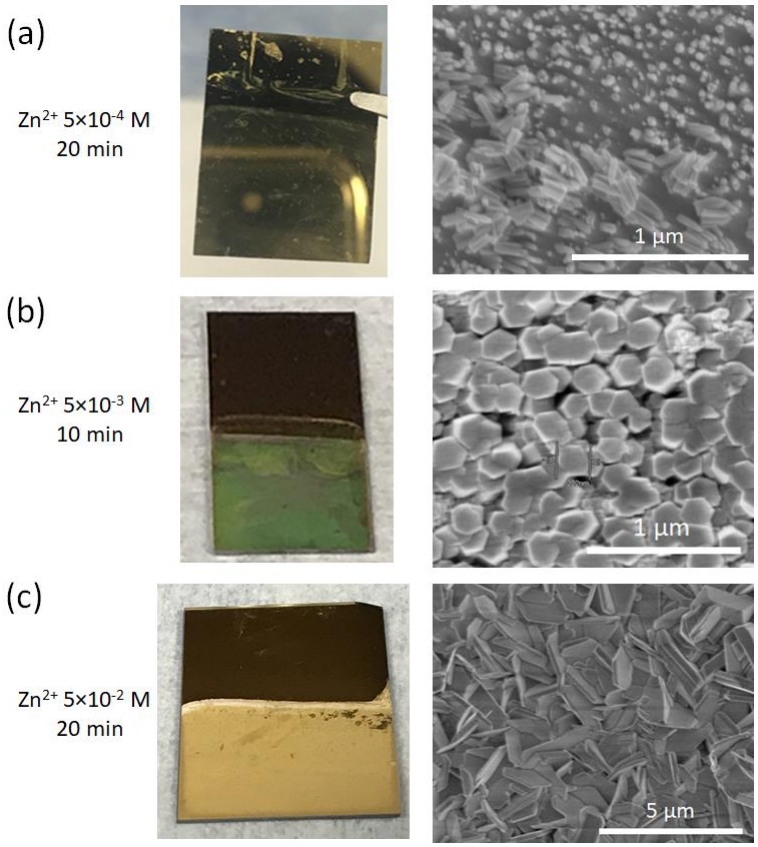

Figure 4-17 Surface morphologies of the deposited ZnO with different concentrations. (a) Zn^{2+} = 5×10^{-4} M for 20 minutes, (b) Zn^{2+} = 5×10^{-3} M for 10 minutes, and (c) Zn^{2+} = 5×10^{-2} M for 20 minutes

of 10 nm by electron beam evaporation. Figure 4-18 (a) shows two samples with the electroplated ZnO on Au/Si with the conditions of Zn^{2+} = 5×10^{-3} M for 10 minutes and 15 minutes, respectively. At this step, very slight colors were observed at certain angles because of the interferences of the light in the ZnO films. Figure 4-18 (b) shows the same samples after 10 nm of Au deposition from the top and (c) from a tilted angle. Although there are a few different colors in the same sample, the angular independent structural colors were observed for the two samples.

Then, Cu electroless plating was performed on ZnO films instead of Au deposition by electron beam evaporation. Figure 4-19 shows the ZnO film before Cu electroless plating, the sample after Cu electroless plating for 20 seconds, and the reference sample when Cu electroless plating was done for 1 minute. As can be seen in Figure 4-19 (a) and (b), the transparent ZnO film deposited on a Au/Si substrate showed the blue structural color after Cu electroless plating for 20 seconds. Figure 4-19 (c) is a reference sample showing how the sample looks when Cu electroless plating is performed longer. After only 1 minute, it showed the exact Cu appearance due to the thick Cu film created on the surface.

For further understanding of ZnO electroplating, characterizations on the ZnO films were performed. Figure 4-20 shows a cross-sectional SEM image of a ZnO film deposited with $Zn^{2+} = 5\times10^{-3}$ M for 15 minutes. The thickness of the ZnO film shown here is 320 nm. Figure 4-21 is comparisons of the simulation and experimental results for the two different colors observed on the sample. Both results match very well and it is confirmed that ZnO can work as a dielectric layer for the Fabry-Pérot cavity structural color. However, these thicknesses are much thicker than the expected ones used for the computational studies in the previous section. Therefore, electroplating for shorter time was performed to obtain thinner films aiming at ~100 nm. Figure 4-22 shows SEM images of the three different ZnO films deposited with $Zn^{2+} = 5\times10^{-3}$ M for 1 minute, 2 minutes, and 3.5 minutes, respectively. As can be seen from the images, longer plating time results in denser ZnO crystals while the thickness of the film is almost maintained. Cu electroless plating was also attempted on these samples to obtain the structural colors. However, it turns out that the Pd colloidal solution damages ZnO films as seen in Figure 4-23 (a) and (b). The borders observed on the surfaces

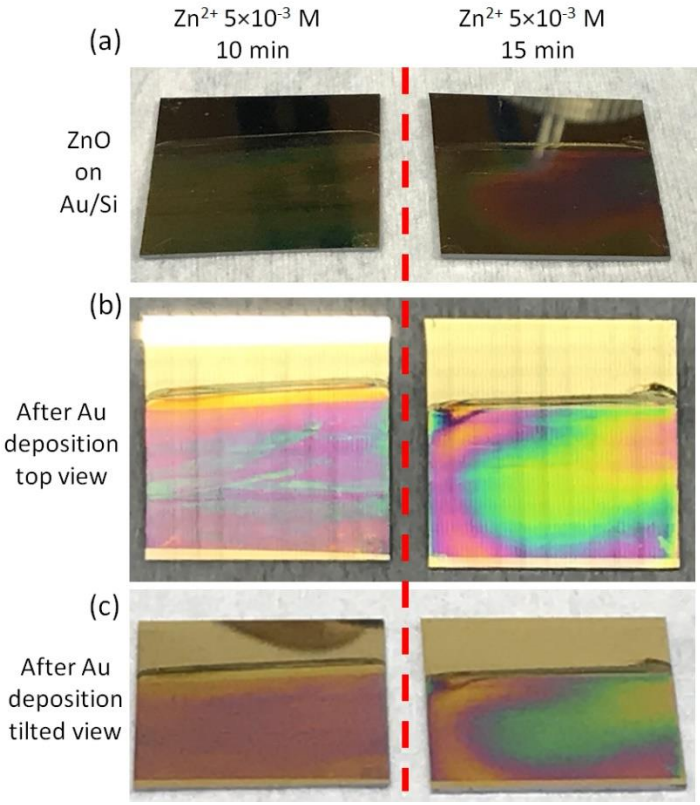

Figure 4-18 Pictures of created structural colors. (a) ZnO films on Au/Si deposited under the conditions of Zn^{2+} = 5×10^{-3} M for 10 minutes and 15 minutes, respectively. (b) After 10 nm Au deposition from the top and (c) from the tilted angle.

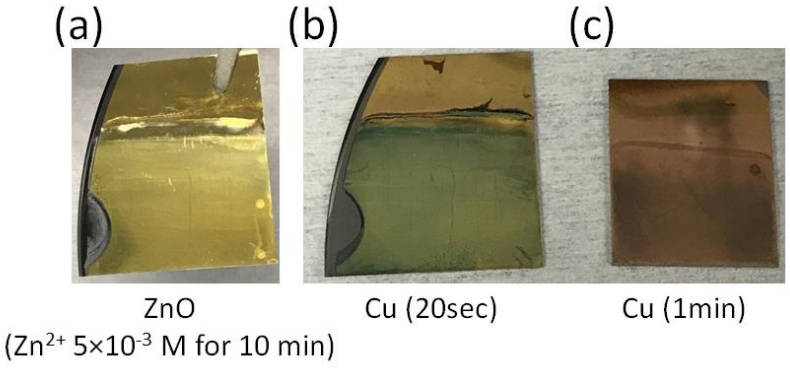

Figure 4-19 Pictures of samples coated with electroless plated Cu. (a) A ZnO film deposited on Au/Si with Zn^{2+} = 5×10^{-3} M for 10 minutes, and (b) after Cu electroless plating was done 20 seconds. (c) A sample coated with Cu by electroless plating for 1 minute.

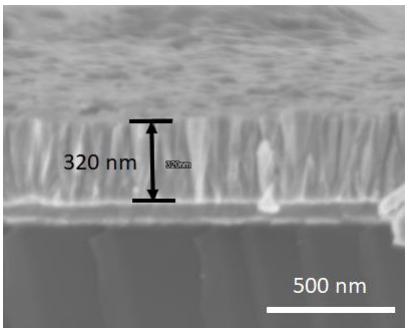

Figure 4-20 A cross-sectional SEM image of a ZnO film deposited by Zn^{2+} = 5×10^{-3} M for 15 minutes.

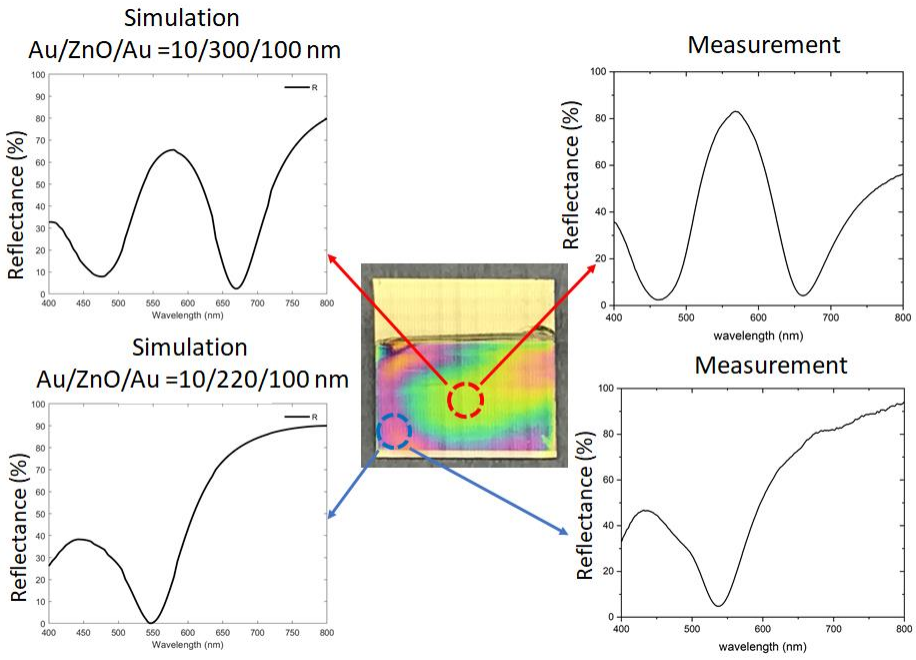

Figure 4-21 Comparisons of the simulations and measurements for two different colors.

of the ZnO deposited samples indicate the surface level of the solution while ZnO was electroplated. However, after the Pd colloid deposition process, these borders disappeared, which implies the ZnO films were dissolved. Since the Pd colloidal solution is acidic, the most plausible reason for this is that the ZnO films are dissolved fast enough when the ZnO crystal density is low. When 15 nm Au films were deposited by electron beam evaporation

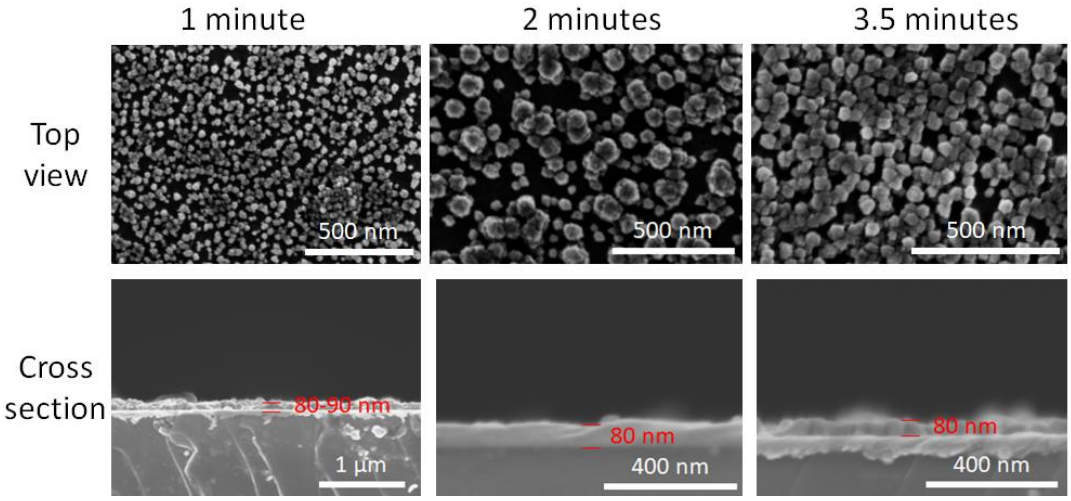

Figure 4-22 SEM images of ZnO films deposited by Zn^{2+} = 5×10^{-3} M for 1 minute, 2 minutes, and 3.5 minutes, respectively.

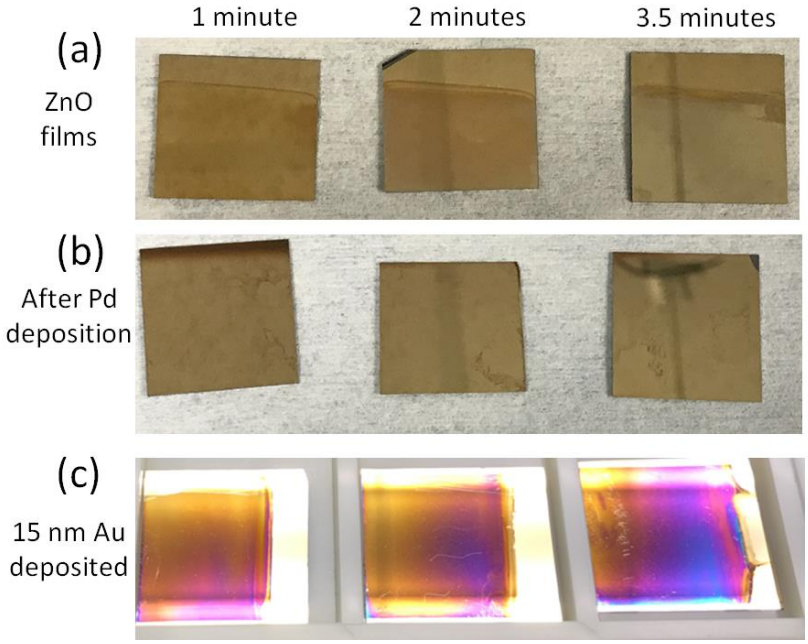

Figure 4-23 ZnO films deposited for 1 minute, 2 minutes, and 3.5 minutes.

instead of Cu electroless plating, all three samples showed bright structural colors as shown in Figure 4-23 (c). The color differences in the same sample are due to the nonuniform ZnO thicknesses resulting from the temperature gradient in the solution.

4.11 Summary

In this thesis, a new design for Fabry-Pérot structural colors replacing Cu_2O and Au with ZnO and Cu has been proposed. The new design improves the color quality and reduces the fabrication cost, owed to the plainness of the process and inexpensive materials. Its reflection spectra and angular dependency were computationally shown, as well as experimental results on the new design. The experimental results also displayed structural colors, however, there are still some issues to be resolved.

We discovered that it is challenging to electroplate ZnO that is less than 100 nm thick with high density. In the first several minutes, electroplating of ZnO increases the density of ZnO crystals rather than increases the thickness of the film. As introduced in the previous section, ZnO film deposited with $Zn^{2+} = 5\times10^{-3}$ M for 15 minutes resulted in a dense film that was 320 nm thick. Figure 4-23 shows the simulations for two different ZnO thicknesses: Cu 20 nm/ ZnO 200 nm/ Au 100 nm and Cu 20 nnm/ ZnO 320 nm/Au 100nm. Although they still have high contrasts in the reflection spectra and are expected to show colors, the angular independencies will not be obtained since the thick ZnO films create constructive and destructive interferences for the multiple orders. This could be used for another application, the angular dependent color, which changes its colors depending on the viewing angle.

CHAPTER 5

Conclusions and future work

5.1 Conclusions

This thesis discusses three different nanofabrication technologies that have shown advantages in fabrication cost compared to current technologies. First, we introduced new materials for thermal and UV nanoimprint lithography to improve the master mold quality, replication very fine patterns, and the productivity of the process. A newly developed technique based on metal transfer assisted nanolithography was also introduced to expand the material compatibility and ability for a large area patterning. When SU-8 is employed, the process can be used to fabricate electric devises directly on various substrates, while the original process which uses the transferred patterns as etching masks remains applicable in the case that KMPR is used.

Secondly, the new approach to increase the patternable size and productivity of plasmonic lithography was proposed. Based on our previous work employing epsilon-near-zero hyperbolic metamaterials (ENZ HMMs) and a photo roller system, a large photomask for plasmonic lithography which can keep the resolution sub-100 nm was discussed both computationally and experimentally. The most challenging process, the photomask fabrication, was successfully overcome by employing the modified metal transfer assisted nanolithography introduced in Chapter 2. An optical setup for large area exposure with

uniform intensity was also introduced. Although the system using ENZ HMMs is pressure sensitive, experimental work on the new plasmonic lithography has been successful. The sub-diffraction limit patterns whose period is 128 nm while using the 442 nm light source was obtained in the photoresist layer as a result.

Lastly, chapter 4 discussed low-cost material deposition technologies, electroplating and electroless plating, for nanotechnology applications. Although these technologies have a long-standing history, there has been a lack of studies on applications to optics/photonics technologies. In this thesis, electroless plating of Pt utilizing Pd colloidal catalysts were employed to create thin coatings on porous substrates for the broadband light absorber applications. Both computational and experimental studies have shown excellent absorption in the wide wavelength range (300-2400 nm) as well as improved the fabrication cost by using wet chemical processes. For structural color applications, electroplating of ZnO and electroless plating of Cu were introduced to replace Cu_2O and Au in the previous work. Computations on the new design have shown promising results which improve the color quality and reduce process complexity. Although further study is required to put the new process into practice, the performance of the new design successfully shows potential solutions for many challenges in the industry.

5.2 Future work of metal transfer assisted nanolithography

As described in Chapter 2, the transfer printing technology is a strong method that can fabricate the whole device, from the stamp to substrate. In this thesis, only Au/Ti and Al thin films were employed as the transferred metal layers, but further study on more complex

structures such as multilayer stacks of various films, oxide metal layers, and arbitrary patterns are highly desirable.

The period of the transferred gratings can be changed by stretching the substrate when a low modulus substrate is used. Similar experimental work has shown that when the substrate was stretched after the gratings were fabricated on it, the period of the gratings were expanded [120]. This technique can be applied in the opposite way by first stretching the substrate and transferring the gratings while the substrate is stretched. It is thought that the recovered substrate shrinks the grating period. This technique could be used to fabricate very fine patterns which are difficult to fabricate by photolithography.

5.3 Future work of plasmonic lithography

In chapter 3, plasmonic lithography for one dimensional gratings fabrication was discussed, but plasmonic interference lithography can be applied to two dimensional patterning as well. Figure 5-1 shows a schematic of the photomask design for two dimensional periodic patterning and its simulated result. The photomask design is almost same as the one dimensional case, except that it has two dimensional periodic Al squares instead of one dimensional gratings, and the electric field needs to be diagonal to the square as indicated by the red arrow. This polarization is simple to obtain by using a laser with circular polarization and tilting the polarizer 45˚. The technologies required to implement this experiment are essentially the same as the ones previously mentioned, highlighting the potential for plasmonic lithography technology to be used in wider applications e.g. moth-eye films [121,122].

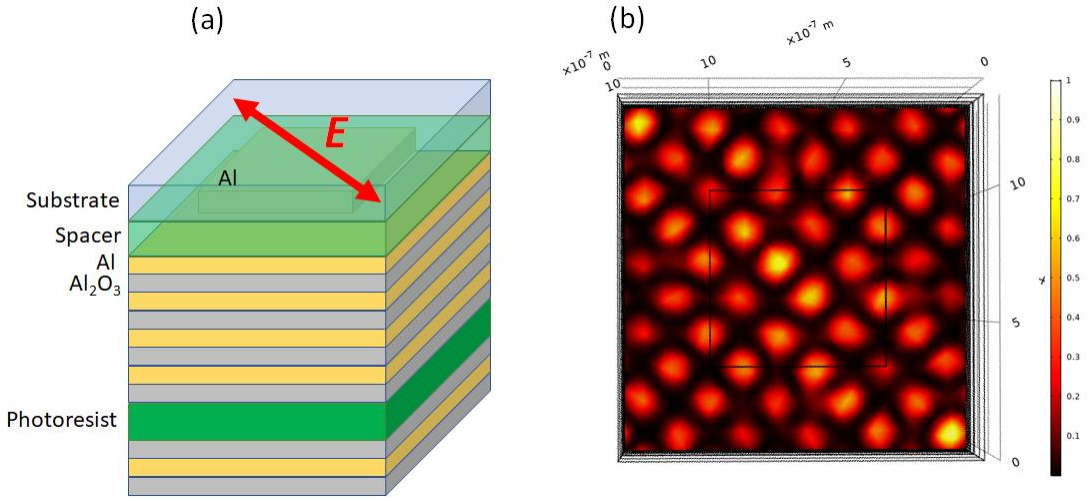

Figure 5-1 (a) A schematic of the photomask design for two dimensional patterning by plasmonic lithography, and (b) the top-view of the simulated $|E|^2$ in the photoresist layer.

In order to improve the sensitivity to the applied pressure discussed in this thesis, replacing the PET film with a flexible glass is a promising solution, as the flexible glass hasmuch higher modulus while also having high transparency and flexibility. Additionally, the planarization by a SU-8 layer and the SiO_2 etching stopper layer are not required when a flexible glass is employed, which makes the fabrication process simpler.

5.4 Future work of electrodeposition for broadband light absorbers and structural colors

Pt was used for the thin metal coating on AAO membranes in this thesis. However, according to our simulations, various other metals also show very high absorptance. Pt can be a good candidate where the stability of the devise is required e.g. solar desalination [96,123–125] and it is very useful to measure the performance as a solar desalination device. However, for general applications such as a broadband light absorber,

low-cost materials are preferred for the thin film coating. Cu and Ni in particular show very high absorptances during simulations, as shown in Figure 4-10. They are significantly less expensive than Pt, and thus, further

experimental studies employing different metals are desired.

To further increase the absorptance of the device, employing V-shape AAO membranes appears to be a promising approach. Not only vertical through holes but also tapering holes, which look like V-shape in cross section, are possible for AAO membrane fabrications. According to the reference [45], such structures can show even higher absorptances comparing with the non-tapered through holes. This kind of AAO membrane is also commercially available, and the material deposition process is compatible.

As for the structural color work using ZnO as a dielectric layer, one of the most promising approaches to improve is to first deposit a thick ZnO film (e.g. 300 nm) and then to etch it below100 nm thickness using an acid solution. It is possible that the surface morphology changes by wet etching, which results in a hazy appearance, but it is very simple and easy to implement. Another idea is to modify the electroplating process to enable thinner film deposition with a high density. A study on ZnO electroplating using a different chemical has been reported by T. Pauporté and D. Lincot [50]. $Zn(ClO_4)_2$ and $LiClO_4$ were employed instead of $ZnCl_2$ and KCl in their study. Figure 5-2 shows SEM images of the electroplated ZnO films deposited with $Zn(ClO_4)_2 = 5\times10^{-3}$ M and $LiClO_4$ = 0.1 M for (a) 2 minutes and (b) 5 minutes, respectively. As can be seen in the SEM image, a very dense ZnO film was

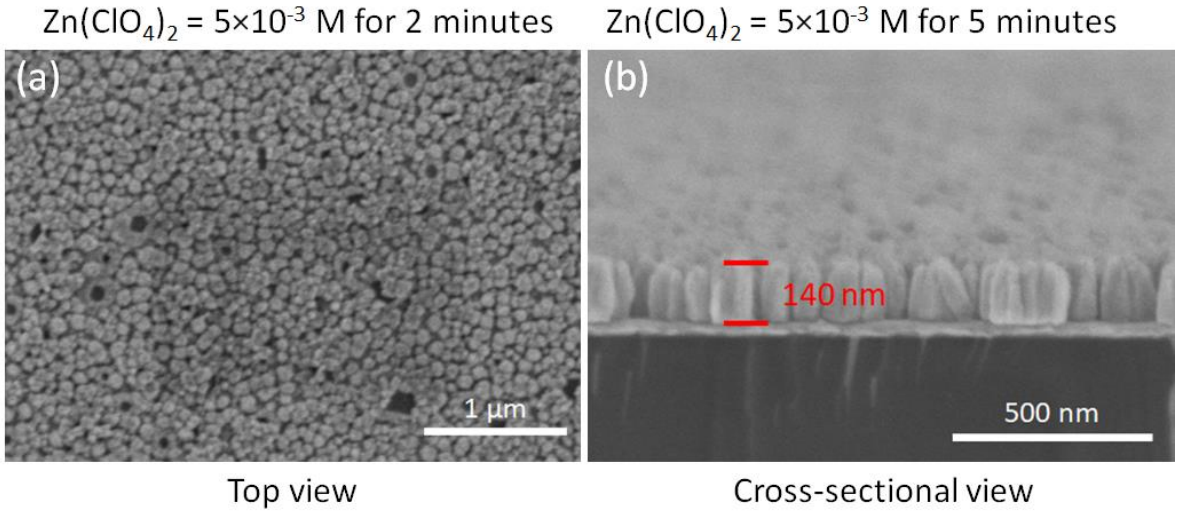

Figure 5-2 SEM images of the ZnO films deposited by $Zn(ClO_4)_2 = 5\times10^{-3}$ M and LiClO4 = 0.1 M. (a) A top view of the film deposited for 2 minutes and (b) a cross-sectional view of the film deposited for 5 minutes.

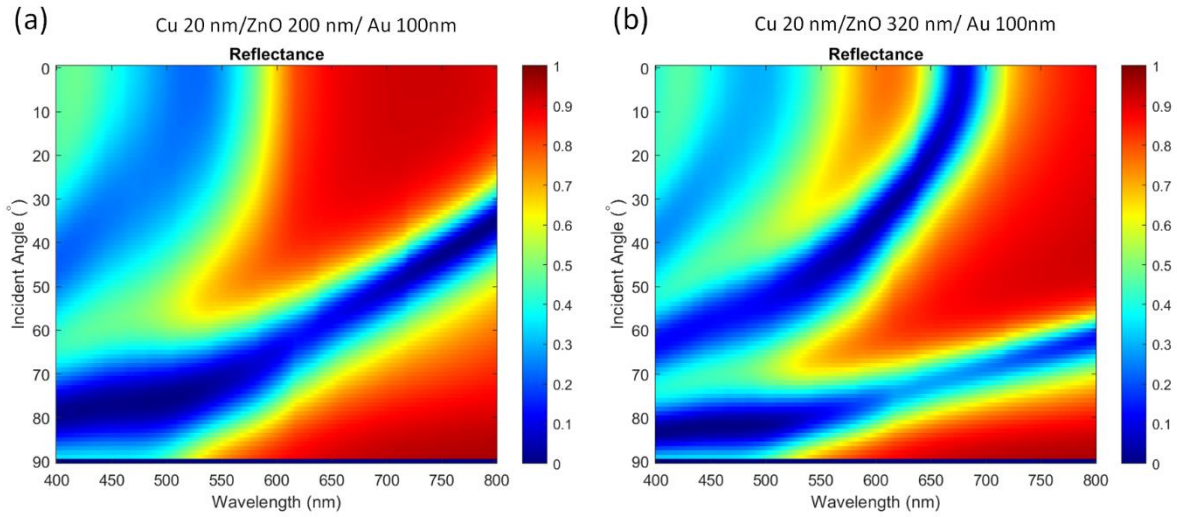

Figure 5-3 Simulation results of reflection spectra for thick ZnO films. (a) Cu 20 nm/ZnO 200 nm/Au 100nm and (b) Cu 20 nm/ZnO 320 nm/Au 100 nm.

deposited on the substrate in just 2 minutes, and the deposition rate calculated for this process is about 20-30 nm/minutes. Therefore, the ability of electroplating a dense film with sub-100 nm thickness has been shown. However, the surface of the film is rougher than the one deposited using $ZnCl_2$ and KCl. Further studies modifying these conditions to get a smoother surface is required in order to put this new design into practice.

Another approach to overcome this challenge is to employ pulsed electroplating to deposit a ZnO film. This process uses two different applied potentials. Generally, one of themis for depositing a material and the other is for reducing the material to ions, which can contribute to engineer the surface morphology, deposition rate, and thickness of the film. There have been several works using pulsed electroplating for ZnO depositions which show that the applied potential can drastically change the surface morphology while maintaining the other conditions [126–129].

Another point which can be improved upon is the nonuniformity of the electroplated ZnO. Since over 50 ˚C is required for this process to obtain a conductive ZnO film, the solution is heated during the process. However, the solution temperature also changes the deposition rate in electroplating, which results in nonuniform film deposition. Although a water bath on a hotplate was used during this work, it was not sufficient to maintain the solution temperature uniformly. One potential solution to this would be to introduce a more sophisticated tool, such as a thermostat chamber, for the better uniformity. Otherwise, simply performing electroplating at room temperature could also solve the issue. Although the ZnO film deposited at room temperature is not conductive, this is generally not an issue, as the

required thickness for structural color applications is sub-100 nm and Cu electroless plating for the top metal layer does not require conductivity for the substrate. Further studies on ZnO electroplating are necessary, but this technology shows great potential to replace and resolve issues with the former design of structural colors and conventional paint technologies.

Other oxide materials with high refractive indices are also of interest. In this thesis, only ZnO was discussed for the dielectric layer because it has a comparably high refractive index and is transparent in the visible wavelength, electroplatable, and conductive. However, when the top metal layer is deposited by electroless plating, conductivity is not required for the dielectric layer. In this case, the material choices are expanded, and many oxide metals become great candidates. For example, TiO_2 is known as a high refractive index material and can be electroplated [130–133]. Although an annealing process at 400˚C is required to obtain a high quality TiO_2 film, the thickness controllability for thin film depositions is very high according to the reference [132], which is suitable for fabricating three different colors. Therefore, TiO_2 may be another promising candidate for structural color filers.

REFERENCES

[1] B. S. Haran, A. Kumar, L. Adam, J. Chang, V. Basker, S. Kanakasabapathy, D. Horak, S. Fan, J. Chen, J. Faltermeier, S. Seo, M. Burkhardt, S. Burns, S. Halle, S. Holmes, R. Johnson, E. McLellan, T. M. Levin, Y. Zhu, J. Kuss, A. Ebert, J. Cummings, D. Canaperi, S. Paparao, J. Arnold, T. Sparks, C. S. Koay, T. Kanarsky, S. Schmitz, K. Petrillo, R. H. Kim, J. Demarest, L. F. Edge, H. Jagannathan, M. Smalley, N. Berliner, K. Cheng, D. Latulipe, C. Koburger, S. Mehta, M. Raymond, M. Colburn, T. Spooner, V. Paruchuri, W. Haensch, D. McHerron, and B. Doris, IEEE Int. Electron Devices Meet. 13 (2008).

[2] A. B. Kahng, C. H. Park, X. Xu, and H. Yao, IEEE Trans. Comput. Des. Integr. Circuits Syst. **29**, 939 (2010).

[3] M. Switkes and M. Rothschild, J. Vac. Sci. Technol. B **19**, 2353 (2001).

[4] S. Owa and H. Nagasaka, Opt. Microlithogr. XVI **5040**, 724 (2003).

[5] K. Kemp and S. Wurm, Comptes Rendus Phys. **7**, 875 (2006).

[6] N. Fu, Y. Liu, X. Ma, and Z. Chen, J. Microelectron. Manuf. **2**, 1 (2019).

[7] D. S. Engstrom, B. Porter, M. Pacios, and H. Bhaskaran, J. Mater. Res. **29**, 1792 (2014).

[8] B. C. Kress and W. J. Cummings, Dig. Tech. Pap. - SID Int. Symp. **48**, 127 (2017).

[9] T. Zhan, K. Yin, J. Xiong, Z. He, and S. T. Wu, IScience **23**, 101397 (2020).

[10] M. Stoppa and A. Chiolerio, Sensors (Switzerland) **14**, 11957 (2014).

[11] T. R. Ray, J. Choi, A. J. Bandodkar, S. Krishnan, P. Gutruf, L. Tian, R. Ghaffari, and J. A. Rogers, Chem. Rev. **119**, 5461 (2019).

[12] A. Nathan, A. Ahnood, M. T. Cole, S. Lee, Y. Suzuki, P. Hiralal, F. Bonaccorso, T. Hasan, L. Garcia-Gancedo, A. Dyadyusha, S. Haque, P. Andrew, S. Hofmann, J. Moultrie, D. Chu, A. J. Flewitt, A. C. Ferrari, M. J. Kelly, J. Robertson, G. A. J. Amaratunga, and W. I. Milne, Proc. IEEE **100**, 1486 (2012).

[13] M. Zou, Y. Ma, X. Yuan, Y. Hu, J. Liu, and Z. Jin, J. Semicond. **39**, 0 (2018).

[14] A. N. Broers, A. C. F. Hoole Andrew, and J. M. Ryan, Microelectron. Eng. **32**, 131 (1996).

[15] S. Y. Chou, P. R. Krauss, and P. J. Renstrom, Appl. Phys. Lett. **67**, 3114 (1995).

[16] S. Y. Chou, P. R. Krauss, and P. J. Renstrom, Science (80-.). **272**, 85 (1996).

[17] S. Y. Chou, P. R. Krauss, and P. J. Renstrom, J. Vac. Sci. Technol. B **14**, 4129 (1996).

[18] L. J. Guo, Adv. Mater. **19**, 495 (2007).

[19] S. Y. Chou and P. R. Krauss, Microelectron. Eng. **35**, 237 (1997).

[20] P. R. Krauss and S. Y. Chou, Annu. Device Res. Conf. Dig. **2897**, 90 (1997).

[21] J. Haisma, J. Vac. Sci. Technol. B **14**, 4124 (1996).

[22] M. Colburn, M. Stewart, S. Damle, T. Bailey, B. Choi, M. Wedlake, T. Michaelson, S. V. Sreenivasan, J. Ekerdt, and C. G. Willson, in *SPIE Conference on Emerging Lithographic Technologies* (Santa Clara, 1999), p. 379.

[23] S. H. Ahn and L. J. Guo, Adv. Mater. **20**, 2044 (2008).

[24] S. H. Ahn, J.-S. Kim, and L. J. Guo, J. Vac. Sci. Technol. B **25**, 2388 (2007).

[25] T. Mäkelä, T. Haatainen, P. Majander, and J. Ahopelto, Microelectron. Eng. **84**, 877 (2007).

[26] S. Y. Hwang, S. H. Hong, H. Y. Jung, and H. Lee, Microelectron. Eng. **86**, 642 (2009).

[27] S. H. Ahn and L. J. Guo, ACS Nano **3**, 2304 (2009).

[28] P. Yi, C. Zhang, L. Peng, and X. Lai, RSC Adv. **7**, 48835 (2017).

[29] Y. Xia and G. M. Whitesides, Angew. Chemie - Int. Ed. **37**, 550 (1998).

[30] C. Kim, M. Shtein, and S. R. Forrest, Appl. Phys. Lett. **80**, 4051 (2002).

[31] M.-G. Kang and L. J. Guo, J. Vac. Sci. Technol. B **26**, 2421 (2008).

[32] D. Qin, Y. Xia, and G. M. Whitesides, Nat. Protoc. **5**, 491 (2010).

[33] N. Fang, H. Lee, C. Sun, and X. Zhang, Science (80-.). **308**, 534 (2005).

[34] Z. W. Liu, Q. H. Wei, and X. Zhang, Nano Lett. **5**, 957 (2005).

[35] D. K. Gramotnev and S. I. Bozhevolnyi, Nat. Photonics **4**, 83 (2010).

[36] F. Hong and R. Blaikie, Adv. Opt. Mater. **1801653**, 1 (2019).

[37] J. B. Pendry, Phys. Rev. Lett. **85**, 3966 (2000).

[38] J. B. Pendry, L. Martin-Moreno, and F. J. Garcia-Vidal, Science (80-.). **305**, 847 (2004).

[39] X. Chen, F. Yang, C. Zhang, J. Zhou, and L. J. Guo, ACS Nano **10**, 4039 (2016).

[40] G. Liang, X. Chen, Q. Zhao, and L. J. Guo, Nanophotonics **7**, 277 (2018).

[41] G. Liang, C. Wang, Z. Zhao, Y. Wang, N. Yao, and P. Gao, Adv. Opt. Mater. **3**, 1248 (2015).

[42] X. Chen, C. Zhang, F. Yang, G. Liang, Q. Li, and J. Guo, ACS Nano **11**, 9863 (2017).

[43] X. Chen, S. H. Lee, C. Zhang, and Q. Li, Nanotechnology **30**, 105202 (2019).

[44] L. Zhou, Y. Tan, J. Wang, W. Xu, Y. Yuan, W. Cai, S. Zhu, and J. Zhu, Nat. Photonics **10**, 393 (2016).

[45] B. Fang, C. Yang, C. Pang, W. Shen, X. Zhang, Y. Zhang, and W. Yuan, Appl. Phys. Lett. **110**, 141103 (2017).

[46] J. U. Kim, S. Lee, S. J. Kang, and T. Il Kim, Nanoscale **10**, 21555 (2018).

[47] C. Ji, S. Acharya, K. Yamada, S. Maldonado, and L. J. Guo, ACS Appl. Mater. Interfaces **11**, 29065 (2019).

[48] Z. Yang, C. Ji, Q. Cui, and L. J. Guo, Adv. Opt. Mater. **8**, 1 (2020).

[49] S. Peulon, J. Electrochem. Soc. **145**, 864 (1998).

[50] T. Pauporté and D. Lincot, Electrochim. Acta **45**, 3345 (2000).

[51] J. J. M. Vequizo, J. Wang, and M. Ichimura, Jpn. J. Appl. Phys. **49**, (2010).

[52] S. Horiuchi and Y. Nakao, Surf. Coatings Technol. **204**, 3811 (2010).

[53] D. S. Macintyre, Y. Chen, D. Lim, and S. Thoms, J. Vac. Sci. Technol. B **19**, 2797 (2001).

[54] Y. Hirai, S. I. Harada, M. Kobayashi, and Y. Tanaka, Jpn. J. Appl. Phys. **41**, 4186 (2002).

[55] J. S. Yu, I. Kim, J. S. Kim, J. Jo, T. T. Larsen-Olsen, R. R. Søndergaard, M. Hösel, D. Angmo, M. Jørgensen, and F. C. Krebs, Nanoscale **4**, 6032 (2012).

[56] S. Garidel, M. Zelsmann, N. Chaix, P. Voisin, J. Boussey, A. Beaurain, and B. Pelissier, J. Vac. Sci. Technol. B **25**, 2430 (2007).

[57] D. R. Barbero, M. S. M. Saifullah, P. Hoffmann, H. J. Mathieu, D. Anderson, G. A. C. Jones, M. E. Weiland, and U. Steiner, Adv. Funct. Mater. **17**, 2419 (2007).

[58] https://www.films.saint-gobain.com/system/files_force/chemfilm_extruded_film_datasheets_75077.pdf?download=1.

[59] https://www.films.saint-gobain.com/sites/imdf.specialtyfilms.com/files/chemfilm_extruded_film_datasheets_75079_0.pdf.

[60] K. L. Johnson, *Point Loading of an Elastic Half-Space* (Cambridge University Press, 1985).

[61] E. M. Arruda, M. C. Boyce, and R. Jayachandran, Mech. Mater. **19**, 193 (1995).

[62] H. K. Taylor, Modeling and Controlling Topographical Nonuniformity in Thermoplastic Micro- and Nano-Embossing, Massachusetts Institute of Technology, 2009.

[63] Z. Fan, H. Razavi, J. W. Do, A. Moriwaki, O. Ergen, Y. L. Chueh, P. W. Leu, J. C. Ho, T. Takahashi, L. A. Reichertz, S. Neale, K. Yu, M. Wu, J. W. Ager, and A. Javey, Nat. Mater. **8**, 648 (2009).

[64] C. Steinhagen, M. G. Panthani, A. Vahid, B. Goodfellow, B. Koo, and B. A. Korgel, J. Am. Chem. Soc. **131**, 12554 (2009).

[65] H. L. Zhang, J. Baeyens, J. Degrève, and G. Cacères, Renew. Sustain. Energy Rev. **22**, 466 (2013).

[66] L. A. Weinstein, J. Loomis, B. Bhatia, D. M. Bierman, E. N. Wang, and G. Chen, Chem. Rev. **115**, 12797 (2015).

[67] Q. Ding, S. F. Barna, K. Jacobs, A. Choubal, G. A. Mensing, Z. Zhang, K. Yamada, N. Kincaid, G. Zhu, R. Tirawat, T. Wendelin, L. J. Guo, P. M. Ferreira, and K. C. Toussaint, ACS Appl. Energy Mater. **1**, 6927 (2018).

[68] M.-G. Kang and L. J. Guo, J. Vac. Sci. Technol. B **25**, 2637 (2007).

[69] Y. S. Kim, H. H. Lee, and P. T. Hammond, Nanotechnology **14**, 1140 (2003).

[70] S. Choi, N. Kim, G. Bae, and K. Suh, J. Mater. Chem. **21**, 14325 (2011).

[71] S. Choi, P. J. Yoo, S. J. Baek, T. W. Kim, and H. H. Lee, J. Am. Chem. Soc. **126**, 7744 (2004).

[72] M. Hegner, P. Wagner, and G. Semenza, Surf. Sci. **291**, 39 (1993).

[73] M. A. Meitl, Z. T. Zhu, V. Kumar, K. J. Lee, X. Feng, Y. Y. Huang, I. Adesida, R. G. Nuzzo, and J. A. Rogers, Nat. Mater. **5**, 33 (2006).

[74] X. Liang, Z. Fu, and S. Y. Chou, Nano Lett. **7**, 3840 (2007).

[75] T. H. Kim, K. S. Cho, E. K. Lee, S. J. Lee, J. Chae, J. W. Kim, D. H. Kim, J. Y. Kwon, G. Amaratunga, S. Y. Lee, B. L. Choi, Y. Kuk, J. M. Kim, and K. Kim, Nat. Photonics **5**, 176 (2011).

[76] A. Carlson, A. M. Bowen, Y. Huang, R. G. Nuzzo, and J. A. Rogers, Adv. Mater.

24, 5284 (2012).

[77] X. Feng, M. A. Meitl, A. M. Bowen, Y. Huang, R. G. Nuzzo, and J. A. Rogers, Langmuir **23**, 12555 (2007).

[78] H. Hiroshima, Microelectron. Eng. **86**, 611 (2009).

[79] H. Lee and G. Y. Jung, Japanese J. Appl. Physics, Part 1 Regul. Pap. Short Notes Rev. Pap. **43**, 8369 (2004).

[80] G. A. L. Iang, Opt. Lett. **44**, 1182 (2019).

[81] W. Srituravanich, N. Fang, C. Sun, Q. Luo, and X. Zhang, Nano Lett. **4**, 1085 (2004).

[82] W. Kong, Y. Luo, C. Zhao, L. Liu, P. Gao, M. Pu, C. Wang, and X. Luo, ACS Appl. Nano Mater. **2**, 489 (2019).

[83] J. Luo, B. Zeng, C. Wang, P. Gao, K. Liu, M. Pu, J. Jin, Z. Zhao, X. Li, H. Yu, and X. Luo, Nanoscale **7**, 18805 (2015).

[84] L. Pan, Y. Park, Y. Xiong, E. Ulin-Avila, Y. Wang, L. Zeng, S. Xiong, J. Rho, C. Sun, D. B. Bogy, and X. Zhang, Sci. Rep. **1**, 1 (2011).

[85] S. Kim, H. Jung, Y. Kim, J. Jang, and J. W. Hahn, Adv. Mater. **24**, 337 (2012).

[86] A. Poddubny, I. Iorsh, P. Belov, and Y. Kivshar, Nat. Photonics **7**, 958 (2013).

[87] I. I. Smolyaninov and V. N. Smolyaninova, Solid. State. Electron. **136**, 102 (2017).

[88] L. Ferrari, C. Wu, D. Lepage, X. Zhang, and Z. Liu, Prog. Quantum Electron. **40**, 1 (2015).

[89] A. Alù, M. G. Silveirinha, A. Salandrino, and N. Engheta, Phys. Rev. B - Condens. Matter Mater. Phys. **75**, 1 (2007).

[90] R. Boidin, V. Nazabal, L. Bene, and N. Petr, Ceram. Int. **42**, 1177 (2016).

[91] Y. B. Chauhan, Int. J. Sci. Res. Dev. **2**, 161 (2015).

[92] J. E. A. M. Van Den Meerakker, J. Appl. Electrochem. **11**, 395 (1981).

[93] I. Ohno, Mater. Sci. Eng. A **146**, 33 (1991).

[94] M. L. Toebes, J. A. Van Dillen, and K. P. De Jong, J. Mol. Catal. A Chem. **173**, 75 (2001).

[95] L. Zhou, Y. Tan, D. Ji, B. Zhu, P. Zhang, J. Xu, Q. Gan, Z. Yu, and J. Zhu, Sci. Adv. **2**, (2016).

[96] X. Wang, Y. He, G. Cheng, L. Shi, X. Liu, and J. Zhu, Energy Convers. Manag. **130**, 176 (2016).

[97] R. Mudachathi and T. Tanaka, Adv. Nat. Sci. Nanosci. Nanotechnol. **9**, (2018).

[98] R. Panwar, S. Puthucheri, D. Singh, and V. Agarwala, IEEE Transactions on Magnetics.

[99] J. Kim, K. Han, and J. W. Hahn, Sci. Rep. **7**, 6740 (2017).

[100] M. Elkabbash, K. V. Sreekanth, Y. Alapan, M. Kim, J. Cole, A. Fraiwan, T. Letsou, Y. Li, C. Guo, R. M. Sankaran, U. A. Gurkan, M. Hinczewski, and G. Strangi, ACS Photonics **6**, 1889 (2019).

[101] J. Fang, T. Liu, Z. Chen, Y. Wang, W. Wei, X. Yue, and Z. Jiang, Nanoscale **8**, 8899 (2016).

[102] J. Y. Lu, S. H. Nam, K. Wilke, A. Raza, Y. E. Lee, A. AlGhaferi, N. X. Fang, and T. J. Zhang, Adv. Opt. Mater. **4**, 1255 (2016).

[103] Z. Li, E. Palacios, S. Butun, H. Kocer, and K. Aydin, Sci. Rep. **5**, 1 (2015).

[104] Y. Cui, K. H. Fung, J. Xu, H. Ma, Y. Jin, S. He, and N. X. Fang, Nano Lett. **12**, 1443 (2012).

[105] Y. Han, J.-A. Huang, X.-Y. Liu, X.-J. Zhang, J.-X. Shi, and C.-C. Yan, Opt. Express **24**, 9178 (2016).

[106] K.-D. Song, T. J. Kempa, H.-G. Park, and S.-K. Kim, Opt. Express **22**, A992 (2014).

[107] W. Li, U. Guler, N. Kinsey, G. V. Naik, A. Boltasseva, J. Guan, V. M. Shalaev, and A. V. Kildishev, Adv. Mater. **26**, 7959 (2014).

[108] D. Hu, H.-Y. Wang, and Q.-F. Zhu, J. Nanophotonics **10**, 026021 (2016).

[109] C. Cao and Y. Cheng, Appl. Phys. A Mater. Sci. Process. **125**, 1 (2019).

[110] G. D. Sulka, A. Brzózka, L. Zaraska, and M. Jaskuła, Electrochim. Acta **55**, 4368 (2010).

[111] H. Li, L. Wu, H. Zhang, W. Dai, J. Hao, H. Wu, F. Ren, and C. Liu, ACS Appl. Mater. Interfaces **12**, 4081 (2020).

[112] J. Yang, S. Qu, H. Ma, J. Wang, S. Yang, and Y. Pang, Opt. Laser Technol. **101**, 177 (2018).

[113] K. Kumar, H. Duan, R. S. Hegde, S. C. W. Koh, J. N. Wei, and J. K. W. Yang, Nat. Nanotechnol. **7**, 557 (2012).

[114] T. Xu, Y. K. Wu, X. Luo, and L. J. Guo, Nat. Commun. **1**, 59 (2010).

[115] M. S. Davis, W. Zhu, T. Xu, J. K. Lee, H. J. Lezec, and A. Agrawal, Nat. Commun. **8**, (2017).

[116] M. J. Uddin and R. Magnusson, Opt. Express **21**, 12495 (2013).

[117] A. F. Kaplan, T. Xu, and L. Jay Guo, Appl. Phys. Lett. **99**, (2011).

[118] O. Aguilar, S. de Castro, M. P. F. Godoy, and M. Rebello Sousa Dias, Opt. Mater. Express **9**, 3638 (2019).

[119] A. Goux, T. Pauporté, J. Chivot, and D. Lincot, Electrochim. Acta **50**, 2239 (2005).

[120] S. H. Ahn and L. J. Guo, Nano Lett. **10**, 4228 (2010).

[121] S. J. Wilson and M. C. Hutley, Opt. Acta (Lond). **29**, 993 (1982).

[122] B. J. Bae, S. H. Hong, E. J. Hong, H. Lee, and G. Y. Jung, Jpn. J. Appl. Phys. **48**, 3 (2009).

[123] H. Ghasemi, G. Ni, A. M. Marconnet, J. Loomis, S. Yerci, N. Miljkovic, and G. Chen, Nat. Commun. **5**, 1 (2014).

[124] M. Zhu, Y. Li, F. Chen, X. Zhu, J. Dai, Y. Li, Z. Yang, X. Yan, J. Song, Y. Wang, E. Hitz, W. Luo, M. Lu, B. Yang, and L. Hu, Adv. Energy Mater. **8**, 1701028 (2018).

[125] M. Zhu, J. Yu, C. Ma, C. Zhang, D. Wu, and H. Zhu, Sol. Energy Mater. Sol. Cells **191**, 83 (2019).

[126] C. Dunkel, F. Lüttich, H. Graaf, T. Oekermann, and M. Wark, Electrochim. Acta **80**, 60 (2012).

[127] C. V. Manzano, O. Caballero-Calero, S. Hormeño, M. Penedo, M. Luna, and M. S. Martín-González, J. Phys. Chem. C **117**, 1502 (2013).

[128] M. Stumpp, D. Damtew, D. Stock, K. Hess, D. Schröder, and D. Schlettwein, J. Electrochem. Soc. **165**, D461 (2018).

[129] M. Lakhdari, F. Habelhames, B. Nessark, M. Girtan, H. Derbal-Habak, Y. Bonnassieux, D. Tondelier, and J. M. Nunzi, EPJ Appl. Phys. **84**, 1 (2018).

[130] C. Natarajan and G. Nogami, J. Electrochem. Soc. **143**, 1547 (1996).

[131] S. Karuppuchamy, K. Nonomura, T. Yoshida, T. Sugiura, and H. Minoura, Solid State Ionics **151**, 19 (2002).

[132] P. Balaya, Sol. Energy (2014).

[133] G. Y. Teo, M. P. Ryan, and D. J. Riley, Electrochem. Commun. **47**, 13 (2014).